

# **Understanding the Effect of Climate and Hydrometeorological Extremes on Natural and Human-Induced Hydrosystems**

by

**Jeongwoo Hwang**

A dissertation submitted to the Graduate Faculty in Engineering at The City  
University of New York  
in conformity with the requirements for the degree of  
Doctor of Philosophy  
in  
Civil and Environmental Engineering

New York, USA

May 2021

---

Copyright © 2021 Jeongwoo Hwang

All rights reserved

---

*" This work is dedicated to my parents Kyu-Nam Hwang and Geewan Kim, my sister Yusu, and my beloved Hyemin "*

# **Understanding the Effect of Climate and Hydrometeorological Extremes on Natural and Human-Induced Hydrosystems**

Jeongwoo Hwang

This manuscript has been read and accepted for the Graduate Faculty in Engineering in satisfaction of the dissertation requirement for the degree of Doctor of Philosophy

---

Naresh Devineni, Chair of Examining Committee

Date

---

---

Ardie D. Walser, Associate Dean for Academic Affairs

Date

---

## **EXAMINING COMMITTEE**

Prof. Naresh Devineni, Mentor, Dept. of Civil Engineering, The City College of New York

Prof. Reza Khanbilvardi, Dept. of Civil Engineering, The City College of New York

Prof. Hansong Tang, Dept. of Civil Engineering, The City College of New York

Prof. Hyun-Han Kwon, Dept. of Civil and Environmental Engineering, Sejong University

Prof. Upmanu Lall, Dept. of Earth and Environmental Engineering, Columbia University

# Abstract

The contemporary hydrosystems of the United States involve a complex combination of natural and modified basins in the presence of changing climate and anthropogenic impacts. An enhanced understanding of the interdependence between climate forcings, human-induced interventions, and water balance in both natural and modified basins are essential for developing reliable and resilient hydrosystems and for better water resources management. In response, this dissertation focuses on investigating the hydroclimatology of natural and modified basins across the contiguous United States. It has three research objectives: (1) to explain flow alterations due to anthropogenic activities, especially dam operations, in modified basins and understand how dam attributes contribute to these alterations, (2) to enhance our understandings of the interactions between catchment attributes, climate forcings, and water balance in natural basins across the contiguous United States, including mountainous and snow-dominated regions, (3) to better understand and predict the spatial manifestation of precipitation extremes by identifying their concurrent nature across the contiguous United States and inferring the significant drivers that govern their spatiotemporal variability. For the first objective, an extensive investigation of anthropogenic alterations in streamflow regimes is performed. The influence of a network of dams on the frequency of streamflow and the propagational effect of its variability are explored across dendritic

streamflow networks. The second objective is achieved by developing and testing a physics-based conceptual water balance model that includes snow melting process for natural basins at the intra-annual timescales. The model is used as a basis to better quantify the time-varying catchment response to climate forcings. For the third objective, a systematic framework based on modern machine learning techniques is developed to identify the spatial manifestation of precipitation extremes (wet and dry) and explain their climate teleconnections. The findings from this dissertation have the potential to provide mitigation plans for future extremes by optimizing water allocations and catchment land use and land covers.

# **Thesis Committee**

**Naresh Devineni, Ph.D. (Advisor and Committee Chair)**

Associate Professor

Department of Civil Engineering

The City College of New York, City University of New York

**Reza Khanbilvardi, Ph.D.**

Professor

Department of Civil Engineering

The City College of New York, City University of New York

**Hansong Tang, Ph.D.**

Associate Professor

Department of Civil Engineering

The City College of New York, City University of New York

**Hyun-Han Kwon, Ph.D.**

Professor

Department of Civil and Environmental Engineering

Sejong University

**Upmanu Lall, Ph.D.**

Professor

Department of Earth and Environmental Engineering

Columbia University

# Acknowledgments

First, I would like to express my greatest sense of gratitude to my doctoral advisor, Professor Naresh Devineni, for providing me with incredible guidance and support during my Ph.D. studies. From his immense knowledge and enthusiasm, I have learned what a good scholar should be. Despite the outbreak of a severe pandemic during my doctoral studies, his consideration and kindness allowed me to accomplish high-quality research achievements.

I am proud and grateful to have a dissertation committee composed of prominent scholars; Professor Reza Khanbilvardi, Professor Hansong Tang, Professor Hyun-Han Kwon, and Professor Upmanu Lall. Their invaluable suggestions and guidance enriched the quality of my study and encouraged me to devote myself to research.

I would also like to thank Professor Sankar Arumugam and Professor Albert Ruhi for their contributions to the study of understanding the water system of the Colorado River Basin and investigating its streamflow changes. They are the co-authors on the papers analyzing streamflow alteration in the Colorado River Basin, which also serves as chapter 2 of this dissertation.

I would like to thank the Civil Engineering Department, Grove School of Engineering, and the City College of New York for giving me this wonderful opportunity to pursue this Ph.D. study. Especially, I sincerely thank the staffs of the

City College of New York who risked themselves during the pandemic to let our research continue.

Last but not the least, I specially thank my beloved wife and family (father, mother, and sister) for their constant support and love. I also express my gratitude to all my friends for the support and help.

This research was supported by the U.S. Department of Energy Early CAREER Award No. DE-SC0018124 (PI. Naresh Devineni) and the United States Geological Survey (USGS) Powell Center Working Group Project: "A global synthesis of land surface fluxes under natural and human-altered watersheds using the Budyko framework".

The journal articles published from this research, or that will be considered for publication shortly hereafter, are listed here.

- 1) **Hwang, J.**, Kumar, H., Ruhi, A., Sankarasubramanian, A., and Devineni, N., 2021, Quantifying Dam-Induced Fluctuations in Streamflow Frequencies Across the Colorado River Basin, *Water Resources Research*, accepted subject to minor revision. ([Chapter 2](#))
- 2) **Hwang, J.** and Devineni, N., 2021, An improved Zhangs Dynamic Water Balance Model using Budyko-based snow representation for better streamflow predictions, *Water Resources Research*, under review. ([Chapter 3](#))
- 3) **Hwang, J.** and Devineni, N., 2021, Quantifying the Spatial Coherence of Deficit and Excess Rainfall across the Continental United States, *Geophysical Research Letter*, under review. ([Chapter 4](#))
- 4) Ruhi, A., **Hwang, J.**, Devineni, N., Mukhopadhyay, S., Kumar, H., Comte, L., Worland, S., and Sankarasubramanian, A., 2021, How does flow alteration propagate across a large, highly-regulated basin? Dam attributes, network context, and

implications for biodiversity, *Proceedings of the National Academy of Sciences of the United States of America*, under review.

- 5) Kumar, H., **Hwang, J.**, Devineni, N., and Sankarasubramanian, A., 2021, A sequent peak algorithm-based degree of regulation index for complex river networks, *Water Resources Research*, under review.

# Table of Contents

<b>Abstract</b>	<b>i</b>
<b>Thesis Committee</b>	<b>iii</b>
<b>Acknowledgments</b>	<b>iv</b>
<b>Table of Contents</b>	<b>vii</b>
<b>List of Tables</b>	<b>xi</b>
<b>List of Figures</b>	<b>xii</b>
<b>1 Introduction</b>	<b>1</b>
1.1 Motivation . . . . .	1
1.2 Science Questions . . . . .	6
1.3 Scientific Contributions . . . . .	7
1.4 Dissertation Structure . . . . .	8
<b>2 Quantifying Dam-Induced Fluctuations in Streamflow Frequencies Across the Colorado River Basin</b>	<b>12</b>
2.1 Summary . . . . .	12

2.2	Introduction . . . . .	13
2.3	Data . . . . .	17
2.3.1	The Colorado River Basin and its Importance for Water Management . . . . .	17
2.3.2	Naturalized Flow Data . . . . .	17
2.3.3	Observed Flow Data . . . . .	18
2.3.4	Criteria for Dam Selection . . . . .	21
2.4	Method . . . . .	21
2.4.1	Wavelet Transform . . . . .	23
2.4.2	Wavelet Coherence . . . . .	24
2.4.3	Dynamic Time Warping Based Hierarchical Clustering . . . . .	26
2.4.4	Wavelet Coherence Interpretation under Known Signals . . . . .	27
2.5	Results and Analysis . . . . .	31
2.5.1	Annual Frequency . . . . .	32
2.5.2	Multi-Annual Frequency . . . . .	39
2.6	Discussion and Concluding Remarks . . . . .	46
<b>3</b>	<b>An Improved Zhangs Dynamic Water Balance Model Using Budyko-Based Snow Representation for Better Streamflow Predictions</b>	<b>59</b>
3.1	Summary . . . . .	59
3.2	Introduction . . . . .	60
3.3	Data Description . . . . .	64
3.3.1	Streamflow Data . . . . .	65
3.3.2	Climate Forcings Data . . . . .	66

3.4	Methods . . . . .	67
3.4.1	Zhangs Dynamic Water Balance Model (ZDWBM) . . . . .	67
3.4.2	Implantation of a Budyko-based Snow Module to ZDWBM .	73
3.4.3	Monthly Parameterization . . . . .	80
3.5	Results and Discussion . . . . .	84
3.5.1	Performance of the Original ZDWBM across the Continental United States . . . . .	85
3.5.2	Model performance with the implanted snow module . . . .	88
3.5.3	Model performance with the implanted snow module and monthly parameterization . . . . .	92
3.5.4	Assessment and validation of the model improvements . . . .	95
3.5.5	Assessment of Model Parameters . . . . .	98
3.6	Summary and Conclusion . . . . .	103
<b>4</b>	<b>Quantifying the spatial coherence of deficit and excess rainfall across the continental United States</b>	<b>112</b>
4.1	Summary . . . . .	112
4.2	Introduction . . . . .	113
4.3	Materials and Methods . . . . .	117
4.3.1	Precipitation Data . . . . .	117
4.3.2	Cumulative Deficit and Excess Index . . . . .	117
4.3.3	Robust Principal Component Analysis (rPCA) . . . . .	120
4.3.4	Climate modeling with ENSO . . . . .	121
4.4	Results . . . . .	122

4.4.1	Simultaneous Dry Extremes . . . . .	123
4.4.2	Simultaneous Wet Extremes . . . . .	124
4.4.3	Association of Spatiotemporal Extremes with El Niño South-Ern Oscillation . . . . .	125
4.5	Summary . . . . .	127
<b>5</b>	<b>Conclusion and Forward</b>	<b>132</b>
5.1	Concluding Remarks . . . . .	132
5.2	Future Works . . . . .	136

# List of Tables

2.1	Details of the USGS streamflow gauging stations used in the study. . .	20
2.2	Summary of Wavelet Coherence Simulation. . . . .	28
3.1	Summary of the incremental improvements of the model for all and snow-affected HCDN catchments across the CONUS. . . . .	86

# List of Figures

- 2.3 Results of the wavelet coherence simulations between two synthetic sinusoidal time series  $y_1$  and  $y_2$ . The simulated time series  $y_1$  and  $y_2$  are initially set to be identical to each other, and one wave component of  $y_2$  is forced to change over time for each simulation while the other components are fixed. The time-varying wavelet coherence between  $y_1$  and  $y_2$  is estimated when the amplitude component of the annual signal of  $y_2$  ( $A_3$ ) changes over time (a), when the phase lag component of the annual signal of  $y_2$  ( $\varphi_3$ ) changes over time (b), and when the phase lag component of the annual signal of  $y_2$  ( $f_3$ ) changes over time (c). Similarly, the simulation measures the wavelet coherence between  $y_1$  and  $y_2$  when the amplitude component of the multi-annual signal of  $y_2$  ( $A_4$ ) changes over time (d), when the phase lag component of the multi-annual signal of  $y_2$  ( $\varphi_4$ ) changes over time (e), and when the phase lag component of the multi-annual signal of  $y_2$  ( $f_4$ ) changes over time (f).





2.7	Wavelet power spectrum of the naturalized streamflow (a) and the controlled streamflow (b) at stations of Cluster-4 from the annual frequency analysis. . . . .	38
2.8	Cluster profiles based on the wavelet coherence loss of streamflow regarding multi-annual frequency (24–60 months). The spatial distribution of the clusters (a) and time series of the wavelet coherence loss at each cluster (b - e) is shown. Rest of the figure is similar to the description provided in Figure 2.8. . . . .	40
2.9	Wavelet power spectrum of the naturalized streamflow (a) and the controlled streamflow (b) at stations of Cluster-2 from the multi-annual frequency analysis. The scale-averaged wavelet power is also presented for both naturalized flow (c) and controlled flow (d) at these stations. . . . .	43
2.10	Wavelet power spectrum of the naturalized streamflow (a) and the controlled streamflow (b) at stations of Cluster-3 from the multi-annual frequency analysis. The scale-averaged wavelet power is also presented for both naturalized flow (c) and controlled flow (d) at these stations. . . . .	44
2.11	Wavelet power spectrum of the naturalized streamflow (a) and the controlled streamflow (b) at stations of Cluster-4 from the multi-annual frequency analysis. The scale-averaged wavelet power is also presented for both naturalized flow (c) and controlled flow (d) at these stations. . . . .	45

2.12 Simplified diagram of the riverine network with the local and cumulative alterations measured for both the annual (a) and multi-annual frequency bands (b). Dam-induced local regulations are represented with triangles, and cumulative alterations are denoted with circles. . .	50
3.1 Spatial distribution of the selected HCDN basins across the continental United States. . . . .	65
3.2 Diagram of the hydrological partitioning process of the ZDWBM (left) and the corresponding flowchart (right). . . . .	69
3.3 Diagram of the hydrological partitioning process of the snow augmented ZDWBM (left) and the corresponding flowchart (right). . . .	80
3.4 Performance of the original ZDWBM across the CONUS: (a) spatial distribution of NSE across the CONUS (b) cumulative distribution function of NSE (c) distribution of NSE for each HUC2 region (d) dependence between NSE and the snow- factor R. The red horizontal dashed line in each subfigure indicates the threshold for a good model ( $NSE > 0.65$ ) . . . . .	87
3.5 Performance of ZDWBM-snow across the CONUS: (a) spatial distribution of NSE across the CONUS (b) cumulative distribution function of NSE (c) distribution of NSE for each HUC2 region (d) dependence between NSE and the snow-factor R. The red horizontal dashed line in each subfigure indicates the threshold for a good model ( $NSE > 0.65$ ) . . . . .	90

3.6 Bias of ZDWBM-snow for each season. The data points shown in gray indicate catchments that are not affected by snow ( $R < 0.4$ ), whereas the data points shown in black are snow-affected basins ( $R > 0.4$ ). The inset of each subfigure represents the histogram of relative errors between the observed and simulated for all catchments (gray) and snow-affected catchments (black). . . . .	91
3.7 Performance of ZDWBM-msnow across the CONUS: (a) spatial distribution of NSE across the CONUS (b) cumulative distribution function of NSE (c) distribution of NSE for each HUC2 region (d) dependence between NSE and snow-factor R. The red horizontal dashed line in each subfigure indicates the threshold for a good model ( $NSE > 0.65$ ) . . . . .	93
3.8 Bias of ZDWBM-msnow for each season. The data points shown in gray indicate catchments that are not affected by snow ( $R < 0.4$ ), whereas the data points shown in black are snow-affected basins ( $R > 0.4$ ). The inset of each subfigure represents the histogram of relative errors between the observed and simulated for all catchments (gray) and snow-affected catchments (black). . . . .	94
3.9 Comparison of NSE for ZDWBM-msnow and original ZDWBM. . .	96
3.10 Cross-validation results verifying for overfitting. (a) Comparison between NSE from calibration and validation periods (b) Comparison between the cumulative distribution function of NSE from calibration (solid) and validation periods (dotted). . . . .	97

3.11 Seasonal spatial distribution of average melting efficiency ( $a_d$ ), catchment retention efficiency ( $e_h$ ), evapotranspiration efficiency ( $i_l$ ), groundwater transition rate ( $m_p$ ), and maximum soil-moisture capacity ( $q_t$ ) for the HCDN catchments where ZDWBM-msnow performance was classified as <i>good</i> during the calibration. Figure continued on next page. . . . .	101
4.1 Annual precipitation anomalies across the CONUS for four samples years: (a) 1991, (b) 1998, (c) 2007, (d) 2011. . . . .	115
4.2 Diagrams of (a) how the cumulative deficit index ( $CDI$ ) and cumulative excess index ( $CEI$ ) are computed as rainfall distribution and long-term mean daily rainfall vary over a synthetic year and (b) how the simultaneous dry and wet extremes are defined from rPCA. In the top figure of (a), the vertical bars (supply) are the daily rainfall magnitudes, and the red line (demand) is the long-term mean daily rainfall. In the bottom figure of (a), the vertical red bars are the cumulative deficits, and the blue bars are the cumulative excesses. The top figure of (b) demonstrates the rPCA decomposition of the $CDI$ matrix ( $M_{CDI}$ ), and the red-colored values in the sparse matrix ( $S_{CDI}$ ) are defined as the simultaneous dry extremes. The bottom figure of (b) shows the decomposition of the $CEI$ matrix ( $M_{CEI}$ ), and the blue-colored values in the sparse matrix ( $S_{CEI}$ ) are defined as the simultaneous wet extremes. . . . .	119

4.3 Spatial variability of (a) spatial distributions of spatiotemporal dry extremes ( <i>left</i> ) and proportion of <i>CDI</i> that is unexpected ( <i>right</i> ) and (b) of spatial distributions of spatiotemporal wet extremes ( <i>left</i> ) and proportion of <i>CEI</i> that is unexpected ( <i>right</i> ) for four sample years 1991, 1998, 2007, 2011. . . . .	124
4.4 (a) Spatial distribution of stations where the simultaneous manifestation of spatiotemporal dry extremes has statistically significant association with ENSO and (b) stations where the simultaneous manifestation of spatiotemporal wet extremes has statistically significant association with ENSO. The color of the dots indicates the $\beta$ coefficient for ENSO. The CONUS is divided into HUC02 basins and the percentage of ENSO-significant stations in each basin is presented alongside both maps. . . . .	126

# Chapter 1

## Introduction

### 1.1 Motivation

The value of water as a resource is universal, and its availability, accessibility, and reliability are of utmost importance. Understanding the climate and catchment controls of water balance, especially in a changing world is vital for understanding the reliability of water. In this regard, several important studies have shown the intricacies of climatic forcings (precipitation and temperature/potential evapotranspiration) and catchment characteristics as the dominant controls of the water balance (Eagleson, 1978; Milly, 1994; Farmer, Sivapalan, and Jothityangkoon, 2003; Zhou et al., 2015). Recently, the drastic increase in demand for water due to growing population and urbanization has led to a vast installation of hydraulic structures and systems across the world to such an extent that human-induced direct intervention has also become one of the chief forces (among climate variability and catchment characteristics) that determines contemporary and future water availability (Vörösmarty and Sahagian, 2000; Sivapalan et al., 2003; Vogel et al., 2015). Simultaneous effects from recent changes in climate and internal variability, land-use and land-cover change, and human controls have made the water yield

process complicated, limiting our ability to understand its variability and predict its availability. Spatiotemporal heterogeneity of the streamflow regimes reflects the complexity of the interaction between the control variables. See for example, Figure 1.1 that shows the de-seasoned monthly flow at 2 different stations that are located near to each other in the Colorado River Basin. Station 0938000 is placed at the immediate downstream of Hoover Dam in the vicinity of Station 09382000, which is located at the headwater of a tributary. While the immediate downstream of the Hoover Dam (Station 0938000) shows a drastic change at a certain point and controlled variability, the natural flow at the vicinal headwater (Station 09382000) continues to hold its natural variability while showing a decreasing trend. This significant difference disregarding their physical proximity is an exemplar that not only climate variability but also catchment characteristics and human-induced changes are affecting the regional hydrological cycle. The availability of water for communities dependent on this catchment is then governed by a combination of controlled and natural variability.

More than 90,000 dams across the United States together store almost one years mean annual natural runoff (Graf, 1999). At the same time, major dams, on average, reduce annual peak discharges by 67% and change the timing of high and low flows (Graf, 2006). Such human-induced direct interventions heavily affect the streamflow variability and subsequent complications including sediment trapping (Vörösmarty, 1997), changes in biodiversity (Poff et al., 2007; Ruhi et al., 2018), and sea level rising (Sahagian, Schwartz, and Jacobs, 1994). Climate variability has traditionally been considered as the dominant factor governing the natural hydrological cycle (Budyko, 1961), while the effect of catchment characteristics is secondary.

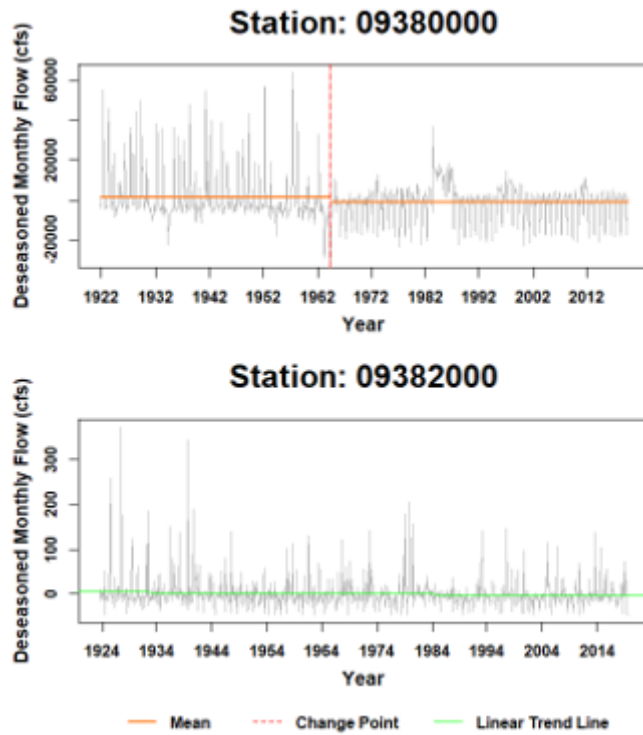


**Figure 1.1:** Time series of de-seasoned monthly streamflow at the downstream of Hoover Dam (above) and at a vicinal headwater (below).

With a large portion of the terrestrial surface, approximately 41%, has been globally altered by human activities (Sterling and Ducharne, 2008) with pandemic engineering of water resources. Anthropogenic intervention has become the primary control that shapes the hydrological cycle, especially in human-invaded regions. These evident human-induced interventions, combined with climate and catchment characteristics, have made the hydrological processes more complicated.

The potential for increasing extreme events as induced by changing climate exacerbates this scenario. For instance, hydrometeorological extremes that manifest as part of the climate variability have brought more than \$1,700 billion in the estimated losses and 13,249 fatalities to the United States from 1980 to 2019 (Weather

and Disasters, 2020). Amid these historical catastrophes, the frequency and intensity of precipitation extremes and droughts are showing an upward trend in several regions of the United States (Andreadis and Lettenmaier, 2006; Dai, 2013; Kunkel et al., 2013; Armal, Devineni, and Khanbilvardi, 2018), exacerbating the future risk of those extremes. Despite the overwhelming evidence pointing to intensifying meteorological extremes, such changes have not generally translated to clear increases in flood inundations or droughts (Hartmann et al., 2013; Hodgkins et al., 2017). This could be attributable to the natural countervailing effects of the catchment (Andrés Doménech et al., 2015; Ivancic and Shaw, 2015) and human controls that mitigate the impact of meteorological extremes (Vogel, Yaindl, and Walter, 2011). As previously discussed, it is now difficult to find a watershed that is not modified by human hydrologic processes (Vörösmarty et al., 2010; Vörösmarty et al., 2013) and not impacted by climate induced natural hazards.

The overall statements above emphasize the complexity of the contemporary hydrosystems and bolster the necessity of an extensive investigation of hydrological processes to adequately develop reliable and resilient hydrosystems and manage future water resources. As the modern hydrosystem of the United States is composed of combinations and interactions of natural and human-impacted basins, such hydrosystem should, above all, be comprehensively understood based on independent investigations of the hydrological processes of each type of basins. Moreover, extreme climate conditions of the basins should also be a part of our primary investigations since they directly influence social and ecological prosperity with various levels of impact across the United States depending on the basin characteristics. This research, therefore, aims to contribute new knowledge to the field

of hydrology by systematically unfolding the complexities in the hydrological processes, which involve dynamic interactions between climate forcings, catchment, anthropogenic intervenes, and water balance by independently exploring the hydrosystems in modified and natural basins. In addition, from a water resources management perspective, this study attempts to assess the vulnerability of the hydrosystems across the continental United States to future hydrometeorological extremes.

This dissertation focuses on developing a systematic framework to better understand the role of climate, anthropogenic effects, and hydrometeorological extremes on natural and modified catchments across the continental United States.

With the dissertation's core objective in mind, these investigations were inspired by the following issues.

1. There is a lack of clear understanding of the time-varying changes in streamflow frequency across river networks that are highly influenced by dams and the incorporation of free flowing tributaries. (**presented in Chapter 2**).
2. There is a need to develop a dynamic water balance model that could accurately predict the water balance in ungauged basins and assess impacts of land-use/land-cover changes. Moreover, the model should account for the snow representation since snowmelt water has been a significant source of water resources, especially in high elevation or northern regions in the United States. (**presented in Chapter 3**).
3. There is no unified definition of wet/dry rainfall extreme that has been universally accepted or shown to work in all climate regions across the United

States. In addition, annual manifestations of simultaneous wet and dry extremes can have a spatiotemporal interdependence subjected to large-scale climate conditions, but it has been less explored. (**presented in Chapter 4**).

## 1.2 Science Questions

This dissertation focuses on understanding the overall hydroclimatology of the United States and is ultimately expected to be a critical source for hydrologists, climate scientists, natural hazard prevention and mitigation agencies, infrastructure managers and water resources stakeholders.

The research questions that are going to be addressed in this dissertation are listed below:

Question 1: How do we better understand the dynamic procedures of water yielding process at a catchment scale due to natural and human-induced changes?

Question 2: Do dams have a cumulative impact on the fluvial network of a basin? If so, can it be quantified and compared to their local impacts? What are the proxy indicators that can significantly explain the spatial variabilities of the cumulative and regional effects of dams on streamflow alteration?

Question 3: How has the annual and multi-annual frequency component of streamflow changed over time across the river network in the Colorado River Basin? Which dams have shown significant impact on the frequency alteration?

Question 4: What are the limitations of the existing Budyko-based dynamic water balance models in predicting the water balance of catchments in the

United States? How can we incorporate the snow melting process into an existing water balance model while minimizing model complexity yet sufficiently reflecting the physical aspects? What are the primary catchment characteristics that influence the water balance? Can we model their time-varying aspect? How can water balance models be improved to understand these controls better?

Question 5: Can we systematically model and identify simultaneous meteorological floods and droughts without any artificial thresholds? What are the chances to have an unexpected spatiotemporal extreme event for each catchment in the United States every year? Are there any large-scale climate signals driving the manifestation of those unexpected events?

### 1.3 Scientific Contributions

The findings of this dissertation contribute to improving the current and future water resources management by advancing our knowledge of the overall hydrosystems in the United States. The systematic exploration of modified basins conducted in this study could help restore and develop environmental flow operations in highly regulated river basins by informing the selection of sites. As part of the study, moreover, a novel water balance model is developed and applied to unmodified (natural) basins across the conterminous United States, providing further insights into the complex water yielding process of catchments. Relating the spatiotemporal interdependence between simultaneous wet/dry rainfall extremes to large-scale climate processes promote our ability to predict those events in advance. The enhanced understanding of both modified and unmodified basins, considering their possible extreme conditions, will improve the current water resources

management and help to establish a mitigation plan.

## **1.4 Dissertation Structure**

This dissertation comprises of five chapters. Chapter 1 is an introduction to the scientific problem. Chapters 2, 3, and 4 form the main contents of this dissertation. Each chapter starts with a summary and a comprehensive introduction and literature review before explaining the data processing and methodology. There are complete results and discussion sections for each chapter, and the concluding remarks and highlights are presented at the end of each chapter, in addition to the supplementary information (if any). Finally, Chapter 5 underlines the concluding remarks and future works.

# References

- Andreadis, K.M. and D.P. Lettenmaier (2006). "Trends in 20th century drought over the continental United States". en. In: *Geophysical Research Letters* 33.10.
- Andrés Doménech, I., R.L. García Bartual, A. Montanari, M. Segura, and J. Bautista (2015). "Climate and hydrological variability: the catchment filtering role". en. In: *Hydrology and Earth System Sciences* 19.1, pp. 379387.
- Armal, S., N. Devineni, and R. Khanbilvardi (2018). "Trends in extreme rainfall frequency in the contiguous United States: Attribution to climate change and climate variability modes". en. In: *Journal of Climate* 31.1, pp. 369385.
- Budyko, M.I. (1961). "The heat balance of the earth's surface". en. In: *Soviet Geography* 2.4, pp. 313.
- Dai, A. (2013). "Increasing drought under global warming in observations and models". en. In: *Nature climate change* 3.1, pp. 5258.
- Eagleson, P.S. (1978). "Climate, soil, and vegetation: 1. Introduction to water balance dynamics". en. In: *Water Resources Research* 14.5, pp. 705712.
- Farmer, D., M. Sivapalan, and C. Jothityangkoon (2003). "Climate, soil, and vegetation controls upon the variability of water balance in temperate and semiarid landscapes: Downward approach to water balance analysis". en. In: *Water Resources Research* 39.2.
- Graf, W.L. (1999). "Dam nation: A geographic census of American dams and their largescale hydrologic impacts". en. In: *Water resources research* 35.4, pp. 13051311.
- Graf, W.L. (2006). "Downstream hydrologic and geomorphic effects of large dams on American rivers". en. In: *Geomorphology* 79.3-4, pp. 336360.
- Hartmann, D.L., A.M.K. Tank, M. Rusticucci, L.V. Alexander, S. Brönnimann, Y.A.R. Charabi, and B.J. Soden (2013). *Observations: atmosphere and surface. In Climate change 2013 the physical science basis: Working group I contribution to the fifth assessment report of the intergovernmental panel on climate change*. en. Cambridge University Press, pp. 159254.
- Hodgkins, G.A., P.H. Whitfield, D.H. Burn, J. Hannaford, B. Renard, K. Stahl, and C. Murphy (2017). "Climate-driven variability in the occurrence of major floods across North America and Europe". en. In: *Journal of Hydrology* 552, pp. 704717.

- Ivancic, T.J. and S.B. Shaw (2015). "Examining why trends in very heavy precipitation should not be mistaken for trends in very high river discharge". en. In: *Climatic Change* 133.4, pp. 681693.
- Kunkel, K.E., T.R. Karl, H. Brooks, J. Kossin, J.H. Lawrimore, D. Arndt, and K. Emanuel (2013). "Monitoring and understanding trends in extreme storms: State of knowledge". en. In: *Bulletin of the American Meteorological Society* 94.4, pp. 499514.
- Milly, P.C.D. (1994). "Climate, soil water storage, and the average annual water balance". en. In: *Water Resources Research* 30.7, pp. 21432156.
- Poff, N.L., J.D. Olden, D.M. Merritt, and D.M. Pepin (2007). "Homogenization of regional river dynamics by dams and global biodiversity implications". en. In: *Proceedings of the National Academy of Sciences* 104.14, pp. 57325737.
- Ruhi, A., X. Dong, C.H. McDaniel, D.P. Batzer, and J.L. Sabo (2018). "Detimental effects of a novel flow regime on the functional trajectory of an aquatic invertebrate metacommunity". en. In: *Global change biology* 24.8, pp. 37493765.
- Sahagian, D.L., F.W. Schwartz, and D.K. Jacobs (1994). "Direct anthropogenic contributions to sea level rise in the twentieth century". en. In: *Nature* 367.6458, pp. 5457.
- Sivapalan, M., K. Takeuchi, S.W. Franks, V.K. Gupta, H. Karambiri, V. Lakshmi, and T. Oki (2003). "IAHS Decade on Predictions in Ungauged Basins (PUB), 20032012: Shaping an exciting future for the hydrological sciences". en. In: *Hydrological sciences journal* 48.6, pp. 857880.
- Sterling, S. and A. Ducharme (2008). "Comprehensive data set of global land cover change for land surface model applications". en. In: *Global Biogeochemical Cycles* 22.3.
- Vogel, R.M., U. Lall, X. Cai, B. Rajagopalan, P.K. Weiskel, R.P. Hooper, and N.C. Matalas (2015). "Hydrology: The interdisciplinary science of water". en. In: *Water Resources Research* 51.6, pp. 44094430.
- Vogel, R.M., C. Yaindl, and M. Walter (2011). "Nonstationarity: flood magnification and recurrence reduction factors in the United States 1". en. In: *JAWRA Journal of the American Water Resources Association* 47.3, pp. 464474.
- Vörösmarty, C.J. (1997). "The storage and aging of continental runoff in large reservoir systems of the world". en. In: *Ambio* 26, pp. 210219.
- Vörösmarty, C.J., P.B. McIntyre, M.O. Gessner, D. Dudgeon, A. Prusevich, P. Green, and P.M. Davies (2010). "Global threats to human water security and river biodiversity". en. In: *Nature* 467.7315, pp. 555561.
- Vörösmarty, C.J., C. Pahl-Wostl, S.E. Bunn, and R. Lawford (2013). "Global water, the anthropocene and the transformation of a science". en. In: *Current Opinion in Environmental Sustainability* 5.6, pp. 539550.
- Vörösmarty, C.J. and D. Sahagian (2000). "Anthropogenic disturbance of the terrestrial water cycle". en. In: *Bioscience* 50.9, pp. 753765.

- Weather, U.S.Billion-Dollar and Climate Disasters (2020). NOAA *National Centers for Environmental Information (NCEI)*. it. URL: <https://www.ncdc.noaa.gov/billions/>.
- Zhou, G., X. Wei, X. Chen, P. Zhou, X. Liu, Y. Xiao, and Y. Su (2015). "Global pattern for the effect of climate and land cover on water yield". en. In: *Nature communications* 6.1, pp. 19.

# Chapter 2

## Quantifying Dam-Induced Fluctuations in Streamflow Frequencies Across the Colorado River Basin<sup>1</sup>

### 2.1 Summary

Periodic fluctuations in streamflow are a major driver of river ecosystem dynamics and water resource management. Most U.S. rivers are impacted by long-term hydroclimatic trends and dams that alter flow variability. However, whether and how dams affect the dominant frequencies of streamflow remains largely unexplored. Here we explored the highly regulated Colorado River Basin to understand how the annual (10-14 months) and multi-annual (24-60 months) frequencies in the flow regimes have been historically altered as affected by dams and free-flowing tributaries. The frequency changes in the streamflow network are captured across the Colorado River Basin based on wavelet analysis using observed and naturalized monthly streamflow datasets. Based on the similarity of historical changes

---

<sup>1</sup>Hwang, J. and Devineni, N., 2021, Quantifying Dam-Induced Fluctuations in Streamflow Frequencies Across the Colorado River Basin, *Water Resources Research*, accepted subject to minor revision.

in streamflow frequency over the last 30 years, the riverine network is classified into four groups for each annual and multi-annual frequency band. The annual frequency of the river network had been relatively well preserved downstream of Hoover Dam, while it showed a systematic trend of alteration downstream of Glen Canyon Dam until it reaches Hoover Dam. Meanwhile, the multi-annual frequency component had been highly altered downstream of both Glen Canyon and Hoover dams. We also identified dams with significant impacts on streamflow frequency by comparing wavelet coherence estimates. This study advances the notion that dams fundamentally alter flow regimes in multiple frequencies with varying amplitudes in space and time across the basin and alteration may propagate or ameliorate by both hydroclimate and management across river networks.

## 2.2 Introduction

As water demand drastically increased due to growing population and urbanization, a vast installation of reservoirs proliferated worldwide, fundamentally changing the water cycle (Ripl, 2003). Large-scale water regulation and conveyance systems currently determine current and future water availability to society (Vörösmarty and Sahagian, 2000; Sivapalan et al., 2003; Vogel et al., 2015). In the U.S. alone, more than 90,000 dams change the quantity and variability of natural flow regimes, altering more than 85% of the inland waterways (Council, 1992). The impacts of such alteration propagate through river networks and affect the fluvial ecosystem in multiple ways: by preventing sediment transport (Willis and Griggs, 2003), by stabilizing channel morphology (Brandt, 2000; Topping, Rubin, and Vierra Jr, 2000; Graf, 2006), or by altering the composition and dynamics of aquatic biota (Poff et al., 2007; Bunn and Arthington, 2002).

Many studies have investigated dam-induced flow alteration, mostly by estimating the proportion of annual flows that can be withheld by a dam or cluster of dams (Vörösmarty et al., 1997; Graf, 1999; Nilsson et al., 2005; Lehner et al., 2011; Grill et al., 2014; Grill et al., 2015; Mailhot et al., 2018). However, this metric does not capture whether flow alteration is affecting the periodic (signal) or stochastic (noise) components of streamflow, or variation in alteration over time. Streamflow periodicity is a critical element in water supply and hydropower generation planning (Koch et al., 2011). It is also critical to many species in the riparian and aquatic habitats, as their life histories have evolved in responses to, and are coupled with, cyclical, predictable high and low flows (Lytle and Poff, 2004). Additionally, previous studies largely focused on long-term impacts of dams on flow regimes providing a single time-invariant estimate that averages any fluctuations in alteration. Because dam operations change over time with dam specific objectives and regional climatic conditions, there is increasing recognition that time-invariant metrics may not be sufficient to explain streamflow alteration and its impacts (Poff, 2018; Ruhi et al., 2018). Developing time-varying flow-alteration metrics may help better understand the transience of hydrologic conditions in river basins dominated by dams as well as their impacts. In addition, showing the local and watershed-scale spatiotemporal variability of the streamflow alteration, which shapes the biota and ecosystem processes along river networks, may help prioritize selection of sites for restoration (Palmer and Ruhi, 2019).

Streamflow variability is typically expressed in both time (Thomas, 1962; Box, Jenkins, and Reinsel, 1970) and frequency domains (Milly and Wetherald, 2002; Patkoski, Sankarasubramanian, and Wang, 2015) over various spatial scales. More recently, wavelet transforms, which permit the orthogonal decomposition of the

original series into both time and frequency domains, have been applied to many geophysical time series (Farge, 1992; Weng and Lau, 1994; Hubbard, 1996; Wang and Wang, 1996; Kulkarni, 2000; Kwon et al., 2006; Kwon, Lall, and Khalil, 2007; Foufoula-Georgiou and Kumar, 2014). Some studies demonstrated the usefulness of wavelet analysis for assessing post-dam operational discharge modulations at specific frequencies (White, Schmidt, and Topping, 2005; Ruhi et al., 2018). Wavelet analysis provides information on the frequency at all scales and times with a single spectrum image that is easy to interpret, can be used when management history is uncertain, and performs well even if the underlying data (e.g., streamflow) is non-stationary due to external forcing (e.g., climate change) and local management. Building on the univariate wavelet transform, wavelet coherence examines the relationship of two time series in the time-frequency domain (Torrence and Compo, 1998; Grinsted, Moore, and Jevrejeva, 2004), making it an ideal tool to assess how time-varying flow alteration may propagate across a river network.

Here we performed wavelet coherence analysis based on the wavelet transforms of controlled (observed) and naturalized (modeled free-flowing) streamflow data. This analysis allowed us to explore the degree of alteration in streamflow over time-focusing on its annual and multi-annual frequencies. The Colorado River Basin, a highly regulated fluvial network, is used for demonstration purposes. Similarities in the degree of alteration across the basin were quantified using the dynamic time warping clustering method. We considered that wavelet coherence represents the cumulative alteration of streamflow due to both climate and human activities. Controlled flows are the product (resultant flow) of regional climate forcing, basin characteristics, and anthropogenic factors. In contrast, naturalized

flows were derived by removing the anthropogenic factors. Wavelet coherence between the two (natural and controlled flows) measures the local correlation in the time-frequency space, revealing locally phase-locked behavior (Grinsted, Moore, and Jevrejeva, 2004). Whereas a high coherence at a given frequency and during a time-period indicates little to no alteration, a low coherence suggests high alteration. As we quantified the degree of alteration, we also identified dams with significant impacts on local and basin-wide alterations. We primarily focused on the annual and multi-annual frequencies since streamflow seasonality (i.e., the cycle of high and low flows) occurs with a regular annual periodicity, and large-scale climate effects manifest at a multi-annual scale.

In this paper, we first provide a description of the study area, sites, and the data sources, including their measurement methods. We then present an overview of the wavelet transform and wavelet coherence analysis and describe the clustering method applied to the time-varying wavelet coherence loss. A synthetic experiment to understand the wavelet coherence time-series' fundamental behavior to changes in the original signals' frequency and amplitude is also demonstrated. We then identify clusters of locations where streamflow shows similar time-varying patterns in wavelet coherence loss and discuss the wavelet coherence analysis for each cluster. Finally, we identify dams with significant impacts on their local streamflow frequency and discuss the significance of our approach to quantify time-varying flow alteration in the frequency domain, and how it propagates across a river network.

## 2.3 Data

### 2.3.1 The Colorado River Basin and its Importance for Water Management

We focused on the Colorado River Basin (CRB) owing to its high levels of regulation, data availability, and importance for water resources management in the United States. Starting from Wyoming and Colorado, the Colorado River flows for about 1,450 miles until it crosses the international border with Mexico (Figure 2.1). The total drainage area is about 246,000 square miles, and extends over seven U.S. states: Arizona, California, Colorado, New Mexico, Nevada, Utah, and Wyoming. More than 25 million people and 3 million acres of croplands depend on the Colorado River for water supply (Bruce, 2012). Colorado River water is partially diverted to serve Denver, Salt Lake Valley, Albuquerque, Cheyenne, Los Angeles, San Diego, and Imperial Valley in California. In this basin, more than 1,400 dams exist, including Hoover Dam and Glen Canyon Dam (which impound the two largest reservoirs in the U.S.). The CRB is commonly divided into two parts, the Upper (UCRB) and the Lower Colorado River Basin (LCRB), located upstream and downstream of Lees Ferry (immediately downstream of Glen Canyon Dam), respectively. The UCRB includes most of the headwaters of the Colorado River, while the LCRB comprises the strongly-regulated and heavily-altered downstream section.

### 2.3.2 Naturalized Flow Data

Monthly time series of naturalized streamflow, developed by the United States Bureau of Reclamation, is available for 26 streamflow sites over CRB. Historical data of monthly consumptive uses and losses, reservoir regulations, and historic

flow in CRB are taken into account to calculate the naturalized streamflow (Prairie and Callejo, 2005). Monthly consumptive uses and losses in the UCRB are obtained at a USGS hydrologic unit code (HUC) based on Consumptive Uses and Losses Reports, which have been published every five years since 1971. For the LCRB, Decree Accounting records of water use were utilized to determine the consumptive uses and losses. The historic reservoir regulation data accounts for water storage and release from 12 mainstem reservoirs and 25 off-stream reservoirs located within the basin. The resultant naturalized flow covers 111 years ranging from 1906 to 2016, at a monthly scale.

### 2.3.3 Observed Flow Data

At the 26 USGS streamflow gauging stations with available naturalized streamflow, monthly streamflow records have been continuously reported for at least 30 years between 1906 and 2016. Their observed monthly streamflow data are retrieved from the USGS National Water Information System (NWIS). The period of record varies by station (average length of 79 years), and the common period of record begins in 1987. As this study intends to explore the level of alteration in the streamflow relative to its natural state, a wavelet coherence analysis between the monthly naturalized and observed streamflow was carried out for 30 years starting from 1987 to 2016. Since most of the dams in the basin were constructed before 1987, coherence analysis after this period provides a complete dam-induced alteration signal. The spatial distribution of the selected USGS streamflow gauging stations is shown in Figure 2.1. For convenience, each station is assigned with an index number as listed in Table 2.1, and their location is described as well in the table.

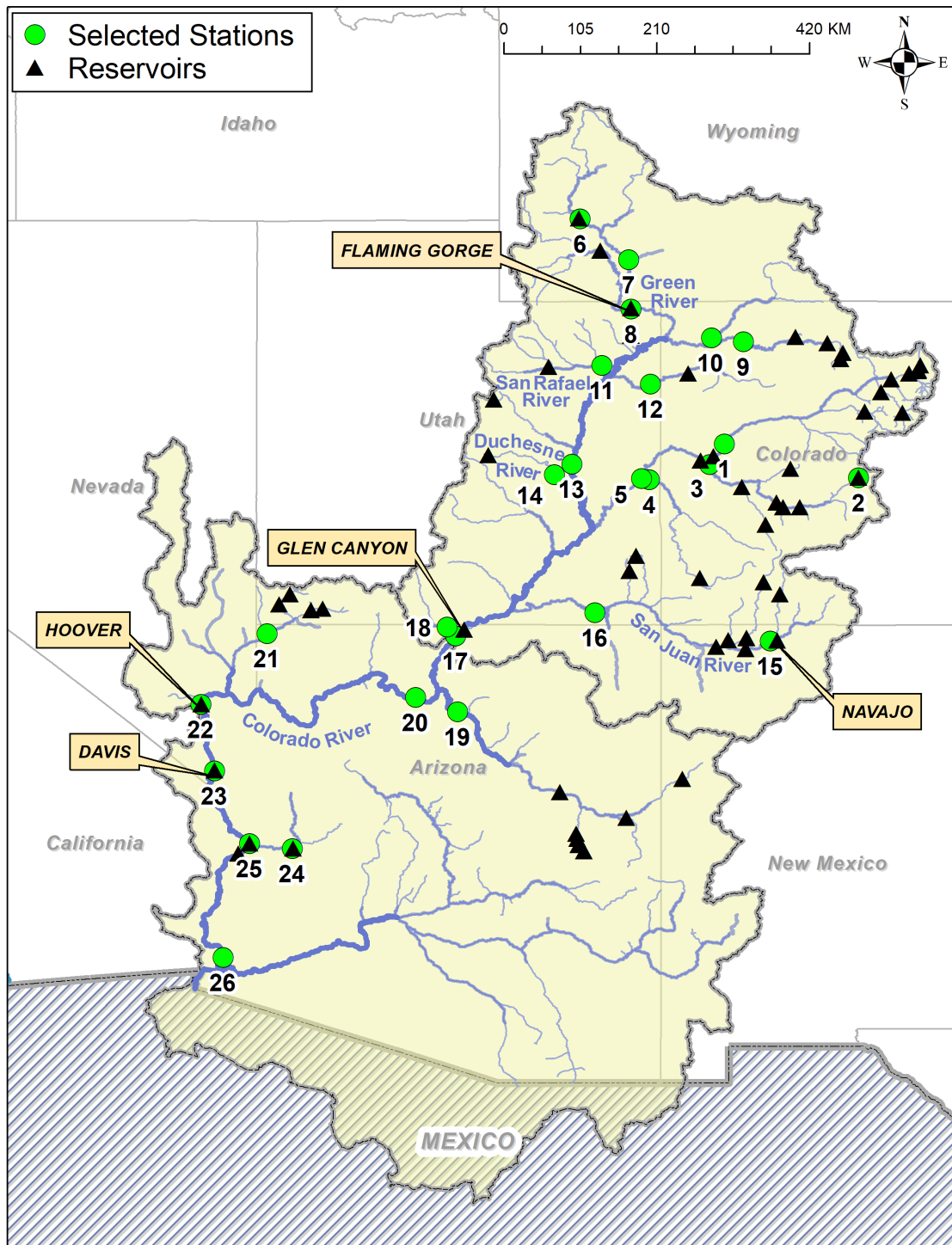


**Figure 2.1:** Spatial distribution of the 26 selected USGS streamflow gauging stations and 61 intermediate-to-large NID dams across the Colorado River Basin (including both Upper and Lower Colorado Basins). Station numbers are also presented.

<b>Index Number</b>	<b>NWIS Site Number</b>	<b>NWIS Site Name (Description of Location)</b>
1	9095500	COLORADO RIVER NEAR CAMEO, CO.
2	9109000	TAYLOR RIVER BELOW TAYLOR PARK RESERVOIR, CO.
3	9152500	GUNNISON RIVER NEAR GRAND JUNCTION, CO.
4	9180000	DOLORES RIVER NEAR CISCO, UT
5	9180500	COLORADO RIVER NEAR CISCO, UT
6	9211200	GREEN RIVER BELOW FONTENELLE RESERVOIR, WY
7	9217000	GREEN RIVER NEAR GREEN RIVER, WY
8	9234500	GREEN RIVER NEAR GREENDALE, UT
9	9251000	YAMPA RIVER NEAR MAYBELL, CO
10	9260000	LITTLE SNAKE RIVER NEAR LILY, CO
11	9302000	DUCHESNE RIVER NEAR RANDLETT, UT
12	9306500	WHITE RIVER NEAR WATSON, UT
13	9315000	GREEN RIVER AT GREEN RIVER, UT
14	9328500	SAN RAFAEL RIVER NEAR GREEN RIVER, UT
15	9355500	SAN JUAN RIVER NEAR ARCHULETA, NM
16	9379500	SAN JUAN RIVER NEAR BLUFF, UT
17	9380000	COLORADO RIVER AT LEES FERRY, AZ
18	9382000	PARIA RIVER AT LEES FERRY, AZ
19	9402000	LITTLE COLORADO RIVER NEAR CAMERON, AZ
20	9402500	COLORADO RIVER NEAR GRAND CANYON, AZ
21	9415000	VIRGIN RV AT LITTLEFIELD, AZ
22	9421500	COLORADO RV BLW HOOVER DAM, AZ-NV
23	9423000	COLORADO RIVER BELOW DAVIS DAM, AZ-NV
24	9426000	BILL WILLIAMS RIVER BELOW ALAMO DAM, AZ
25	9427520	COLORADO RIVER BELOW PARKER DAM, AZ-CA
26	9429490	COLORADO RIVER ABOVE IMPERIAL DAM, AZ-CA

**Table 2.1:** Details of the USGS streamflow gauging stations used in the study.

### 2.3.4 Criteria for Dam Selection

According to the National Inventory of Dams (NID) database, 1,455 dams are present in CRB, fulfilling various purposes (mainly hydropower, flood control, water supply and irrigation). Here we only consider intermediate to large dams, i.e., those with a height greater than 12.2 meters or a storage capacity larger than 1.23 million cubic meters, following the definition of the American Society of Civil Engineering (Snyder, 1964). This procedure returned 61 dams (Figure 2.1), which are assumed to impact the riverine system where the 26 streamflow gauges are located. Most of these selected dams were constructed before 1987, and their cumulative capacity is > 99.9% of the total storage of the selected dams. Therefore, it is reasonable to assume that further dam construction post-1987 had much lesser impacts on flow regime alteration through new capacity additions. The connectivity between the selected dams and streamflow gauges is developed based on the River and Infrastructure Connectivity Network (RICON) tool, which systematically combines three geospatial information; the National Hydrographic Dataset (NHDPlusV2), streamflow gauges from the USGS National Water Information System, and NID reservoirs (Mukhopadhyay, Sankarasubramanian, and Awasthi, 2020).

## 2.4 Method

We take both the naturalized and controlled streamflow series for each station and compute the wavelet coherence spectrum between them. In this case, the wavelet coherence spectrum results in a localized coefficient for each of the 256 frequency scales over the 360 months. The wavelet coherence spectrum between the 10-months and 14-months frequency scales is selected and averaged into the

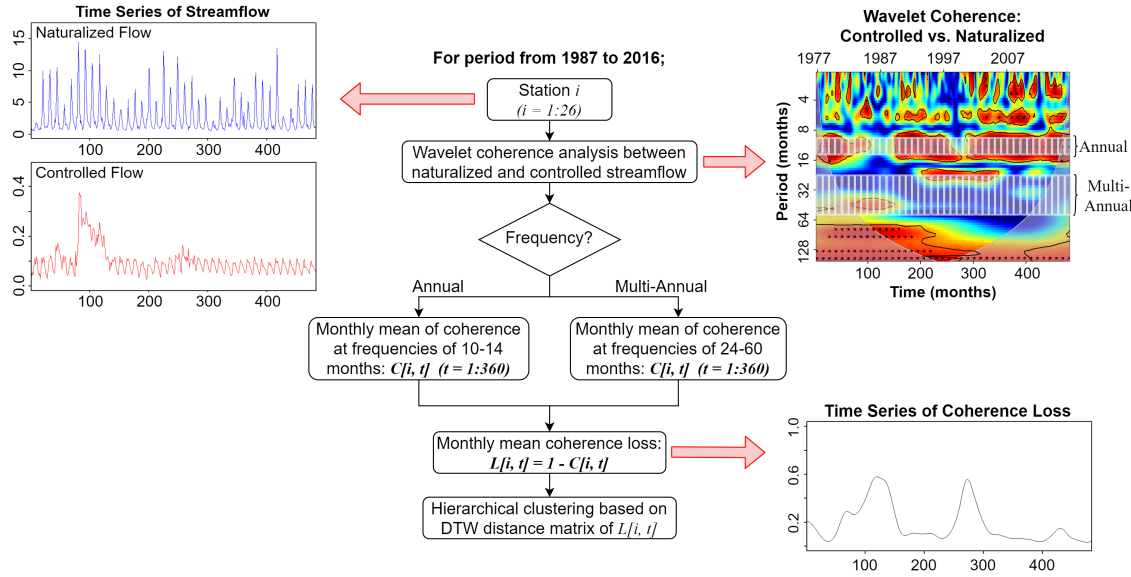


**Figure 2.2:** Methodological flowchart for the wavelet coherence analysis.

annual frequency band across the entire time. Similarly, for the multi-annual frequency band, the wavelet coherence spectrum for frequency scales between 24-months and 60-months is selected and averaged for each time period. The scale-averaged wavelet coherence loss for each frequency band is then computed by subtracting the wavelet coherence from 1. This scale-averaged wavelet coherence loss time-series measures the degree of alteration over time. We finally group stations with similar time-varying wavelet coherence loss for each frequency band using the dynamic time warping hierarchical clustering method to understand the regional alterations.

In the following sub-sections, we provide details on the wavelet transform, wavelet coherence, and dynamic time warping hierarchical clustering methods. In Figure 2.2, we present the workflow diagram for the systematic approach that was carried out in this study.

### 2.4.1 Wavelet Transform

As this study investigates the level of alteration in the streamflow relative to its natural state in terms of time and frequency, wavelet coherence between monthly naturalized and controlled (observed) streamflow is determined. Decomposing a time series into a time-frequency domain allows for localizing intermittent periodicities across scales (Torrence and Compo, 1998). This process conjugates the given time series with a flexible wavelet function, which can be temporally dilated/compressed while it translates along the timesteps. High-frequency features of a given time series can be captured with a wavelet function narrow in time, whereas low-frequency components can be analyzed with a dilated wavelet function. A variety of wavelet functions (or mother wavelets) are available; here, we implement the Morlet wavelet, defined as,

$$\psi_0(\eta) = \pi^{-1/4} e^{iw_0\eta} e^{-\eta^2/2} \quad (2.1)$$

where  $w_0$  and  $\eta$  are the dimensionless frequency and time, respectively. The non-dimensional frequency of the Morlet wavelet is set as 6 in this study to satisfy the wavelet admissibility (Farge, 1992). This complex wavelet function returns information about both the amplitude and phase, and thus makes itself applicable for describing wave-like oscillatory behaviors such as streamflow and precipitation (Kumar and FoufoulaGeorgiou, 1997; Torrence and Compo, 1998; Labat, 2005). The continuous wavelet transform of a discrete time series ( $x_n$ ) with equal time spacing of  $t$  is defined as the convolution with a scaled and normalized wavelet

function (Torrence and Compo, 1998) as

$$W_b^X(a) = \sqrt{\frac{\delta t}{a}} \sum_{n=1}^N x_n \psi_0 \left[ (n - b) \frac{\delta t}{a} \right] \quad (2.2)$$

where  $W_b^X(a)$  is the wavelet spectrum,  $a$  is the scale parameter,  $b$  is the localized time index, and  $N$  is the total number of sample points in the time series. It should be noted that the wavelet function is normalized to unit energy at each scale in Eq. 2.2 to ensure the wavelet transforms at each scale are directly comparable. The convolution is done for  $N$  times for each scale to estimate the wavelet power spectrum in both time and frequency scales, and the wavelet power is defined as  $|W_b^X(a)|^2$ .

### 2.4.2 Wavelet Coherence

Wavelet coherence is a quantity that describes the coherence between two different time series based on their cross-wavelet transforms as a function of both time and frequency. Given two time series X and Y, the cross-wavelet spectrum is defined as

$$W_b^{XY}(a) = W_b^X(a) W_b^{Y*}(a) \quad (2.3)$$

where  $*$  denotes the complex conjugate. The cross-wavelet spectrum reveals the covariance between the time series as a function of time and frequency. By dividing the square of the absolute value of the smoothed cross-wavelet power with

smoothed wavelet power spectra, one can obtain the wavelet coherence,  $R^2$  (Torrence and Webster, 1999):

$$R^2 = \frac{|\langle a^{-1} W_b^{XY}(a) \rangle|^2}{\langle a^{-1} |W_b^X(a)|^2 \rangle \cdot \langle a^{-1} |W_b^Y(a)|^2 \rangle} \quad (2.4)$$

This provides a quantity ranging from 0 to 1, representing the localized correlation coefficient in time and frequency space (Grinsted, Moore, and Jevrejeva, 2004). The brackets  $\langle \cdot \rangle$  in Eq. 2.4 indicate smoothing in both time and scale. For the Morlet wavelet, the temporal smoothing operator is a Gaussian function,  $e^{-t^2/(2s^2)}$ , while the scale smoothing is done using a boxcar filter. For a more elaborate description of the wavelet coherence, see Torrence and Webster (1999).

We are interested in knowing how the wavelet coherence between the naturalized and controlled flow evolves over time at the annual and multi-annual frequency bands. To this end, we compute the scale-averaged coherence for each time step based on each frequency band of the annual frequency (10–14 months) and multi-annual frequency (24–60 months) from 1987 to 2016. In turn, the coherence loss at each timestep is simply calculated by subtracting the coherence value from 1. This procedure yields a time series of the wavelet coherence loss of the controlled flow relative to its naturalized flow at the annual and multi-annual frequency bands. We should note that the resolution of a continuous wavelet transform is determined by the tradeoff between the temporal resolution and frequency resolution of the wavelet. Higher frequency features of a given time series are captured with good temporal resolutions. In contrast, lower frequency components can only be captured with modest temporal resolutions as it is required to have sufficiently long time series to resolve the low frequencies better. This indicates that we can retain the temporal accuracy of the scale-averaged wavelet coherence

loss in the annual frequency scale, whereas the scale-averaged wavelet coherence loss in the multi-annual frequency scale contains less accurate temporal information. For multi-annual features, therefore, we only focus on the long-term trend rather than explaining them locally.

### 2.4.3 Dynamic Time Warping Based Hierarchical Clustering

To explain the regional discordance between controlled and naturalized flow across the basin, stations are clustered in groups based on their scale-averaged time-varying wavelet coherence loss from 1987 to 2016. Euclidean distance is typically used as a similarity measure for clustering. However, as Euclidean distance is determined by aligning the  $i$ -th point in one sequence with the  $i$ -th point in the other, it is susceptible to phase lags and outliers, which is a critical aspect, especially when clustering the cascading streamflow. Thus, we implement the dynamic time warping (DTW) technique instead, providing a robust distance metric for similarity quantification. Unlike the Euclidean distance, DTW is a flexible measure that can detect the similarities between time series, even if they are out of phase in time (Berndt and Clifford, 1994). For further details, see Berndt and Clifford (1994) and Keogh and Ratanamahatana (2005). Based on the DTW similarity measures, the wavelet coherence loss dynamics at different stations are grouped using the hierarchical clustering method. The optimal number of clusters is determined based on the elbow method (Thorndike, 1953). The impact of anthropogenic regulations and climatic forcings on the wavelet coherence loss are explored based on the resultant clusters.

#### 2.4.4 Wavelet Coherence Interpretation under Known Signals

Before we begin interpreting the wavelet coherence loss results for the CRB, we performed wavelet coherence under known time series signals, which we call as experiments. These experiments provide the sensitivity of the wavelet coherence to changes in the wave components of signals in specific frequency bands. For this purpose, we created two noiseless identical sinusoidal time series ( $y_1$  and  $y_2$ ) containing both annual and multi-annual frequency signals (equations 2.5 and 2.6):

$$y_1 = A_1 \sin(2\pi f_1 t + \varphi_1) + A_2 \sin(2\pi f_2 t + \varphi_2) \quad (2.5)$$

$$y_2 = A_3 \sin(2\pi f_3 t + \varphi_3) + A_4 \sin(2\pi f_4 t + \varphi_4) \quad (2.6)$$

In the above equations,  $A_1$  and  $A_3$  are the amplitude of the annual signal;  $A_2$  and  $A_4$  indicate the amplitude of the multi-annual signal.  $f_1$  and  $f_3$  signify the annual frequency;  $f_2$  and  $f_4$  are the multi-annual frequency.  $\varphi_1$  and  $\varphi_3$  are the phase lag of the annual signal; and  $\varphi_2$  and  $\varphi_4$  represent the phase lag of the multi-annual signal. In a sequence of six simulations, one of the two time series,  $y_1$ , remains unperturbed, whereas the other,  $y_2$ , is set to have the signal characteristics change over time. Each simulation focused on one frequency band at a time and measured the wavelet coherence between the two given time series while ensuring one wave component changes over time while the rest remain constant. For example, in the first simulation, the amplitude of the second time series that relates to the annual frequency ( $A_3$ ) is altered three times over the 1,500 time periods. Between  $t = 1$  to  $t = 375$ ,  $A_3 = 1$ ; between  $t = 376$  to  $t = 750$ ,  $A_3 = 2/3$ ; between  $t = 751$  to  $t = 1125$ ,  $A_3 = 1/3$ ; and between  $t = 1126$  to  $t = 1500$ ,  $A_3 = 0$ ; hence creating

<b>Frequency Band</b>	<b>Wave Component</b>	<b>Simulation</b>	<b>Description</b>
Annual	Amplitude	$A_1 = 1$ (Constant) $A_3 = 1, \frac{2}{3}, \frac{1}{3}, 0$	Significant change in wavelet coherence is observed only when the amplitude was completely diminished
	Phase Lag	$\varphi_1 = 0$ (Constant) $\varphi_3 = 0, \frac{\pi}{4}, \frac{\pi}{2}, \pi, 0$	Wavelet coherence instantaneously fluctuates whenever the phase lag changes by $\pi$
	Frequency	$f_1 = 12$ (Constant) $f_3 = 12, 13, 15, 17$	A permanent shift in the wavelet coherence is observed whenever there is a change in the frequency
Multi-Annual	Amplitude	$A_2 = 1$ (Constant) $A_4 = 1, \frac{2}{3}, \frac{1}{3}, 0$	Significant change in wavelet coherence is observed only when the amplitude was completely diminished
	Phase Lag	$\varphi_2 = 0$ (Constant) $\varphi_4 = 0, \frac{\pi}{4}, \frac{\pi}{2}, \pi, 0$	Wavelet coherence instantaneously fluctuates whenever the phase lag changes by $\pi$
	Frequency	$f_2 = 48$ (Constant) $f_4 = 48, 49, 54, 60$	A permanent shift in the wavelet coherence is observed whenever there is a change in the frequency

**Table 2.2:** Summary of Wavelet Coherence Simulation.

a time series where the amplitude systematically tapers off to zero. Likewise, in the second and third simulation, the phase lag ( $\varphi_3$ ) and the frequency ( $f_3$ ) is altered systematically. The amplitude ( $A_4$ ), phase lag ( $\varphi_4$ ) and frequency ( $f_4$ ) of the multi-annual band are altered in simulations four to six. It should be noticed that phase lag components are altered four times over the 1,500 time periods during the simulations. The details of the six simulations are summarized in Table 2.2.

For both frequency bands, changes in the amplitude resulted in a temporary drop in the wavelet coherence, followed by an immediate recovery (Figure 2.3a

and Figure 2.3d). Unless the amplitude of the frequency signal was completely removed, changes in the amplitude had a minor impact on wavelet coherence. When the amplitude was entirely diminished, the wavelet coherence exhibited a significant downward shift.

Wavelet coherence finds locally phase-locked behaviors (Grinsted, Moore, and Jevrejeva, 2004), and therefore, changes in the phase difference between two signals have a minimal impact on the fluctuation of the wavelet coherence at any frequency level (Figure 2.3b and Figure 2.3e). However, it is shown from the simulation that the wavelet coherence drastically decreases and recovers whenever one of the signals changes its phase by  $\pi$ . Instantaneous fluctuations in the wavelet coherence caused by this phase shift can be detected by comparing the phase differences between the signals before and after the expeditious fluctuation.

As expected, the wavelet coherence showed the most sensitive response to changes in the frequency than to other wave components (Figure 2.3c and Figure 2.3f). The wavelet coherence began to shift as soon as the frequency of the signals started to differ from each other. The larger the frequency change, exponentially more the wavelet coherence was lost. During these simulations, it was confirmed that the temporal resolution of the wavelet coherence was relatively lower in the multi-annual frequency band than in the annual frequency band. The wavelet coherence responded immediately to changes in the relationship between the signals in the annual frequency band, while it tended to lag in the multi-annual frequency band. This observation reflects the tradeoff between the temporal resolution and frequency resolution of the wavelet. To summarize the simulations, the fluctuation of the wavelet coherence can be affected by any wave component, but permanent shifts can be induced only by changes in the frequency.

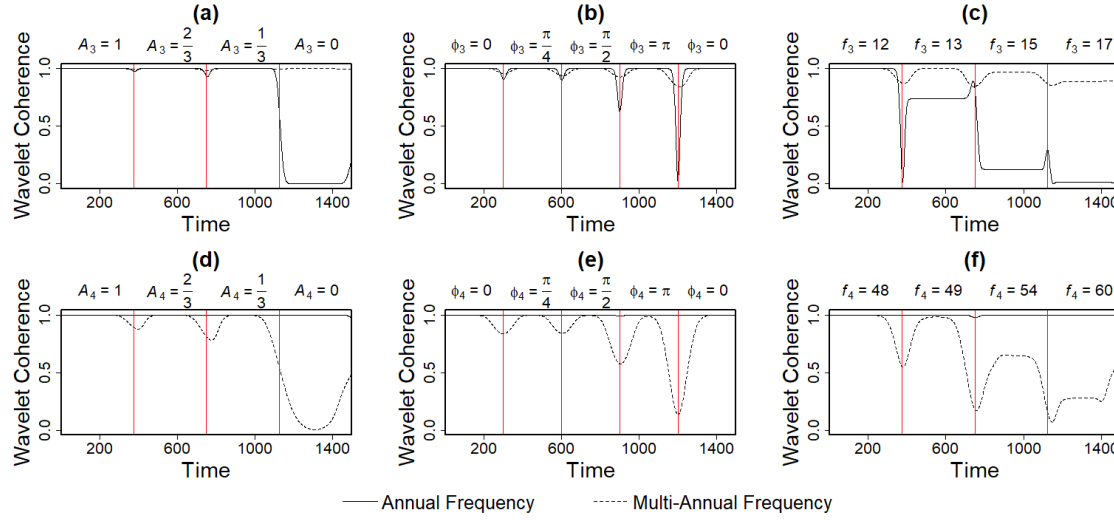


**Figure 2.3:** Results of the wavelet coherence simulations between two synthetic sinusoidal time series  $y_1$  and  $y_2$ . The simulated time series  $y_1$  and  $y_2$  are initially set to be identical to each other, and one wave component of  $y_2$  is forced to change over time for each simulation while the other components are fixed. The time-varying wavelet coherence between  $y_1$  and  $y_2$  is estimated when the amplitude component of the annual signal of  $y_2$  ( $A_3$ ) changes over time (a), when the phase lag component of the annual signal of  $y_2$  ( $\phi_3$ ) changes over time (b), and when the phase lag component of the annual signal of  $y_2$  ( $f_3$ ) changes over time (c). Similarly, the simulation measures the wavelet coherence between  $y_1$  and  $y_2$  when the amplitude component of the multi-annual signal of  $y_2$  ( $A_4$ ) changes over time (d), when the phase lag component of the multi-annual signal of  $y_2$  ( $\phi_4$ ) changes over time (e), and when the phase lag component of the multi-annual signal of  $y_2$  ( $f_4$ ) changes over time (f).

Figure 2.4 presents an example of the wavelet coherence analysis between the naturalized flow and controlled flow after the Glen Canyon Dam. The amplitude of streamflow remarkably decreased after the construction of Glen Canyon Dam (Figure 2.4d and Figure 2.4e), and the annual frequency of streamflow notably diminished (Figure 2.4a and Figure 2.4b). Considering the findings from the controlled experiments, however, the significant decline of the wavelet coherence between naturalized and controlled flow series in both the annual and multi-annual frequency bands (Figure 2.4c and Figure 2.4f) is presumed to be dominantly caused by the distortion in the frequency component of the streamflow. The understandings obtained from this experimental design will be used next to better explain the

wavelet coherence results for the CRB.

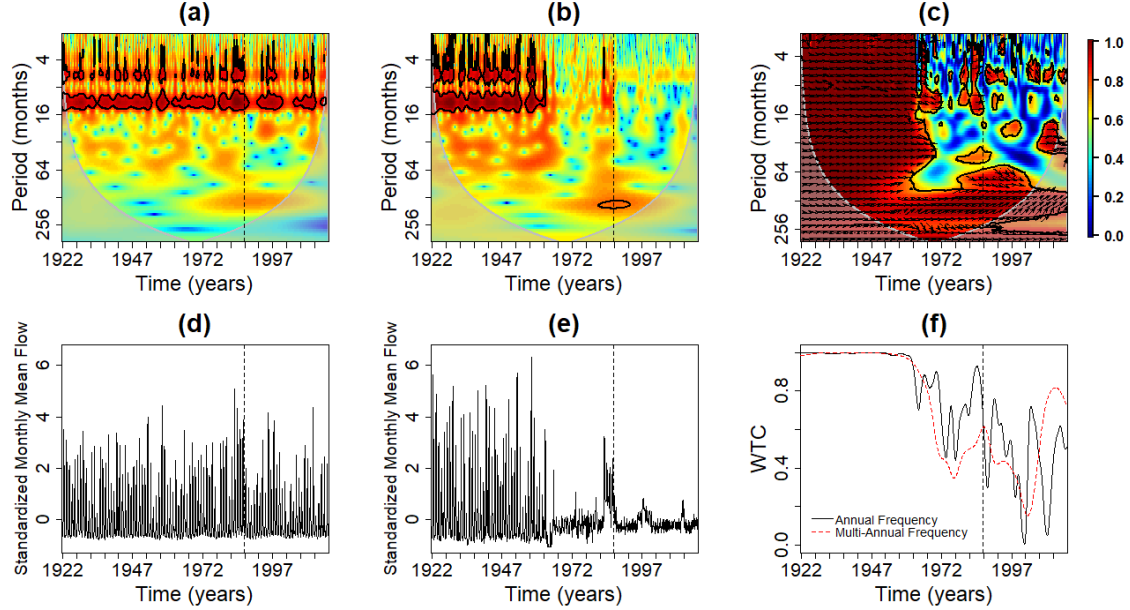


**Figure 2.4:** Wavelet coherence analysis between naturalized flow and controlled flow at the downstream of Glen Canyon Reservoir. Each subplot represents the wavelet power spectrum of the naturalized flow (a), wavelet power spectrum of the controlled flow (b), wavelet coherence spectrum between naturalized and controlled flow series (c), standardized monthly mean flow of the naturalized flow (d), standardized monthly mean flow of the controlled flow (e), and the scale-averaged wavelet coherence between naturalized and controlled flow series for annual and multi-annual frequency bands (f). The dashed line at 1987 indicates the beginning of the period of analysis for our study.

## 2.5 Results and Analysis

As a result of DTW-based hierarchical clustering, the 26 streamflow gaging stations were classified into four clusters for both the annual and multi-annual frequency bands. Figures 2.5 and 2.8 show the stations constituting each cluster and the modalities of the wavelet coherence loss for each cluster in the annual and multi-annual frequency ranges, respectively. Panel (a) of Figures 2.5 and 2.8 show the spatial distribution of the 26 stations and to which cluster they belong. Panels (b) to (e) show the wavelet coherence loss time series for the stations representing

the clusters. While the DTW-based hierarchical clustering is applied on the data from 1987-2016, the wavelet coherence loss for the entire time series is shown in these panels.

Further, the dam constructions are also illustrated in the figures with the evolution of each cluster's cumulative reservoir capacity. The time-varying wavelet coherence loss between the naturalized and controlled streamflow is qualitatively explained for each cluster and frequency band their collective characteristics in relation to the climate and anthropogenic conditions. We assume that naturalized flow represents the climate condition since the influence of anthropogenic interventions was excluded during the process of its derivation. For each station, the mean annual naturalized flow is divided into three categories based on the terciles (33 percentile and 66 percentile), each representing a dry, neutral, and wet year in ascending order.

### 2.5.1 Annual Frequency

Based on the wavelet coherence loss in the annual frequency, the river network of CRB can be divided geospatially into four regions: most rivers in UCRB and tributaries in LCRB (Cluster-1), segment of the Colorado River below Hoover Dam and some tributaries in UCRB (Cluster-2), controlled tributaries in UCRB (Cluster-3), and immediate downstream of Glen Canyon Dam (Cluster-4). The annual frequency component has been relatively well preserved across the basin even in those areas where streamflow is heavily regulated, such as the downstream of Hoover Dam, whereas some tributaries in UCRB have been showing significant variability in the annual wavelet coherence loss. The immediate downstream of Glen Canyon Dam have been systematically losing its annual frequency feature

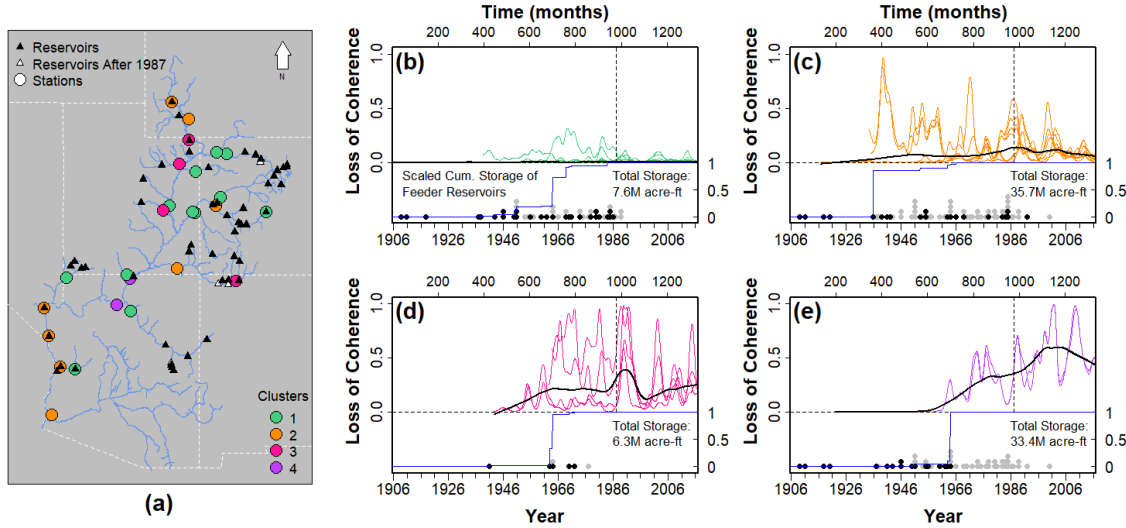


**Figure 2.5:** Cluster profiles based on the wavelet coherence loss of streamflow regarding annual frequency (10–14 months). The spatial distribution of the clusters (a) and time series of the wavelet coherence loss at each cluster (b - e) is shown. Each cluster is assigned with different colors, as shown in the map, and its time series of the wavelet coherence loss is displayed following the same color scheme. Each set of the time-varying wavelet coherence loss is locally fitted (LOWESS) for each cluster and is shown with a solid black line. The vertical dashed line indicates the year of 1987. In the lower part of each subplot of the time-varying wavelet coherence loss, the upstream reservoirs' construction timing is also depicted for each cluster with black and grey points over time. Black points indicate construction of immediate upstream reservoirs, which directly fed the cluster at that time, whereas the grey points represent the installation of upstream reservoirs with indirect impact. The evolution of the immediate upstream reservoirs' total storage capacity is also shown in a scaled measure for each cluster (solid blue line).

since the construction of Glen Canyon Dam.

The first cluster includes eight stations from the UCRB and four stations from the tributaries in the LCRB (Figure 2.5a). The time series of the wavelet coherence loss for these 12 stations show that streamflow has lost coherence with the naturalized flow by less than 33% (low coherence loss) in terms of annual frequency at these stations since 1987 (past 30 years) (Figure 2.5b). This phenomenon indicates that external interventions such as basin management or changes in climate have had little or no impact on the streamflow at these locations.

Cluster-2 consists of eight stations, four of which are located along the Colorado River after the Hoover Dam, and the rest along the tributaries of the UCRB (Figure 2.5a). It is notable to see that the Colorado River below the Hoover dam shows similar behavior to the tributaries in the UCRB in terms of annual frequency. The average wavelet coherence loss is 11%, and an evident temporal variation is also observed at these stations (Figure 2.5c). The probability of the wavelet coherence loss exceeding 66% (high coherence loss) is negligible at these eight stations for the period of 30 years between 1987-2016. The coherence loss was mostly less than 33% (low coherence loss) during those years, regardless of the annual climate conditions. As shown in Figure 2.5c, this cluster consists of two groups of stations that exhibit different behavioral modalities in the earlier years from 1930 to 1980. During this preceding period, the Colorado River after the Hoover Dam exhibits more significant temporal variability in the wavelet coherence loss than that of the latter 30-year period, while the tributaries in the UCRB show a constant behavior.

The third cluster contains four stations in the UCRB, mostly in the tributaries regulated by dams (Green River, San Juan River, San Rafael River, Duchesne River) (Figure 2.5a). The average wavelet coherence loss of the streamflow at these stations is 28%, and a significant interannual variability is observed (Figure 2.5d). The wavelet coherence loss at two of these stations (San Rafael River, Duchesne River) tends to be relatively greater during dry years (e.g., 1988, 1989, 1990, 2002, 2003, 2004). In contrast, the wavelet coherence is preserved during wet years and dry years at the Green River and San Juan River. The probability of the wavelet coherence loss being less than 33% (low coherence loss) is 72% on average across the stations. Even if one breaks this into climatically wet and dry years, the probability remains high (58–81%). The overall probability of the wavelet coherence loss to be

between 33% and 66% (medium coherence loss) is 19%. Depending on the climate, this probability becomes 7% under wet conditions, 25% under neutral conditions, and 25% under dry conditions on average. The probability of the wavelet coherence loss greater than 66% (high coherence loss) at these four stations is computed at 10% on average. Under drier conditions, the wavelet coherence loss exhibits a higher probability of exceedance (11–38%) except at one station (San Juan River), where the exceedance never happens during the given 30-year period.

The wavelet coherence loss estimates at these stations show a synchronized pattern of fluctuation over time since the 1980s. To explain this better, we explored the wavelet coherence between the naturalized flow series of these four stations one with another (i.e., coherence between the natural flows of San Rafael River and Duchesne rivers, San Rafael River and Green River, San Rafael River and San Juan River, Duchesne River and Green River, Duchesne River and San Juan River, Green River and San Juan River) in terms of annual frequency and confirmed a high level of synchronicity regardless of their distant location. This indicates that these four stations have a high degree of co-variability in their naturalized flows. The fact that the wavelet coherence loss estimates at these stations between natural and controlled flows show a synchronized pattern of fluctuation over time since the 1980s also means that they have a high degree of co-variability in the controlled flows, indicating a synchronized alteration similar anthropogenic forcings. In other words, the streamflow at these four stations may have been under similar controls in terms of annual frequency since the 1980s. As shown in Figure 2.5d, significant shifts in the wavelet coherence loss can be observed since 1987. These shifts can occur when the annual frequency is disrupted in either the naturalized or controlled streamflow while it remains in the other. According to the wavelet

power spectrum of the naturalized flow and controlled flow, the controlled flow had a weak annual frequency signal during the shifts, whereas the naturalized flow showed statistically significant annual frequency signals for most of the time at these four stations (Figure 2.6). The significant shift of the wavelet coherence loss that occurred at Cluster-3 in the 1980s is reflected in the Final Biological Opinion on the Operation of Flaming Gorge, which was issued by the U.S. Fish and Wildlife Service in 1992. The opinion stated that Flaming Gorge Dam's operation would endanger the aquatic biota and riparian ecology of the Green River (Fish and Service, 1992). During this time, additional constructions for water storage facilities were planned, and hydrologic assessments suggested that the ecological impact of constructions could be partially counterbalanced by flexibly changing the operation of the Navajo Dam (Fish and Service, 1991). In 1993, the Bureau of Reclamation started to alter the operation of these dams to meet the flow recommendations outlined in the 1992 Final Biological Opinion. This operational change coincides with the recovery of the wavelet coherence loss of the cluster.

Lastly, the fourth cluster consists of two stations that are situated sequentially in the mainstem below the Glen Canyon Dam (Figure 2.5a). Their overall average wavelet coherence loss is 54%, and a systematic loss in the wavelet coherence is observed (Mann-Kendall tau = 0.68, 0.71) with a quasi-cyclical variability (Figure 2.5e). The beginning of this trend coincides with the completion of the Glen Canyon dam in 1963. The wavelet power spectrum of the naturalized flow at these stations signifies that the annual frequency signal is statistically significant across the given time. In contrast, the annual frequency signal in the controlled flow at these stations is mostly diminished (Figure 2.7). This result is consistent with past

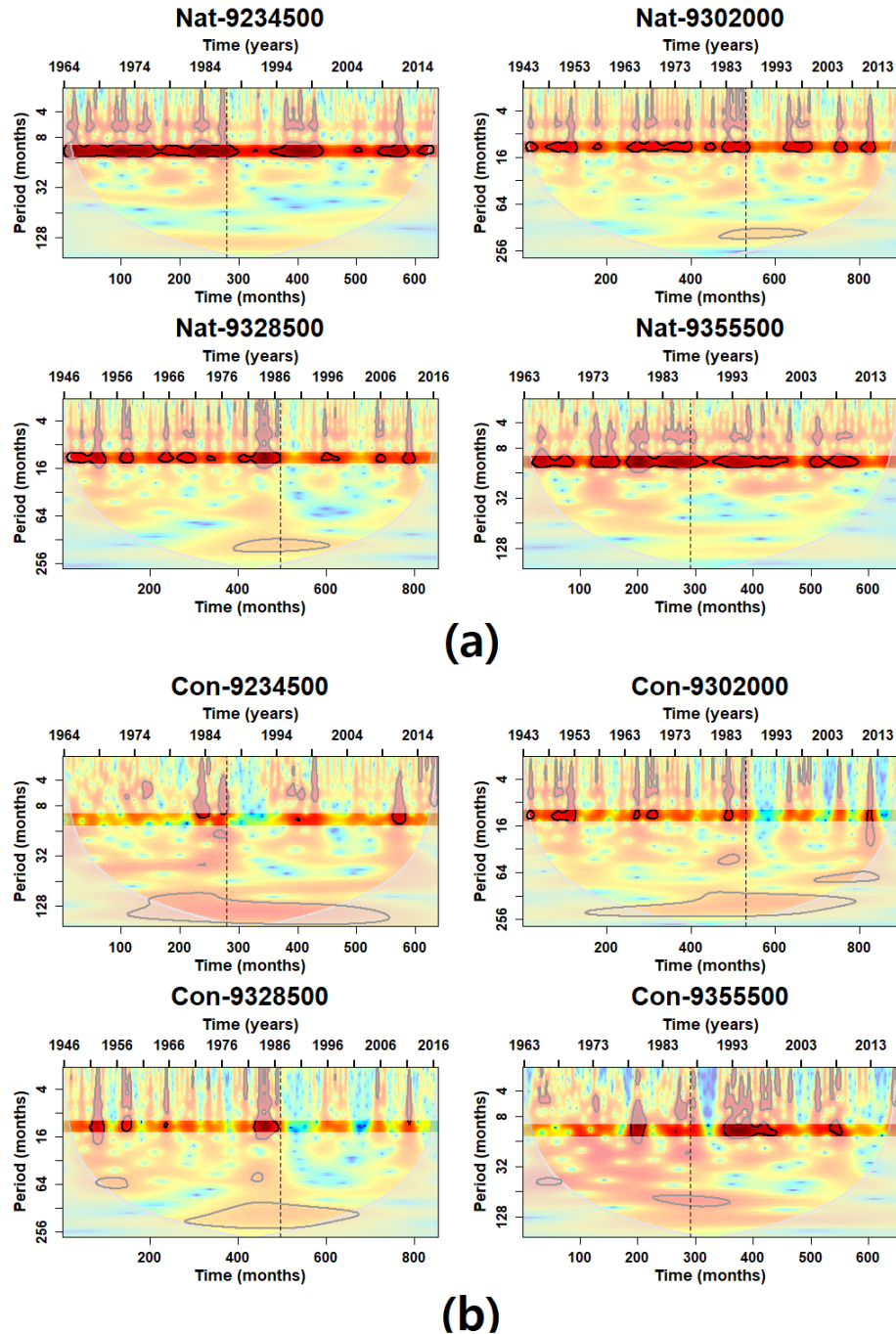


**Figure 2.6:** Wavelet power spectrum of the naturalized streamflow (a) and the controlled streamflow (b) at stations of Cluster-3 from the annual frequency analysis. Black contours in the spectra represent the 95% confidence level compared to red noise. The solid white line is the cone of influence, where zero padding has affected the variance. Red colors indicate higher local powers, whereas lower local powers are displayed in blue colors. The vertical dashed line indicates the year of 1987.

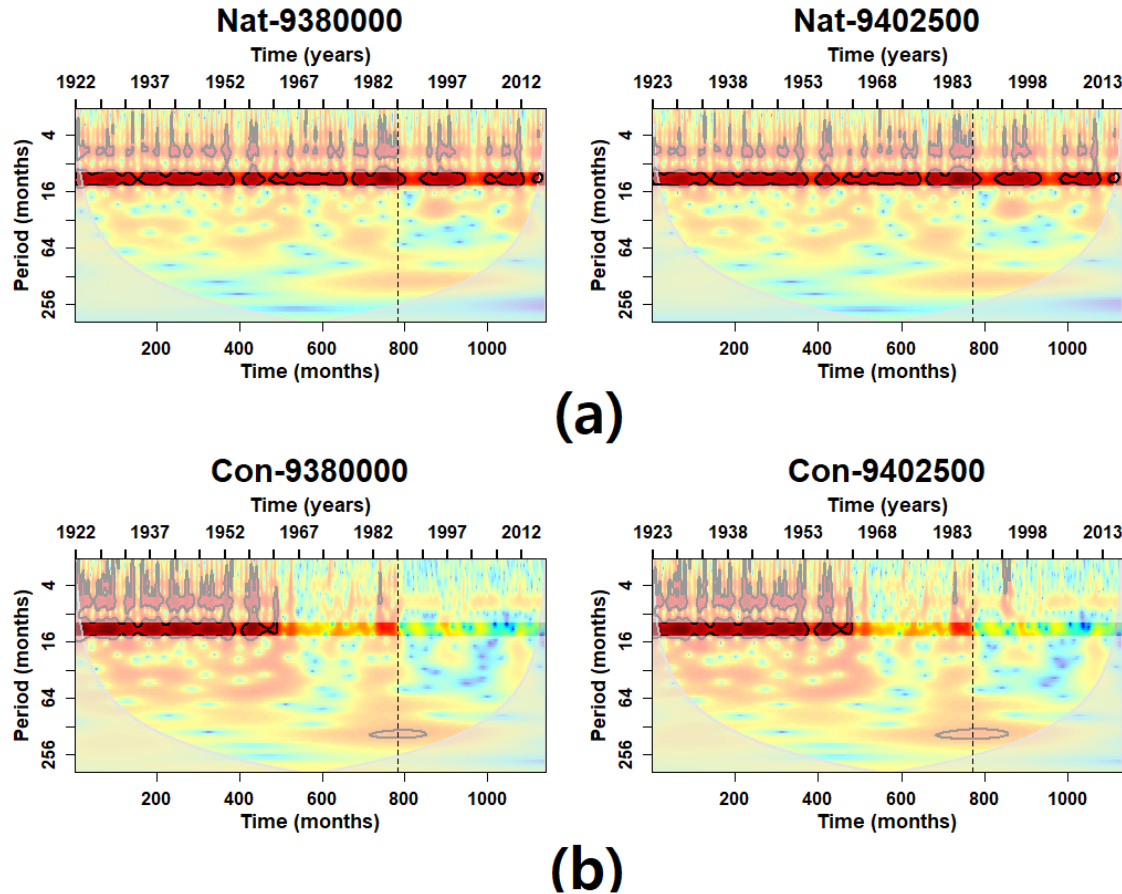


**Figure 2.7:** Wavelet power spectrum of the naturalized streamflow (a) and the controlled streamflow (b) at stations of Cluster-4 from the annual frequency analysis.

literature that revealed the diminution of the annual signal in the post-dam streamflow by using the Fourier analysis (White, Schmidt, and Topping, 2005). Therefore, the systematic increase in the wavelet coherence loss observed in Cluster-4 is assumed to be due to anthropogenic factors than to changes in the climate. At this point, it would be premature to conclude the Glen Canyon Dam's operation procedure is the dominant factor of the distortion. The wavelet coherence loss in the annual frequency level at these stations could have been cumulatively propagated from upstream as affected by other dams while the Glen Canyon Dam may

have operated in a way without interfering the streamflow. This aspect will be discussed in Section 2.6. Meanwhile, the probabilities of the streamflow to have the wavelet coherence loss greater than 33% (medium or high coherence loss) at these two stations are 89% and 79%, respectively, and the probabilities of the wavelet coherence loss exceeding 66% (high coherence loss) are both 30%. Regardless of the climate, the average probability of exceedance remains significant (Wet: 29%, Neutral: 35%, Dry: 22%). To be specific, the wavelet coherence loss (WCL) at the station immediately below the Glen Canyon Dam has a probability  $P(WCL>0.66) = 0.29$ , while  $P(WCL>0.66 | \text{Wet}) = 0.29$  and  $P(WCL>0.66 | \text{Dry}) = 0.22$ . At the other station,  $P(WCL>0.66) = 0.31$ , and  $P(WCL>0.66 | \text{Wet}) = 0.33$ ,  $P(WCL>0.66 | \text{Dry}) = 0.23$ . The wavelet coherence loss of the streamflow at these two stations shows a similar modality despite the confluences of tributaries between them.

### 2.5.2 Multi-Annual Frequency

Wavelet coherence loss analysis for multi-annual frequency classified the river network into four different clusters: all rivers of UCRB (except San Juan River) and tributaries in LCRB (Cluster-1), San Juan River (Cluster-2), segment of the Colorado River below Hoover Dam (Cluster-3), and immediate downstream of Glen Canyon Dam (Cluster-4). While wavelet coherence loss of multi-annual frequency remained at a relatively low level in most of the rivers in UCRB, significant losses were observed in other regions. A systematic increase in wavelet coherence loss has been observed since the completion of Navajo Dam. The immediate downstream of Glen Canyon Dam and Hoover Dam have been continuously showing a high level of alteration in the multi-frequency components, except that downstream of Glen Canyon Dam has been recently recovering its wavelet coherence

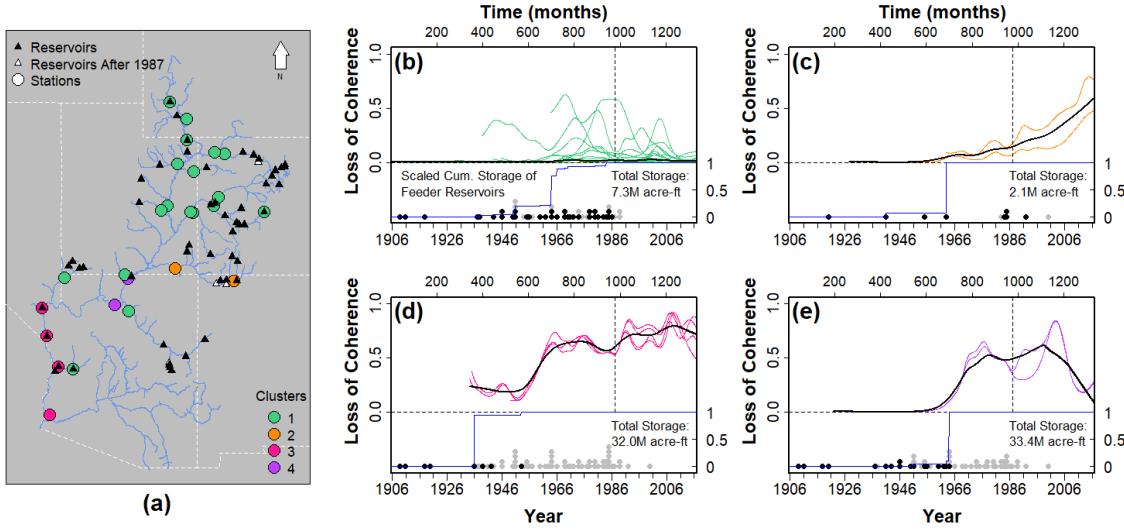


**Figure 2.8:** Cluster profiles based on the wavelet coherence loss of streamflow regarding multi-annual frequency (24–60 months). The spatial distribution of the clusters (a) and time series of the wavelet coherence loss at each cluster (b - e) is shown. Rest of the figure is similar to the description provided in Figure 2.8.

loss.

The first cluster comprises 14 stations from the UCRB and four stations in the tributaries in the LCRB (Figure 2.8a) (a total of 18 out of 26). As shown in Figure 2.8b, the estimated wavelet coherence loss of the streamflow is relatively low at these stations, with an average of 4% for the multi-annual frequency band. The wavelet coherence loss never exceeds 66% at these stations during the given period, regardless of the climate conditions (dry or wet years). A few stations show a moderate level of wavelet coherence loss ( $33\% < WCL < 66\%$ ) in a few months, but most of the wavelet coherence loss observed from Cluster-1 is determined to be less than 33% (low coherence loss) for the entire period. This cluster contains all 12 stations of Cluster-1 from the annual frequency analysis. Moreover, three stations classified as Cluster-2 from the annual frequency analysis are also included in this cluster. Cluster-1 and Cluster-2 of the annual frequency analysis include stations

where streamflow exhibits little or no wavelet coherence loss. Those 15 stations included in either of the two clusters are classified as Cluster-1 in the multi-annual frequency scale. They retain a low level of modification at both the annual and multi-annual frequency scales.

The second cluster consists of two stations at the San Juan River (Figure 2.8a). As shown in Figure 2.8c, a systematic increase in the multi-annual wavelet coherence loss is observed at these two stations (Mann-Kendall tau = 0.84, 0.81). This trend began to develop with the completion of Navajo Dam, the largest dam on the San Juan River. This systematic increase may be attributable to the drastic diminution of the multi-annual frequency in the controlled flow, which can be observed from its wavelet power spectrum (Figure 2.9). The increasing trend of the multi-annual wavelet coherence loss in the San Juan River is assumed to be mainly driven by dam operations or other anthropogenic factors. To determine whether the Navajo Dam has a significant impact on the wavelet coherence loss in the San Juan River, the dam's local regulation has to be assessed by investigating the wavelet coherence between the upstream and downstream of the dam, which will be discussed in Section 2.6 in detail. One station of this cluster is located downstream of the other and is classified as Cluster-2 from the annual frequency analysis, showing little or no wavelet coherence loss in the annual frequency range. The other station is situated immediately below the Navajo Dam and belongs to Cluster-3 of the annual frequency analysis, exhibiting a significant interannual variability in the annual wavelet coherence loss. Both the annual and multi-annual signals of the streamflow at San Juan River are disrupted in the upstream, and the annual frequency partially retrieves as the streamflow proceeds along the river. However, the disruption in the multi-annual signal from the upstream is mostly

propagated downstream.

The four stations along the Colorado River below the Hoover Dam are grouped as Cluster-3 (Figure 2.8a). The multi-annual wavelet coherence loss of the streamflow at these four stations has been high, 73% on average since 1987, with a certain level of temporal variability (Figure 2.8d). Interestingly, these four stations are categorized as Cluster-2 from the annual frequency analysis, which shows little or no wavelet coherence loss in the annual frequency range. In other words, the streamflow at these four stations has lost its wavelet coherence relative to its natural state in terms of multi-annual frequency, while the annual frequency feature is preserved during the 30 years. A shift in the wavelet coherence loss is observed at these four stations in the 1950s after the Davis Dam construction. The multi-annual frequency wavelet power spectrum of the controlled flow exhibits a deflation in both variability and scale-averaged power since the completion of the dam construction. In contrast, a consistent quasi-oscillatory signal of the multi-annual frequency component is observed in the wavelet power spectrum of the naturalized flow across the given 30-year period (Figure 2.10). These observations lead us to assume that an operational change to the local dams after the construction of the Davis Dam partially diminished the local streamflows coherence with its naturalized flow at the multi-annual scale. The Mexican Treaty of 1944 ensured the construction of Davis Dam to regulate and deliver annual flow to Mexico (Reclamation, 1946), which, in turn, contributes to the recovery in the annual frequency in streamflow downstream of Davis Dam.

Cluster-4 comprises two sequential stations in the Colorado River below the Glen Canyon Dam (Figure 2.8a). A recovery in the multi-annual wavelet coherence is observed at these stations during the 30 years. According to the extended

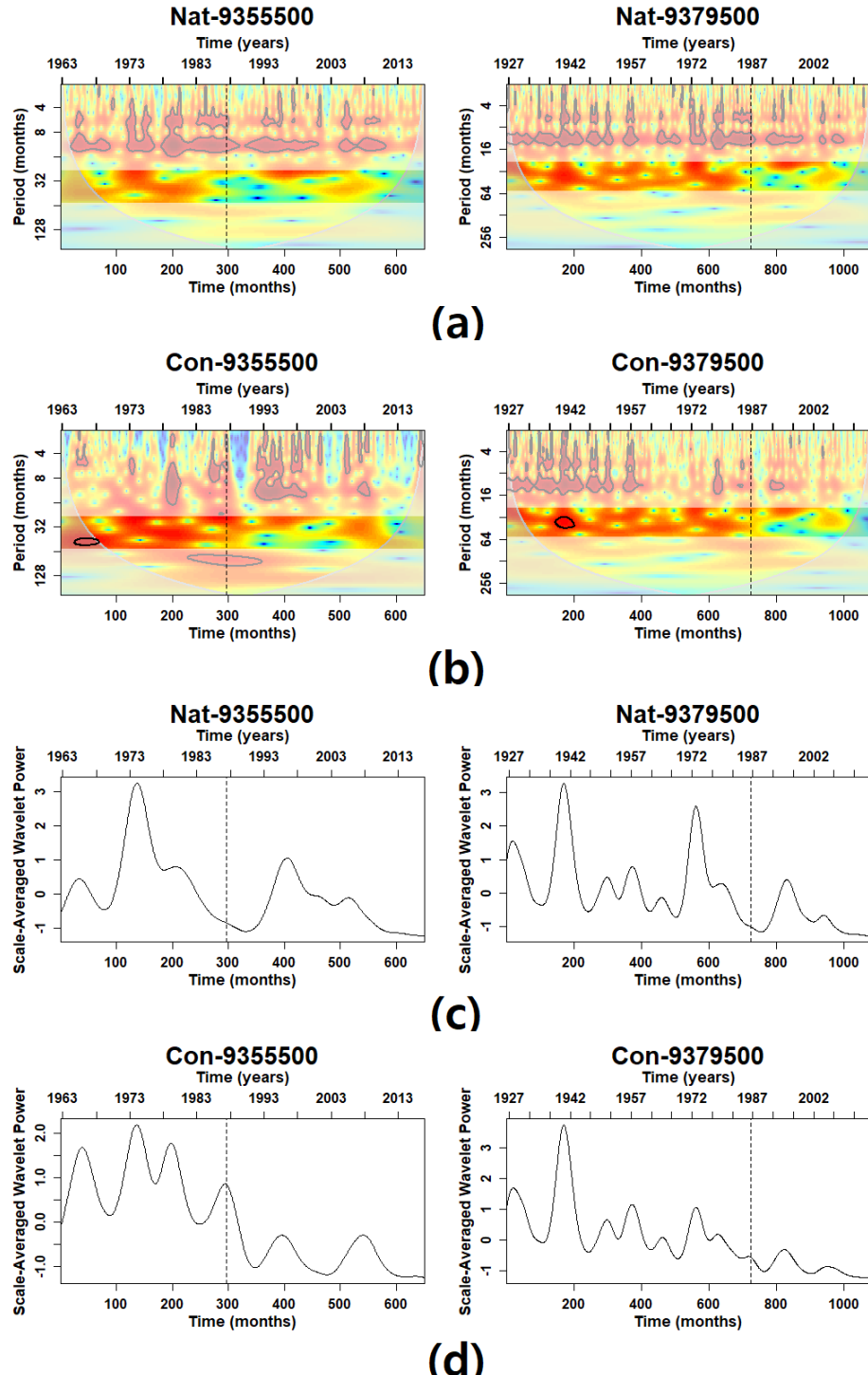


**Figure 2.9:** Wavelet power spectrum of the naturalized streamflow (a) and the controlled streamflow (b) at stations of Cluster-2 from the multi-annual frequency analysis. The scale-averaged wavelet power is also presented for both naturalized flow (c) and controlled flow (d) at these stations.

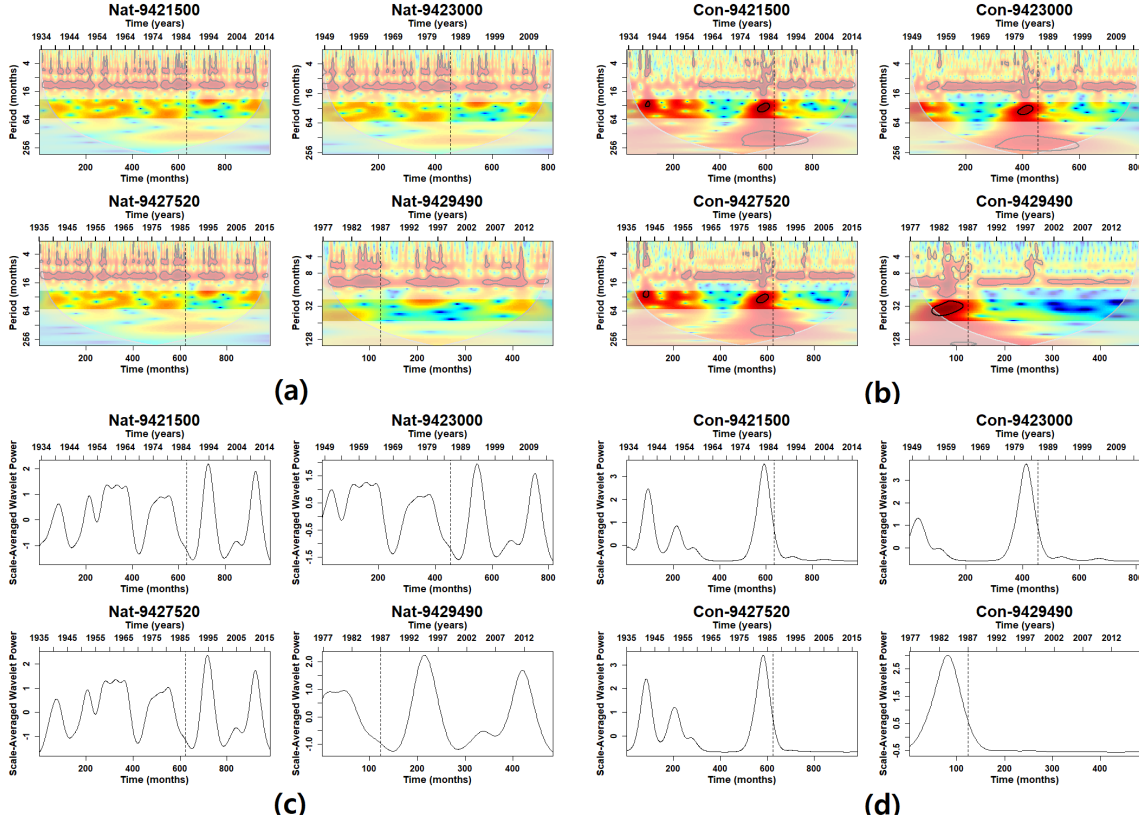


**Figure 2.10:** Wavelet power spectrum of the naturalized streamflow (a) and the controlled streamflow (b) at stations of Cluster-3 from the multi-annual frequency analysis. The scale-averaged wavelet power is also presented for both naturalized flow (c) and controlled flow (d) at these stations.

time series shown in Figure 2.8e, the wavelet coherence loss increased dramatically as the Glen Canyon Dam's construction started in 1956, and it has recently been decreasing. We assume the ascending shift in the wavelet coherence loss results from the multi-annual frequency signal's subsidence in the controlled streamflow, which can be observed from its wavelet power spectrum (Figure 2.11). The recent decrease in wavelet coherence loss reflects a recovery of the local correlation in the multi-annual frequency signal between the naturalized flow and the controlled flow. The mean probability of the wavelet coherence loss to exceed 66% (high coherence loss) at these two stations is 0.36.

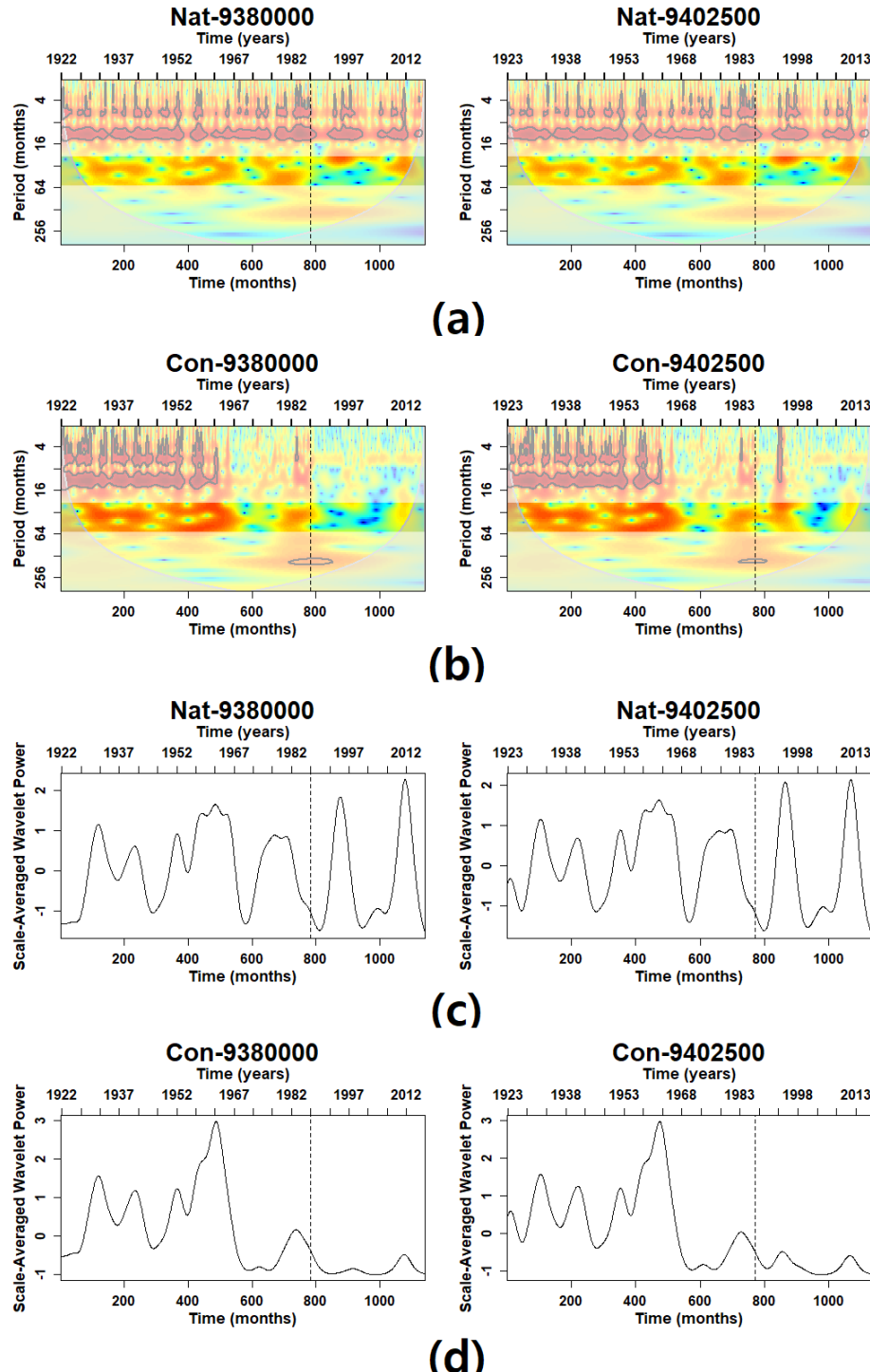


**Figure 2.11:** Wavelet power spectrum of the naturalized streamflow (a) and the controlled streamflow (b) at stations of Cluster-4 from the multi-annual frequency analysis. The scale-averaged wavelet power is also presented for both naturalized flow (c) and controlled flow (d) at these stations.

It is important to know that the temporal accuracy of a continuous wavelet transform is subjected to its frequency resolution. That is, when decomposing a time series into wavelets for lower frequency bands, longer time intervals are accounted, and thus contain less accurate temporal information. Therefore, for multi-annual frequency components, we only focused on the long-term aspects of the wavelet coherence loss rather than an analysis pursuing a temporal accuracy.

## 2.6 Discussion and Concluding Remarks

This study estimated time-varying alteration in streamflow frequency in the CRB via wavelet coherence analysis between the naturalized and controlled streamflow series. Stations where streamflow show similar patterns in wavelet coherence loss were grouped together, and four clusters were identified for each annual and multi-annual frequency band. At most of the stations in UCRB, the frequency component of the streamflow was relatively well preserved. Interestingly, the Colorado River after Hoover Dam showed a low degree of alteration in the annual frequency despite significant alteration induced by Glen Canyon Dam. In terms of multi-annual frequency, we observed significant levels of alteration after Glen Canyon Dam and Hoover Dam. However, downstream of Glen Canyon Dam we observed a tendency to recover alteration in its multi-annual frequency signal. The San Juan River has been showing a systematic increase in wavelet coherence loss for the multi-annual frequency since the completion of Navajo Dam in 1962.

Based on these results, we focused on stations where streamflow showed significant distortion in frequency and determined whether it was mainly due to anthropogenic factors or changes in the regional climate. Even if the frequency loss at any station is presumed to be driven by anthropogenic factors, it does not fully

signify that the distortion ascribes to the immediate upstream dams that feed the station. The immediate upstream dams may have been operated at a given periodicity from the immediate upstream to downstream while the actual distortion could have been derived cumulatively over the entire network. To identify the reservoirs or group of reservoirs with such significant impacts on the streamflow, we estimate each dam cluster's local regulation by computing the time-averaged wavelet coherence loss between the controlled flow series upstream and downstream for each annual and multi-annual frequency band. Local regulation is ascribed to dams that regulate flow between upstream-downstream pair(s). In addition, the time-averaged wavelet coherence loss between the naturalized and controlled streamflow series is also computed for each station and frequency band, assuming it represents the cumulative alteration in the frequency signal of the streamflow. Hence, the local regulation is the time-averaged wavelet coherence loss between the controlled flows of an upstream-downstream pair(s), and cumulative regulation is the time-averaged wavelet coherence between the natural and controlled flows at every given station.

The local regulation and cumulative discordance measured for both the annual and multi-annual frequency bands are shown in Figure 2.12 with a simplified riverine network diagram. The figure presents the time-averaged wavelet coherence loss between naturalized flow and controlled flow in circles across the basin, and they indicate the cumulative alterations in frequency. Meanwhile, the time-averaged wavelet coherence loss between the upstream and downstream controlled flow series of each dam or dam cluster within the river network is also shown in the figure in triangles. They are considered to represent the local alteration in frequency due to the corresponding dam or dam cluster. According to the

figure, the annual frequency of streamflow is less cumulatively altered at most of the stations in the UCRB. The alteration on annual frequency generally becomes more perceptible as the river proceeds, especially after the Glen Canyon Dam, but it eventually recovers as it passes the Hoover Dam. The annual frequency signal of the streamflow at station 15 (San Juan River near Archuleta, NM) in the San Juan River is moderately regulated, and the downstream group of dams shows a low level of local regulation on the annual frequency signal of the streamflow (0.09). Consequently, streamflow recovers its distorted annual frequency signal by the time it reaches station 16 (San Juan River near Bluff, UT). This recovery may be induced by the confluences of tributaries with a robust annual frequency signal. The Glen Canyon Dam shows a significant impact on the local streamflow's annual periodicity (0.58), and it propagates to station 20 (Colorado River near Grand Canyon, AZ). Hoover Dam seems to heavily regulate the annual frequency of the local streamflow (0.56), but in a way restoring the annual frequency of the streamflow to its naturalized state. This could be due to the Colorado River Compact between the Upper and Lower Colorado River Basins (Reclamation, 2021). The dams at the Colorado River after the Hoover Dam have minimal impact on the annual frequency of the streamflow. Therefore, we conclude that the streamflow's collective characteristics at these four stations observed in Cluster-2 from the annual frequency analysis are mainly due to the combination of local regulations at the Hoover Dam restoring the annual frequency of the streamflow and the operation of the subsequent dams inheriting the upstream hydrographs.

The multi-annual frequency feature of the streamflow is less altered in the UCRB, except in the San Juan River. The multi-annual frequency component of the Colorado River below the Glen Canyon Dam shows a high degree of alteration

and becomes even higher as it passes through the Hoover Dam. For the multi-annual frequency scale, a significant degree of cumulative alteration is observed in the streamflow at station 15 (San Juan River near Archuleta, NM), and it propagates down the San Juan River. This cumulative distortion of the San Juan River's multi-annual frequency is partially recovered as the streamflow reaches station 16 (San Juan River near Bluff, UT), but not enough to resemble its natural state. For both the annual and multi-annual frequency bands, the cluster of reservoirs that directly feeds station 16 (San Juan River near Bluff, UT) shows a negligible local regulation (0.17). Considering there are no major dams other than those feeding station 15 (San Juan River near Archuleta, NM) and 16 (San Juan River near Bluff, UT) in the San Juan River, the mutual behavior of streamflow at station 15 (San Juan River near Archuleta, NM) and 16 (San Juan River near Bluff, UT) for the multi-annual frequency, which is shown in Cluster-2 of the multi-annual frequency analysis, is assumed to be driven by the management of the dam cluster that feeds station 15 (San Juan River near Archuleta, NM), the Navajo Dam. Glen Canyon Dam significantly regulates the multi-annual frequency component of the local streamflow (0.41). Since there are no major dams in the river segment that significantly affects the multi-annual frequency signal of the streamflow between station 17 (Colorado River at Lees Ferry, AZ) and 20 (Colorado River near Grand Canyon, AZ), we conclude that the mutual pattern of the wavelet coherence loss of multi-annual frequency in the streamflow at these stations, which is shown in Cluster-4, are dominantly due to the local regulation of the Glen Canyon Dam. Hoover Dam also has significant control over the multi-annual frequency signal of the local streamflow (0.64), and the downstream of the dam shows a consistent pattern in the wavelet coherence loss of the multi-annual frequency until it leaves the LCRB. There are three major dams downstream of the Hoover Dam: the Davis,

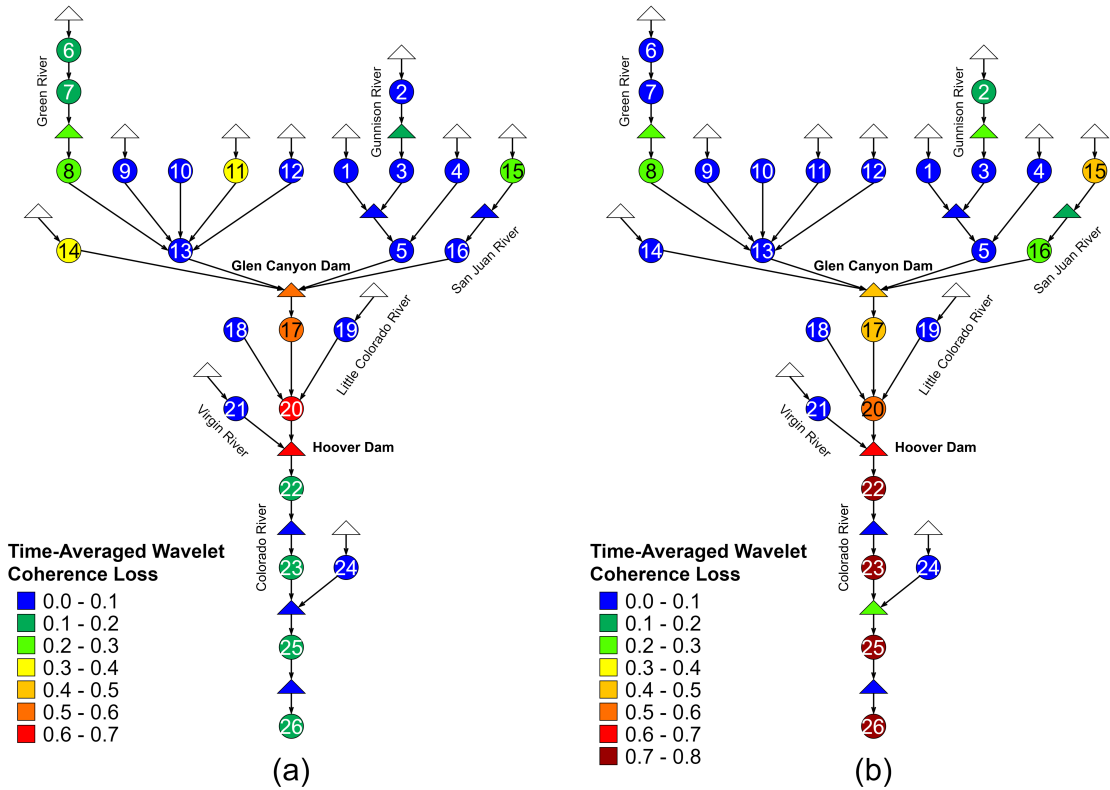


**Figure 2.12:** Simplified diagram of the riverine network with the local and cumulative alterations measured for both the annual (a) and multi-annual frequency bands (b). Dam-induced local regulations are represented with triangles, and cumulative alterations are denoted with circles.

Parker, and the Headgate Rock Dams. These dams commonly have a negligible impact on the cumulative distortion in the multi-annual frequency of the stream-flow (0.05, 0.25, 0.06). This implies that the local regulation of the Hoover Dam dominantly drives the wavelet coherence loss of Cluster-3 from the multi-annual frequency analysis.

To summarize, in this study, we assumed the wavelet coherence loss between the naturalized flow and controlled flow represents the cumulative degree of alteration of the frequencies in streamflow propagated from the headwaters. As part of the study, we also attempted to separate the local alterations in the streamflow due

to dam operations with an intent to distinguish the main sources of the cumulative alterations. As a result, it was revealed that the alteration in the frequency signal of the San Juan River is dominantly derived by the Navajo Dam. The Colorado River in the Lower Colorado Basin can be divided into two river segments regarding the wavelet coherence loss - the Glen Canyon Dam to the Hoover Dam river segment and the Hoover Dam to the basin outlet river segment. The wavelet coherence loss of the streamflow between the Hoover Dam and Glen Canyon Dam shows a homogeneous fluctuation across the segment, and the majority of this pattern is presumed to be caused by the local impact from Glen Canyon Dam. The pattern of wavelet coherence loss in the other river segment, which covers the Colorado River from the Hoover Dam to the basin outlet, shows another uniform pattern across the segment, and we conclude that this is inherited from the management of the Hoover Dam operation.

This study assesses the cumulative effects and local impacts of dams on flow frequencies to enhance our knowledge of how altered flow frequencies propagate through river networks a critical need in highly-regulated basins (Ruhi et al., 2019a). Although our approaches have largely focused on explaining the spatiotemporal changes in frequency components of streamflow, if expanded, they could help select sites for restoration and develop environmental flow operations (Palmer and Ruhi, 2019). Environmental flow operations and/or preservation of free-flowing tributaries may help restore specific dimensions of flow variability (e.g., at daily and seasonal scales), limiting the success of freshwater fish invasions (Comte, Grantham, and Ruhi, 2021).

While we used CRB as a case study, the proposed assessment method that allowed the quantification of time varying alteration in the frequency domain and

the partitioning of anthropogenic factors from climate factors, is transferable to other highly regulated basins and will help better understand dam-induced flow alteration. Thus, it can significantly contribute to the field of sustainable water management by providing information of the local and cumulative impacts of dams on streamflow alteration in the time-frequency domain. This knowledge could be utilized when planning for new dams, or reoperating existing ones. This study also emphasizes the estimation of naturalized basins for large regulated basins analysis based on past releases, storages and consumptive use. Further related studies might involve investigating the direct association between dam operations and wavelet coherence loss in the downstream for each reservoir or group of reservoirs to provide information in a form that could be useful for establishing dam operation rules.

Given we had such a naturalized dataset for a long period over CRB (Prairie and Callejo, 2005), we were able to analyze the flow alteration from multi-annual frequency influenced predominantly by water management. Federal/state/private agencies responsible for the operation of reservoirs should coordinate and make the naturalized flows over the entire cascade to support such analyses. Future research evaluating streamflow frequency alteration can be improved by taking small dams and weirs into account owing to their numbers, they often have substantial cumulative impacts (Couto and Olden, 2018). In addition, one may consider investigating streamflow alteration at finer temporal and frequency scales with awareness of the tradeoff between time and frequency resolutions. While this study focused on the frequency domain of the natural and controlled flow time series, analysis can also be done using the time domain to capture the amount of variance explained and propagated through the network. In a related study, we

developed a complete analysis on examining the highly-regulated Colorado River Basin to understand how flow alteration propagates over space, as influenced by dams and the incorporation of free-flowing tributaries (Ruhi et al., 2019b).

# References

- Berndt, D.J. and J. Clifford (1994). "Using dynamic time warping to find patterns in time series". en. In: *KDD workshop* 10.16, pp. 359370.
- Box, G.E., G.M. Jenkins, and G. Reinsel (1970). *Time series analysis: forecasting and control Holden-day San Francisco*. en. BoxTime Series Analysis: Forecasting and Control Holden Day1970.
- Brandt, S.A. (2000). "Classification of geomorphological effects downstream of dams". en. In: *Catena* 40.4, pp. 375401.
- Bruce, Breton W (2012). "WaterSMARTThe Colorado River Basin Focus Area Study". In: *US Geological Survey: Washington DC, USA*.
- Bunn, S.E. and A.H. Arthington (2002). "Basic principles and ecological consequences of altered flow regimes for aquatic biodiversity". fr. In: *Environmental management* 30.4, pp. 492507.
- Comte, L., T. Grantham, and A. Ruhi (2021). "Human stabilization of river flows is linked with fish invasions across the USA". en. In: *Global Ecology and Biogeography*.
- Council, National Research (1992). *Restoration of aquatic ecosystems: science, technology, and public policy*. en. National Academy Press.
- Couto, T.B. and J.D. Olden (2018). "Global proliferation of small hydropower plants-science and policy". en. In: *Frontiers in Ecology and the Environment* 16.2, pp. 91100.
- Farge, M. (1992). "Wavelet transforms and their applications to turbulence". en. In: *Annual review of fluid mechanics* 24.1, pp. 395458.
- Fish, U.S. and Wildlife Service (1991). *Final biological opinion for the Animas-La Plata Project, Colorado and New Mexico*. it. Denver, CO: Fish and Wildlife Service.
- Fish, U.S. and Wildlife Service (1992). *Final biological opinion on the operation of Flaming Gorge Dam*. en. Denver, CO: Fish and Wildlife Service, Mountain-Prairie Region.
- Foufoula-Georgiou, E. and P. Kumar, eds. (2014). *Wavelets in geophysics*. nl. Elsevier.
- Graf, W.L. (1999). "Dam nation: A geographic census of American dams and their largescale hydrologic impacts". en. In: *Water resources research* 35.4, pp. 13051311.
- Graf, W.L. (2006). "Downstream hydrologic and geomorphic effects of large dams on American rivers". en. In: *Geomorphology* 79.3-4, pp. 336360.

- Grill, G., C.O. Dallaire, E.F. Chouinard, N. Sindorf, and B. Lehner (2014). "Development of new indicators to evaluate river fragmentation and flow regulation at large scales: A case study for the Mekong River Basin". en. In: *Ecological Indicators* 45, pp. 148159.
- Grill, G., B. Lehner, A.E. Lumsdon, G.K. MacDonald, C. Zarfl, and C.R. Liermann (2015). "An index-based framework for assessing patterns and trends in river fragmentation and flow regulation by global dams at multiple scales". en. In: *Environmental Research Letters* 10.1, p. 015001.
- Grinsted, A., J.C. Moore, and S. Jevrejeva (2004). "Application of the cross wavelet transform and wavelet coherence to geophysical time series". en. In: *Nonlinear processes in geophysics* 11.5/6, pp. 561566.
- Hubbard, B.B. (1996). *The world according to wavelets the story of a mathematical technique in the making*. en. Universities Press.
- Keogh, E. and C.A. Ratanamahatana (2005). "Exact indexing of dynamic time warping". en. In: *Knowledge and information systems* 7.3, pp. 358386.
- Koch, F., M. Prasch, H. Bach, W. Mauser, F. Appel, and M. Weber (2011). "How will hydroelectric power generation develop under climate change scenarios? A case study in the Upper Danube basin". en. In: *Energies* 4.10, pp. 15081541.
- Kulkarni, J.R. (2000). "Wavelet analysis of the association between the southern oscillation and the Indian summer monsoon". en. In: *International Journal of Climatology: A Journal of the Royal Meteorological Society* 20.1, pp. 89104.
- Kumar, P. and E. FoufoulaGeorgiou (1997). "Wavelet analysis for geophysical applications". en. In: *Reviews of geophysics* 35.4, pp. 385412.
- Kwon, H.H., U. Lall, and A.F. Khalil (2007). "Stochastic simulation model for non-stationary time series using an autoregressive wavelet decomposition: Applications to rainfall and temperature". en. In: *Water Resources Research* 43.5.
- Kwon, H.H., U. Lall, Y.I. Moon, A.F. Khalil, and H. Ahn (2006). "Episodic inter-annual climate oscillations and their influence on seasonal rainfall in the Everglades National Park". en. In: *Water resources research* 42.11.
- Labat, D. (2005). "Recent advances in wavelet analyses: Part 1. A review of concepts". en. In: *Journal of Hydrology* 314.1-4, pp. 275288.
- Lehner, B., C.R. Liermann, C. Revenga, C. Vörösmarty, B. Fekete, P. Crouzet, and D. Wisser (2011). "Highresolution mapping of the world's reservoirs and dams for sustainable riverflow management". en. In: *Frontiers in Ecology and the Environment* 9.9, pp. 494502.
- Lytle, D.A. and N.L. Poff (2004). "Adaptation to natural flow regimes". en. In: *Trends in ecology evolution* 19.2, pp. 94100.
- Mailhot, A., G. Talbot, S. Ricard, R. Turcotte, and K. Guinard (2018). "Assessing the potential impacts of dam operation on daily flow at ungauged river reaches". en. In: *Journal of Hydrology: Regional Studies* 18, pp. 156167.

- Milly, P.C.D. and R.T. Wetherald (2002). "Macroscale water fluxes 3. Effects of land processes on variability of monthly river discharge". en. In: *Water Resources Research* 38.11, pp. 171.
- Mukhopadhyay, S., A. Sankarasubramanian, and C. Awasthi (2020). "Developing the hydrological dependency structure between streamgage and reservoir networks". en. In: *Scientific data* 7.1, pp. 19.
- Nilsson, C., C.A. Reidy, M. Dynesius, and C. Revenga (2005). "Fragmentation and flow regulation of the world's large river systems". en. In: *Science* 308.5720, pp. 405408.
- Palmer, M. and A. Ruhi (2019). "Linkages between flow regime, biota, and ecosystem processes: Implications for river restoration". en. In: *Science* 365.6459.
- Patskoski, J., A. Sankarasubramanian, and H. Wang (2015). "Reconstructed streamflow using SST and tree-ring chronologies over the southeastern United States". en. In: *Journal of Hydrology* 527, pp. 761775.
- Poff, N.L. (2018). "Beyond the natural flow regime? Broadening the hydroecological foundation to meet environmental flows challenges in a nonstationary world". en. In: *Freshwater Biology* 63.8, pp. 10111021.
- Poff, N.L., J.D. Olden, D.M. Merritt, and D.M. Pepin (2007). "Homogenization of regional river dynamics by dams and global biodiversity implications". en. In: *Proceedings of the National Academy of Sciences* 104.14, pp. 57325737.
- Prairie, J. and R. Callejo (2005). *Natural Flow and Salt Computation Methods, Calendar Years 1971-1995*. en.
- Reclamation, U.S. Bureau of (1946). *Utilization of Waters of Colorado and Tijuana Rivers and of the Rio Grande: Treaty Between the United States of America and Mexico*. it. URL: <https://www.usbr.gov/lc/region/pao/pdf/mextrety.pdf>.
- Reclamation, U.S.Bureau of (2021). *The Law of the River*.
- Ripl, W. (2003). "Water: the bloodstream of the biosphere". en. In: *Philosophical Transactions of the Royal Society of London. Series B: Biological Sciences* 358.1440, pp. 19211934.
- Ruhi, A., X. Dong, C.H. McDaniel, D.P. Batzer, and J.L. Sabo (2018). "Detimental effects of a novel flow regime on the functional trajectory of an aquatic invertebrate metacommunity". en. In: *Global change biology* 24.8, pp. 37493765.
- Ruhi, A., J. Hwang, N. Devineni, S. Mukhopadhyay, H. Kumar, L. Comte, and S. Arumugam (2019a). "How does flow alteration propagate across a large, highly-regulated basin? Dam attributes, network context, and implications for biodiversity". en. In: *AGU Fall Meeting Abstracts*. Vol. 2019, pp. 23 2086.

- Ruhi, Albert, Jeongwoo Hwang, Naresh Devineni, Sudarshana Mukhopadhyay, Hemant Kumar, Lise Comte, Scott Worland, and Sankarasubramanian Arumugam (2019b). "How does flow alteration propagate across a large, highly-regulated basin? Dam attributes, network context, and implications for biodiversity". In: *AGU Fall Meeting Abstracts*. Vol. 2019, H23N–2086.
- Sivapalan, M., K. Takeuchi, S.W. Franks, V.K. Gupta, H. Karambiri, V. Lakshmi, and E. Zehe (2003). "Shaping an exciting future for the hydrological sciences". en. In: *IAHS Decade on Predictions in Ungauged Basins* (PUB 48.6, pp. 857880.
- Snyder, F.F. (1964). "Hydrology of spillway design: Large structures-adequate data". en. In: *Journal of the Hydraulics Division* 90.3, pp. 239259.
- Thomas, H.A. (1962). "Mathematical synthesis of streamflow sequences for the analysis of river basin by simulation". en. In: *Design of water resources-systems*, pp. 459493.
- Thorndike, R.L. (1953). "Who belongs in the family?" cs. In: *Psychometrika* 18.4, pp. 267276.
- Topping, David J, David M Rubin, and LE Vierra Jr (2000). "Colorado River sediment transport: 1. Natural sediment supply limitation and the influence of Glen Canyon Dam". In: *Water Resources Research* 36.2, pp. 515–542.
- Torrence, C. and G.P. Compo (1998). "A practical guide to wavelet analysis". en. In: *Bulletin of the American Meteorological society* 79.1, pp. 6178.
- Torrence, C. and P.J. Webster (1999). "Interdecadal changes in the ENSO monsoon system". en. In: *Journal of climate* 12.8, pp. 26792690.
- Vogel, R.M., U. Lall, X. Cai, B. Rajagopalan, P.K. Weiskel, R.P. Hooper, and N.C. Matalas (2015). "Hydrology: The interdisciplinary science of water". en. In: *Water Resources Research* 51.6, pp. 44094430.
- Vörösmarty, C.J. and D. Sahagian (2000). "Anthropogenic disturbance of the terrestrial water cycle". en. In: *Bioscience* 50.9, pp. 753765.
- Vörösmarty, C.J., K.P. Sharma, B.M. Fekete, A.H. Copeland, J. Holden, J. Marble, and J.A. Lough (1997). *The storage and aging of continental runoff in large reservoir systems of the world*. en. Ambio (Sweden).
- Wang, B. and Y. Wang (1996). "Temporal structure of the Southern Oscillation as revealed by waveform and wavelet analysis". en. In: *Journal of Climate* 9.7, pp. 15861598.
- Weng, H. and K.M. Lau (1994). "Wavelets, period doubling, and timefrequency localization with application to organization of convection over the tropical western Pacific". en. In: *Journal of Atmospheric Sciences* 51.17, pp. 25232541.
- White, M.A., J.C. Schmidt, and D.J. Topping (2005). "Application of wavelet analysis for monitoring the hydrologic effects of dam operation: Glen Canyon Dam and the Colorado River at Lees Ferry, Arizona". en. In: *River research and applications* 21.5, pp. 551565.

Willis, C.M. and G.B. Griggs (2003). "Reductions in fluvial sediment discharge by coastal dams in California and implications for beach sustainability". en. In: *The Journal of Geology* 111.2, pp. 167182.

# Chapter 3

## An Improved Zhangs Dynamic Water Balance Model Using Budyko-Based Snow Representation for Better Streamflow Predictions<sup>1</sup>

### 3.1 Summary

Understanding the water balance of a catchment in relation to its regional climate forcings and catchment characteristics is critical for predicting current and future water resources amid the changing climate and land cover. This study intends to improve Zhangs monthly water balance model (a physics-based conceptual hydrologic model) that reflects the physical partitioning process of the hydrological cycle at the basin level based on regional climate and catchment characteristics. The existing model does not include snow process and has confronted evident limitations in snow-affected areas, which is a critical aspect since snowmelt water has been a significant source of water resources for many regions, especially in the temperate and frigid zones. To this end, we introduce a snow module based on

---

<sup>1</sup>Hwang, J., Devineni, N., 2021, An Improved Zhangs Dynamic Water Balance Model Using Budyko-Based Snow Representation for Better Streamflow Predictions, *Water Resources Research*, under review.

surface energy balance and Budyko-limits on melting and combine it with the existing water balance equations. Moreover, monthly parameterization is applied to the model to better explain the time-varying hydrological characteristics of a catchment. The proposed model involves five different monthly parameters, which determine the physical partitioning process of the hydrological cycle, and they are regionally calibrated under Budyko-type constraints. The model is applied to 1,210 basins across the conterminous United States, and the simulated streamflow is compared to the observed data. The proposed model significantly outperformed the current model, improving the mean NSE by 21% and increasing the number of catchments with an acceptable NSE by 36%. The spatial variability of the basin characteristics across the continental United States is also investigated based on the calibrated parameter values.

## 3.2 Introduction

Sufficient understanding of the hydrological processes and catchment controls is essential for predicting water availability and enhancing water resources reliability for human society and ecology. In this regard, several critical studies have shown that the intricate interactions between climatic forcings (precipitation and temperature/potential evapotranspiration) and catchment characteristics are the dominant controls for the water balance of a catchment (Eagleson, 1978; Milly, 1994; Farmer, Sivapalan, and Jothityangkoon, 2003; Zhou et al., 2015). Accordingly, hydroclimatic models are often adopted to simplify the complex hydroclimatological process by selectively amplifying a system's fundamental aspects at the expense of incidental details. Thus, a model is considered ideal when it is simple enough to understand and use while complex enough to reflect the hydrological

process (Anderson and Burt, 1985). To this end, numerous hydrological models have been developed along with the advances in hydrology, data collection, and computational capability (Thornthwaite, 1948; Thomas, 1981; Liang et al., 1994; Beven et al., 1995; Reggiani, Sivapalan, and Hassanizadeh, 2000; Zhang et al., 2008; Fekete et al., 2010).

An empirical study conducted by Budyko (1961) estimates the long-term water balance by introducing a simple supply-demand relationship between the long-term available surface energy and water. Also known as Budyko's framework, this concept has been used to build water balance models. The significance of such water balance models lies in the fact that they generally explain the fundamental aspects of a hydrological process sufficiently with a relatively small number of inputs and model parameters (Milly, 1994; Koster and Suarez, 1999; Sankarasubramanian and Vogel, 2002a). As the water demand continues to increase, there has been a growing interest in predicting water availability for ungauged watersheds (Sivapalan et al., 2003; Franks et al., 2005). However, quantifying the impacts of climate variability and land-use/land-cover changes on hydrology and predicting streamflow in these ungauged catchments have remained challenging (Sivapalan et al., 2003; Zhang et al., 2004). Subsequently, Budyko-based models have been gaining attention since they have the potential for monthly runoff predictions or impact assessment of land-use/land-cover changes in ungauged catchments by taking advantage of its parameter parsimony (Zhang et al., 2008; Sankarasubramanian et al., 2020).

Budyko-based water balance models at longer timescales (annual to decadal) have shown a good performance (Yang et al., 2007; Li et al., 2013; Padrón et al.,

2017) and have been further improved by introducing additional controls, including soil-moisture holding capacity, rainfall seasonality, vegetation characteristics, snow ratio, and human-influences (Zhang, Dawes, and Walker, 2001; Sankarasubramanian and Vogel, 2002a; Zhang et al., 2015; Sankarasubramanian et al., 2020). Extending these Budyko-based water balance models to finer timescales requires the incorporation of additional processes. Zhang et al. (2008) argued that rainfall variation, potential evapotranspiration, and water storage must be considered when modeling water balance at sub-annual timescales. In response, they proposed a sub-annual water balance model with a multi-layer structure to comprise the storage control and mimic the physical partitioning process. Based on a top-down approach (Sivapalan and Young, 2006), the proposed model extends the "supply-demand" concept of Budyko's framework for two critical partitioning processes separation of precipitation into catchment retention and direct runoff, and separation of water availability into evapotranspiration, soil moisture storage, and groundwater recharge. The partitioning process of the model is controlled by four efficiency and partitioning parameters in total, and each of these parameters represents a hydrological characteristic of a catchment. This parsimonious physics-based structure of Zhang's dynamic water balance model (ZDWBM) provides an advantage over other hydrologic models that simulate monthly water balance (Vandewiele, Xu, et al., 1992; Xiong and Guo, 1999; Mouelhi et al., 2006; Wang et al., 2014). The abcd model, proposed by Thomas (1981), involves a partitioning process comparable to that of the ZDWBM, but the evapotranspiration and baseflow are treated differently. Moreover, the ZDWBM allows both linear and nonlinear relationships (as the process demands) during the partitioning, whereas the abcd model only allows nonlinear relationships.

Although several studies have confirmed ZDWBM's capability in predicting monthly runoff for various regions (Zhang et al., 2008; Tekleab et al., 2011; Bai et al., 2015), the model is found to perform poorly in many watersheds across the continental United States (Petersen, Devineni, and Sankarasubramanian, 2018). It is especially true where snowmelt plays a significant role – high elevation catchments and those located in higher latitudes. Such underperformance in those regions reflects the limitation of the model without snowmelt controls. This limitation could be a critical aspect since snowmelt is often considered a significant water source for many catchments (Stewart, Cayan, and Dettinger, 2005; Barnett, Adam, and Lettenmaier, 2005). Therefore, improvements to the ZDWBM are required to account for snowmelt effects in the hydrological cycle.

Several studies included snow components in Budyko-based models, but they are mostly based on a simple temperature-based model (Martinez and Gupta, 2010; Deng et al., 2018), degree-day method (Bai et al., 2018), or physical models (Zhang et al., 2015). These methods require multiple additional parameters, may be insufficient to represent the actual snow melting, or excessively increase the model's complexity. Here, we first explore the limitations of ZDWBM in modeling monthly water balance based on more than 1,200 unmodified basins across the continental United States and propose a novel snow module for improving the model, extending the supply-demand concept of Budyko's framework based on the surface energy balance. The proposed snow module introduces only one additional parameter, minimizing the increase in model complexity. The augmented model with snow module is also tested with monthly parameters to represent the seasonal variability of catchment characteristics better.

In Section 3.3, we first describe the catchments, streamflow data, and climate

forcings data employed for the study. In Section 3.4, we review how ZDWBM describes the hydrological process using Budyko's framework. The proposed Budyko-based snow module is also discussed in Section 3.4, and the application of monthly parameterization to the snow-augmented model is demonstrated here as well. In Section 3.5, we compare the performance of the original ZDWBM, snow augmented model, and snow augmented model with monthly parameterization, respectively. Finally, in Section 3.6, we summarize our findings from the study and discuss their significance.

### 3.3 Data Description

For this study, we only focus on unmodified basins and thus employ a hydroclimatological dataset of lumped-average monthly precipitation, temperature, and potential evapotranspiration developed by Vogel and Sankarasubramanian (2005). The dataset was developed for catchments where monthly streamflow measurements are also available from the Hydroclimatic Data Network (HCDN) database, developed by Slack, Lumb, and Landwehr (1993). HCDN catchments are found to be minimally affected by human influences, which makes them specifically suitable for exploring surface-water conditions under fluctuations in prevailing climatic conditions Slack, Lumb, and Landwehr (1993). A detailed description of the HCDN dataset can be found in Vogel, Wilson, and Daly (1999), Vogel and Sankarasubramanian (2000), and Sankarasubramanian and Vogel (2002b). Figure 3.1 shows the spatial distribution of the HCDN basins in the continental United States. The basins are classified into three groups: snow-dominated basins, snow-affected basins, and basins least affected by snow. The classification is based on a snow-factor index ( $R$ ) which measures the proportion of snow to streamflow in

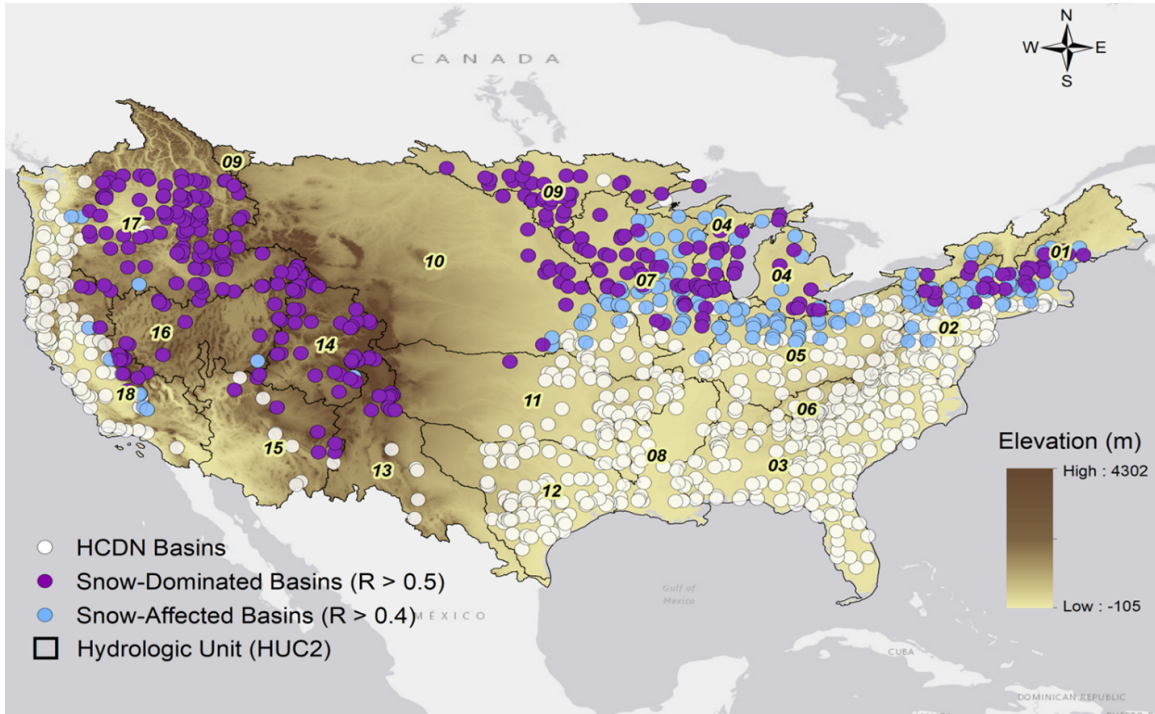


**Figure 3.1:** Spatial distribution of the selected HCDN basins across the continental United States.

a catchment (Barnett, Adam, and Lettenmaier, 2005). Catchments with  $R > 0.4$  are classified as snow-affected, and those with  $R > 0.5$  are categorized as snow-dominated. Based on this measure, more than 40% of the selected HCDN basins are snow-affected, and more than 20% are snow-dominated. The snow factor is computed based on the precipitation data, following the procedure presented in Section 3.4.2.

### 3.3.1 Streamflow Data

The HCDN database contains daily mean streamflow for 1,659 HCDN basins across the United States. It is subjected to a certain level of quality assurance by the United States Geological Survey (USGS): (1) Availability of data in electronic form data is available in electronic format; (2) Breadth of coverage records from

any station for any water year through 1988 are considered; (3) Length of record record lengths are at least 20 years unless the site location is underrepresented; (4) Accuracy of the records accuracy ratings of records are at least good as defined by USGS standards; (5) Unimpaired basin conditions there is no overt adjustment of natural monthly streamflows by any form of regulations; (6) Measured discharge values only measured discharge values are tabulated, whereas reconstructed or estimated records are not used. Streamflow records vary by catchment, ranging from 1874 to 1988, with an average record length of ~44 years. For this study, we only considered basins with continuous streamflow data for at least ten years between 1957 and 1988, and this criterion yielded 1,210 HCDN basins for further investigation. The average record length of the selected sites is approximately 31 years.

### 3.3.2 Climate Forcings Data

Vogel and Sankarasubramanian (2005) compiled a monthly climate dataset containing lumped average monthly minimum and maximum temperature, precipitation, and potential evapotranspiration for 1,376 HCDN watersheds. The temperature and precipitation data were derived by using the Precipitation Elevation Regression on Independent Slopes Model (PRISM) climate analysis system (Daly, Neilson, and Phillips, 1994). PRISM distributes point measurements to evenly spaced grids while accounting for orographic effects and other elevation-related effects. It should be noted that the HCDN precipitation data includes both rainfall and snow water equivalent without any distinction. Monthly potential evapotranspiration data were computed using the Hargreaves and Samani (1982) method.

## 3.4 Methods

### 3.4.1 Zhangs Dynamic Water Balance Model (ZDWBM)

Budyko (1961) has inferred a functional relationship between atmospheric demand, water supply, and water balance for longer time scales, assuming the water storage component is negligible under a steady state. This idea can be applied to unmodified catchments by considering precipitation ( $P$ ) as the water available, and potential evapotranspiration ( $PET$ ) as the atmospheric demand. Under dry conditions, where  $PET$  is significantly greater than  $P$ , the actual evapotranspiration ( $ET$ ) is limited by  $P$ . During wet periods, meanwhile,  $PET$  is extremely less than  $P$ . Thus,  $ET$  would be limited by  $PET$ . This supply-demand limit concept of Budykos framework can be expressed as

$$ET = f(P, PET)$$

When  $\frac{PET}{P} > 1$  (Dry Conditions),  $ET \rightarrow P$  as  $\frac{PET}{P} \rightarrow \infty$

When  $\frac{PET}{P} < 1$  (Wet Conditions),  $ET \rightarrow PET$  as  $\frac{PET}{P} \rightarrow 0$

Budykos framework is recognized as a Darwinian approach because of this empirical nature of understanding the overall hydrological process from observations and a constitutive equation (Harman and Troch, 2014; Wang et al., 2016). Due to its simplicity, several studies have attempted to develop a water balance model based on this framework (Zhang et al., 2008; Chen, Alimohammadi, and Wang, 2013; Wang and Tang, 2014) and tested various mathematical equations (Schreiber,

1904; Budyko, Miller, and Miller, 1974; Pike, 1964; Fu, 1981; Zhang, Dawes, and Walker, 2001) that comply with this concept. Fu (1981) has proposed an equation ( $F$ ) through mathematical reasoning to describe this functional relationship between mean annual  $P$ ,  $ET$ , and  $PET$  as

$$\frac{\overline{ET}}{\overline{P}} = F\left(\frac{\overline{PET}}{\overline{P}}, \alpha\right) = 1 + \frac{\overline{PET}}{\overline{P}} - \left[1 + \left(\frac{\overline{PET}}{\overline{P}}\right)^{\frac{1}{1-\alpha}}\right]^{1-\alpha} \quad (3.1)$$

where  $\overline{P}$ ,  $\overline{PET}$ , and  $\overline{ET}$  are mean annual precipitation, potential evapotranspiration, and evapotranspiration, respectively, while  $\alpha$  is the model parameter that ranges from 0 to 1. Arguing that Fus equation outperforms other similar equations in estimating mean annual evapotranspiration (Zhang et al., 2004), Zhang et al. (2008) have incorporated this equation into Budykos framework to develop a water balance model that could reflect the physical partitioning process. This combination of Darwinian approach and physical partitioning process enables Zhangs dynamic water balance model (ZDWBM) to achieve parameter parsimony, making the model suitable for ungauged catchments.

As the water balance of a catchment becomes highly sensitive to changes in storage at finer timescales, ZDWBM takes storage controls into account to make itself suitable for sub-annual time scales. The storage controls consist of two different water volumes soil-moisture storage and groundwater storage. The soil-moisture storage is the water in the vadose zone sensitive to the atmospheric demand and likely to evaporate or transpire. In contrast, groundwater storage is mainly controlled by the soil-moisture dynamics rather than climate forcings ( $P$  and  $PET$ ). Besides, ZDWBM generalizes the method of Budyko (1961) estimating  $ET$  with a supply-demand framework to model other water balance components, which will

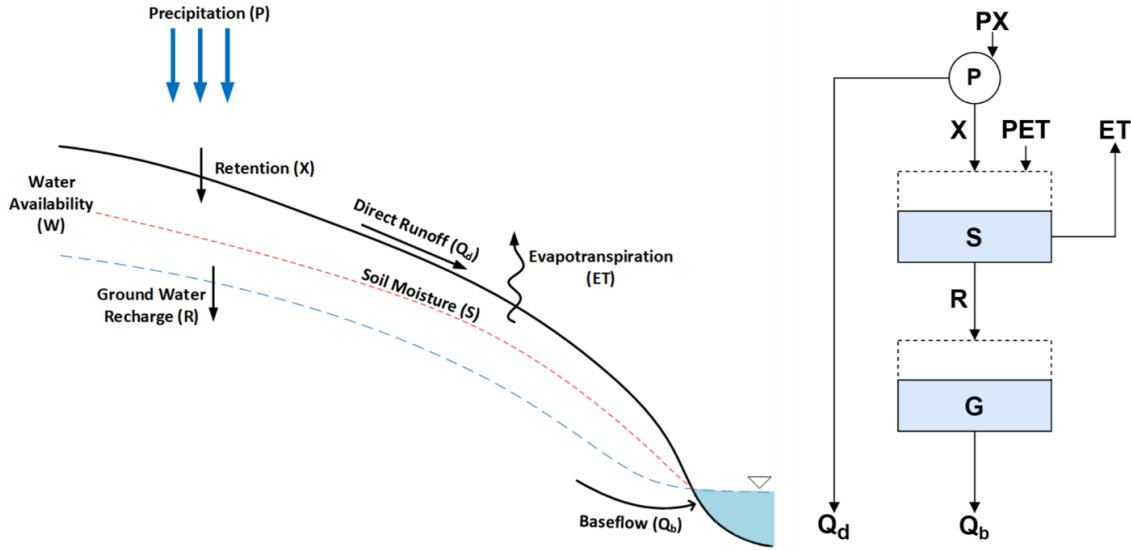


**Figure 3.2:** Diagram of the hydrological partitioning process of the ZDWBM (left) and the corresponding flowchart (right).

be shown during this section. A diagram that illustrates the partitioning process and major hydrological components of ZDWBM is presented in Figure 3.2 with a simplified flowchart alongside. ZDWBM mathematically describes the hydrological cycle by starting from partitioning precipitation ( $P_t$ ) into direct runoff ( $Q_t^d$ ) and catchment retention ( $X_t$ ) for any given timestep  $t$  as

$$P_t = Q_t^d + X_t \quad (3.2)$$

where  $X_t$  is defined as catchment rainfall retention, which is the amount of rainfall retained by the catchment for evapotranspiration ( $ET_t$ ), change in soil-moisture storage ( $S_t - S_{t-1}$ ), and groundwater recharge ( $R_t$ ). This  $X_t$  can be modeled with the supply-demand limit concept by presuming its atmospheric demand limit ( $PX_t$ ) as the sum of potential evapotranspiration ( $PET_t$ ) and available storage capacity of soil water ( $S_{max} - S_{t-1}$ ), where  $S_{max}$  is a model parameter that indicates the

maximum soil-moisture storage capacity. The water availability limit of  $X_t$  is approximated as  $P_t$ . Based on Budykos framework, therefore, Zhang et al. (2008) postulates the relationship between  $X_t$ ,  $PX_t$ , and  $P_t$  as

$$\text{When } \frac{PX_t}{P} > 1 \text{ (Dry Conditions), } X_t \rightarrow P \text{ as } \frac{PX_t}{P} \rightarrow \infty$$

$$\text{When } \frac{PX_t}{P} < 1 \text{ (Wet Conditions), } X_t \rightarrow PX_t \text{ as } \frac{PX_t}{P} \rightarrow 0$$

and employs Fus equation to estimate the actual catchment rainfall retention  $X_t$ ,

$$\frac{X_t}{P_t} = F \left( \frac{PX_t}{P_t}, \alpha_1 \right) \quad (3.3)$$

$$X_t = P_t \left[ 1 + \frac{PX_t}{P_t} - \left\{ 1 + \left( \frac{PX_t}{P_t} \right)^{\frac{1}{1-\alpha_1}} \right\}^{1-\alpha_1} \right] \quad (3.4)$$

$$X_t = P_t \left[ 1 + \frac{PET_t + (S_{max} - S_{t-1})}{P_t} - \left\{ 1 + \left( \frac{PET_t + (S_{max} - S_{t-1})}{P_t} \right)^{\frac{1}{1-\alpha_1}} \right\}^{1-\alpha_1} \right] \quad (3.5)$$

where  $\alpha_1$  is defined as retention efficiency that ranges from 0 to 1. The larger  $\alpha_1$  is, the more retention and less direct runoff are expected.

Then, water availability of a catchment ( $W_t$ ) can be estimated following its definition, the combination of  $X_t$  and  $S_{t-1}$ :

$$W_t = X_t + S_{t-1} \quad (3.6)$$

Considering the aforementioned definition of  $X_t$ , Eq. 3.6 could be rewritten as

$$W_t = ET_t + S_t + R_t \quad (3.7)$$

The sum of  $ET_t$  and  $S_t$  is referred to as evapotranspiration opportunity ( $Y_t$ ), the potential amount of water that can evaporate or transpire from the vadose zone (Sankarasubramanian and Vogel, 2002a). The atmospheric demand limit of  $Y_t$  is approximated as the sum of  $S_{max}$  and  $PET_t$ , while the water supply limit is the available water  $W_t$ . Based on the supply-demand limit concept, Zhang et al. (2008) formulated the evapotranspiration opportunity of a catchment  $Y_t$  with Fus equation as

$$\frac{Y_t}{W_t} = F \left( \frac{S_{max} + PET_t}{W_t}, \alpha_2 \right) \quad (3.8)$$

$$Y_t = W_t \left[ 1 + \frac{S_{max} + PET_t}{W_t} - \left\{ 1 + \left( \frac{S_{max} + PET_t}{W_t} \right)^{\frac{1}{1-\alpha_2}} \right\}^{1-\alpha_2} \right] \quad (3.9)$$

where  $\alpha_2$  is a model parameter defined as the evapotranspiration efficiency that ranges from 0 to 1.

Meanwhile, the evapotranspiration component  $ET_t$  is assumed to have an atmospheric limit of potential evapotranspiration ( $PET_t$ ), and a water supply limit

of catchment water availability ( $W_t$ ). Rooted in Budykos framework and Fus equation, therefore,  $ET_t$  is obtained by

$$\frac{ET_t}{W_t} = F \left( \frac{PET_t}{W_t}, \alpha_2 \right) \quad (3.10)$$

$$ET_t = W_t \left[ 1 + \frac{PET_t}{W_t} - \left\{ 1 + \left( \frac{PET_t}{W_t} \right)^{\frac{1}{1-\alpha_2}} \right\}^{1-\alpha_2} \right] \quad (3.11)$$

where  $\alpha_2$  is the same model parameter from Eq. 3.8. By obtaining  $Y_t$  and  $ET_t$ , groundwater recharge  $R_t$  can now be estimated by rewriting Eq. 3.7 as

$$R_t = W_t - Y_t \quad (3.12)$$

It should be noted that the parameter sharing between Eq. 3.8 and Eq. 3.10 ensures that groundwater recharge  $R_t$  is essentially governed by evapotranspiration efficiency  $\alpha_2$ . That is, larger (smaller) values of  $\alpha_2$  results in less (more) groundwater recharge  $R_t$  in the catchment.

Considering the definition of  $Y_t$ , soil-moisture storage ( $S_t$ ) can be now determined as:

$$S_t = Y_t - ET_t \quad (3.13)$$

ZDWBM assumes groundwater storage ( $G_t$ ) as a linear reservoir, and thus, groundwater balance is estimated as

$$G_t = (1 - d) G_{t-1} + R_t \quad (3.14)$$

$$Q_t^b = d(G_{t-1}) \quad (3.15)$$

where  $Q_t^b$  is baseflow, and  $d$  is a model parameter which represents the proportion of groundwater transferred to the baseflow for each given timestep  $t$ . Finally, the total streamflow ( $Q_t$ ) can be obtained by the summation of direct runoff  $Q_t^d$  and the base flow  $Q_t^b$  as written as follows:

$$Q_t = Q_t^d + Q_t^b \quad (3.16)$$

To summarize, ZDWBM estimates catchment scale sub-annual runoff with climate forcings such as  $P_t$  and  $PET_t$  based on four different model parameters retention efficiency ( $\alpha_1$ ), evapotranspiration efficiency ( $\alpha_2$ ), groundwater coefficient ( $d$ ), and maximum soil-moisture storage capacity ( $S_{max}$ ). These parameters are calibrated based on four objective functions which determine the dissimilarity between estimated and observed runoff data for each tested catchment. Each of these objective function places different weights on errors in low flows, high flows, time shift between estimated and observed, and mass balance over the period of calibration. A set of parameter values that minimizes the mean of those four objective functions are assumed to represent the regional characteristics of the climate and basin.

### 3.4.2 Implantation of a Budyko-based Snow Module to ZDWBM

The idea of Budykos framework stems from the concept of long-term energy and water balance, which both are subjected to the principle of conservation, assuming the ground heat and subsurface water storage components are negligible. The long-term energy and water balance of a catchment for can be mathematically

expressed, respectively, as

$$Rn = L_E \cdot ET + Hn \quad (3.17)$$

$$P = ET + Q \quad (3.18)$$

where  $Rn$  [ $M/T^2$ ] is the net radiative heat flux from the atmosphere to land surface,  $L_E$  [ $M/L \cdot T^2$ ] is the latent heat of evaporation,  $ET$  [ $L$ ] is evapotranspiration,  $Hn$  [ $M/T^2$ ] is the sensible heat, the heat transfer from land surface to atmosphere,  $P$  [ $L$ ] is precipitation, and  $Q$  [ $L$ ] is runoff. The division of Eq. 3.17 by the latent heat of evapotranspiration ( $L_E$ ) yields an energy-balance constraint on evapotranspiration ( $ET$ ):

$$\frac{Rn}{L_E} = ET + \frac{Hn}{L_E} \quad (3.19)$$

The above equation implies that the maximum possible  $ET$  occurs when the sensible heat is negligible, and the incoming radiative energy is exclusively consumed by  $ET$  while the amount of water available for  $ET$  is unlimited in the subsurface. This maximum possible evapotranspiration is thus numerically equivalent to  $Rn/L_E$  and is conceptually referred to as potential evapotranspiration ( $PET$ ) (Budyko, Miller, and Miller, 1974; Zhang et al., 2015; Sposito, 2017).

Since ET simultaneously acts as the primary process for both long-term water balance and energy balance as shown in Eq. 3.18 and 3.19, it is possible to conclude that a functional relationship between water and energy balance exists:

$$\frac{ET}{P} = f \left( \frac{PET}{P} \right) \quad (3.20)$$

which is referred to as Budykos framework as mentioned in the previous subsection.

To improve the existing dynamic water balance model proposed by Zhang et al. (2008), especially in snow-affected regions, we developed a snow module that could be implanted into the model. The proposed snow module takes the effect of snow into account and follows the logic of Budykos framework as well to preserve the spirit of, and parameter parsimony that is achieved from ZDWBM. The snow and water balance for any monthly timestep  $t$  are jointly considered as

$$SF_t + SP_{t-1} = M_t + SP_t \quad (3.21)$$

$$M_t + RF_t = ET_t + Q_t + \Delta S_t \quad (3.22)$$

where  $SF_t$  [ $L$ ] is the snow-water equivalent (SWE) snowfall,  $SP_t$  [ $L$ ] is the SWE snowpack,  $M_t$  [ $L$ ] is the SWE snowmelt,  $RF_t$  [ $L$ ] is rainfall, and  $\Delta S_t$  [ $L$ ] is the change in soil-moisture storage. Eq. 3.21 indicates that the given amount of snow is equivalent to the sum of snowmelt and the remaining snowpack, neglecting snow sublimation and deposition.

Since precipitation from the HCDN database provides the sum of rainfall and SWE snowfall without any distinction, each rainfall and snowfall amount have to be determined. Here  $P_t$  is partitioned into  $RF_t$  and  $SF_t$  based on the monthly average of daily min and max temperatures ( $T_t^{avg}$ ):

If  $T_t^{avg} \leq -0.5$ , then  $RF_t = 0$  and  $SF_t = P_t$

If  $T_t^{avg} \geq +0.5$ , then  $RF_t = P_t$  and  $SF_t = 0$

Else,  $RF_t = P_t (0.5 + T_t^{avg})$  and  $SF_t = P_t (0.5 - T_t^{avg})$

Since the process of melting consumes energy, as does evapotranspiration, the intra-annual energy balance equation can be expressed in a similar form to Eq. 3.17 as,

$$Rn_t = L_E \cdot ET_t + L_F \cdot M_t + Hn_t + G_t \quad (3.23)$$

where  $L_F [M/L \cdot T^2]$  is the latent heat of fusion, and  $G_t [M/T^2]$  is the ground heat flux. As both the processes of snow melting and evapotranspiration simultaneously absorb energy, especially during melting seasons, while the given amount of  $Rn_t$  is limited, the maximum possible energy for each phase transition is determined as a fraction of the incoming  $Rn_t$ , assuming  $Hn_t$  and  $G_t$  are fully occupied for the phase transitions. Previous energy balance studies in different locations argue that net radiation contributes most of the energy available for melting (Mazurkiewicz, Callery, and McDonnell, 2008; Boudhar et al., 2016; Fayad et al., 2017).

When a substantial amount of energy is supplied to a surface containing snow, both evaporation and melting start absorbing energy competitively (Miller, 1982). An exact division of the total energy available for the phase change processes of evaporation and melting is challenging since it involves complex heat and mass transfer processes of a system with large temporal and spatial variations. An experimental study conducted by Shook and Gray (1997) argued that more than 90% of

the total energy available for phase changes is allocated for melting than evaporation in open environments with continuous snowpacks. At a basin scale, however, snowpacks are rarely continuous in monthly timescale. Thus, it might be inappropriate to consider this estimate as the absolute fraction for partitioning the total energy for  $ET_t$  and  $M_t$ . Instead, we assume net  $Rn_t$  is partitioned for  $ET_t$  and  $M_t$  based on the mass ratio of water and snow contents in the catchment, respectively.

$$Rn_t = Re_t + Rm_t \quad (3.24)$$

$$Re_t = \left( \frac{RF_t + S_{t-1}}{SF_t + SP_{t-1} + RF_t + S_{t-1}} \right) \cdot Rn_t \quad (3.25)$$

$$Rm_t = \left( \frac{SF_t + SP_{t-1}}{SF_t + SP_{t-1} + RF_t + S_{t-1}} \right) \cdot Rn_t \quad (3.26)$$

where  $Re_t$  [ $M/T^2$ ] and  $Rm_t$  [ $M/T^2$ ] are the maximum possible energies distributed for  $ET_t$  and  $M_t$ , respectively. This setup yields an energy fraction similar to that from Shook and Gray (1997) for extreme snow-dominating situations. This calculation method can be considered conceptually reasonable for obtaining a rough estimate of the energy partition for any generalized case. For example, the proportion of total energy for  $ET_t$  is expected to increase when snowpacks become patchy and accompanied by increased air temperature (higher saturation vapor pressure) and snowmelt water. Meanwhile, when snowpack accumulates in the presence of low air temperature, the total amount of energy for evaporation may be small. However, the proportion of the total energy for  $M_t$  is likely to increase due to the low air temperature (lower saturation vapor pressure), increased snow component, and water loss by freezing. That is, the ratio of the available energy

between  $ET_t$  and  $M_t$  can be roughly estimated in proportion to the mass ratio of water and snow.

Then, the maximum possible evapotranspiration and melting are computed with the given  $PET_t$  dataset since it can derive the net total available energy for phase transitions:

$$\begin{aligned} PET_t^* &= \frac{Re_t}{L_E} = \left( \frac{RF_t + S_{t-1}}{SF_t + SP_{t-1} + RF_t + S_{t-1}} \right) \cdot \frac{Rn_t}{L_E} \\ &= \left( \frac{RF_t + S_{t-1}}{SF_t + SP_{t-1} + RF_t + S_{t-1}} \right) \cdot PET_t \quad (3.27) \end{aligned}$$

$$\begin{aligned} PM_t &= \frac{Rm_t}{L_F} = \left( \frac{SF_t + SP_{t-1}}{SF_t + SP_{t-1} + RF_t + S_{t-1}} \right) \cdot \frac{Rn_t}{L_F} \\ &= \left( \frac{SF_t + SP_{t-1}}{SF_t + SP_{t-1} + RF_t + S_{t-1}} \right) \cdot \frac{Rn_t}{(0.15 \cdot L_E)} \\ &= \left( \frac{SF_t + SP_{t-1}}{SF_t + SP_{t-1} + RF_t + S_{t-1}} \right) \cdot \left( \frac{1}{0.15} \right) \cdot PET_t \quad (3.28) \end{aligned}$$

where  $PET_t^* [L]$  is the newly computed potential evapotranspiration and  $PM_t [L]$  is potential melting, which is the maximum possible melting. Here, we compute  $PET_t^*$  with the existing  $PET_t$  which is the potential amount of evapotranspiration when the radiative energy is monopolized only by the evapotranspiration process. As the specific latent heat of fusion (334 kJ/kg) is  $\sim 0.15$  times the specific latent heat of evaporation (2265 kJ/kg),  $PM_t$  is obtained with the existing  $PET_t$  using this ratio.

Now  $M_t$  could be obtained by establishing a functional relationship based on the logic of Budykos framework, approximating the supply limit of  $M_t$  as given amount of snow ( $SF_t + SP_{t-1}$ ), and the atmospheric demand limit as  $PM_t$ . This could be mathematically expressed using Fus equation as

$$\frac{M_t}{SF_t + SP_{t-1}} = F \left( \frac{PM_t}{SF_t + SP_{t-1}}, \beta \right) \quad (3.29)$$

$$M_t = (SF_t + SP_{t-1}) \left[ 1 + \frac{PM_t}{SF_t + SP_{t-1}} - \left[ 1 + \left( \frac{PM_t}{SF_t + SP_{t-1}} \right)^{\frac{1}{1-\beta}} \right]^{1-\beta} \right] \quad (3.30)$$

where  $\beta$  is a parameter that indicates the melting efficiency of a catchment, ranging from 0 to 1. More  $M_t$  is expected to occur at basins with larger values of  $\beta$ , whereas less  $M_t$  is expected at basins with smaller values of  $\beta$ . When snow is not present ( $SF_t + SP_{t-1} = 0$ ),  $M_t$  is always 0 regardless of  $\beta$ . Therefore, the calibrated  $\beta$  for catchments with mean annual snow less than 0.1 mm are adjusted as 1 to comply with its concept.

Since the proposed snow module defines the input source of water as a combination of rainfall ( $RF_t$ ) and snowmelt ( $M_t$ ), the initial partitioning process of ZDWBM is reconstructed as:

$$RF_t + M_t = Q_t^d + X_t \quad (3.31)$$

The subsequent procedures of the model remain the same except that catchments are assumed to be frozen during snow accumulating phases. In other words, the entire initial subsurface water storage  $S_{t-1}$  becomes a part of the final snowpack  $SP_t$ , while  $S_t$  becomes 0 when the mean temperature ( $T_t^{avg}$ ) is less than -0.5 .

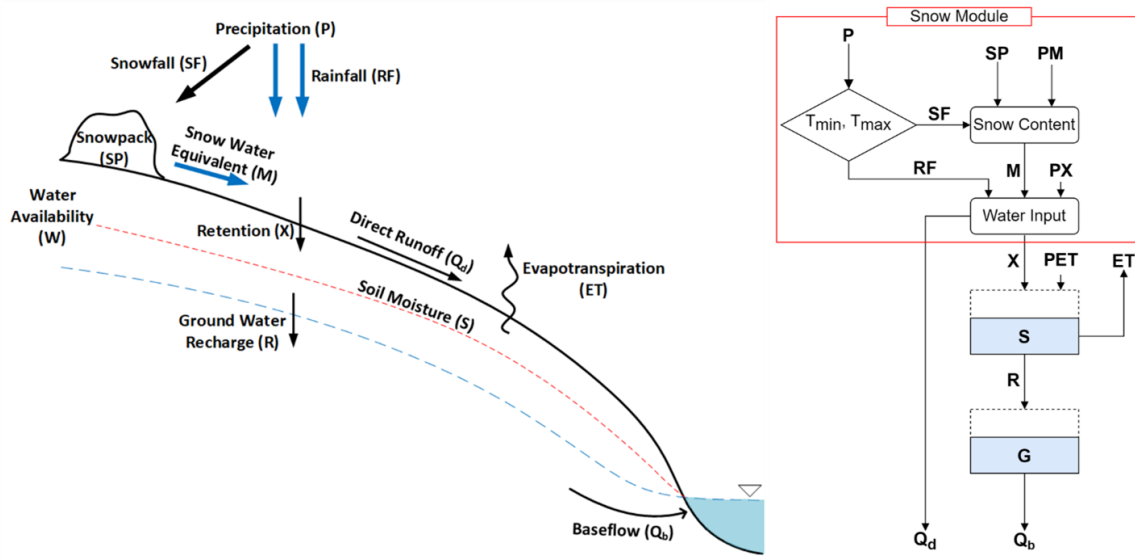


**Figure 3.3:** Diagram of the hydrological partitioning process of the snow augmented ZD-WBM (left) and the corresponding flowchart (right).

Figure 3.3 illustrates the augmented water balance model with the proposed snow module.

### 3.4.3 Monthly Parameterization

The existing ZDWBM yields four time-invariant model parameters, each representing different hydrological aspects of the catchment. However, catchment's hydrological responses are often modulated by various factors that manifest in sub-annual time scales, such as antecedent soil moisture, seasonal vegetation, and temperature fluctuations. Thus, while those single-value parameters may partially explain the long-term characteristics of catchments, they might be insufficient to reflect catchments' dynamic response. Moreover, since both snow melting and accumulation processes are extremely season-sensitive, the necessity of developing a time-variant parameterization arises as we intend to include the snow factor in the model. To capture the time-variant catchment properties while minimizing

the increase in model complexity at the same time, we set each model parameter to have 12 monthly values. The monthly parameters are optimized to minimize the dissimilarity between the simulated and observed flows during the calibration period. For each monthly timestep, the model is designed to calibrate the parameter values of the corresponding month. The full model with snow module and monthly parameterization is mathematically presented below:

$$\frac{M_t}{SF_t + SP_{t-1}} = F \left( \frac{PM_t}{SF_t + SP_{t-1}}, \beta_n \right), \text{ where } n = 1 : 12$$

$$\frac{M_t}{SF_t + SP_{t-1}} = 1 + \frac{PM_t}{SF_t + SP_{t-1}} - \left[ 1 + \left( \frac{PM_t}{SF_t + SP_{t-1}} \right)^{\frac{1}{1-\beta_n}} \right]^{1-\beta_n} \quad (3.32)$$

$$RF_t + M_t = Q_t^d + X_t \quad (3.33)$$

$$\frac{X_t}{P_t} = F \left( \frac{PX_t}{P_t}, \alpha_{1n} \right), \text{ where } n = 1 : 12 \text{ (months)}$$

$$X_t = P_t \left[ 1 + \frac{PET_t^* + (S_{maxn} - S_{t-1})}{P_t} - \left\{ 1 + \left( \frac{PET_t^* + (S_{maxn} - S_{t-1})}{P_t} \right)^{\frac{1}{1-\alpha_{1n}}} \right\}^{1-\alpha_{1n}} \right] \quad (3.34)$$

$$W_t = X_t + S_{t-1} \quad (3.35)$$

$$\frac{Y_t}{W_t} = F \left( \frac{S_{maxn} + PET_t^*}{W_t}, \alpha_{2n} \right), \text{ where } n = 1 : 12 \text{ (months)}$$

$$Y_t = W_t \left[ 1 + \frac{S_{maxn} + PET_t^*}{W_t} - \left\{ 1 + \left( \frac{S_{maxn} + PET_t^*}{W_t} \right)^{\frac{1}{1-\alpha_{2n}}} \right\}^{1-\alpha_{2n}} \right] \quad (3.36)$$

$$\frac{ET_t}{W_t} = F \left( \frac{PET_t^*}{W_t}, \alpha_{2n} \right), \text{ where } n = 1 : 12 \text{ (months)}$$

$$ET_t = W_t \left[ 1 + \frac{PET_t^*}{W_t} - \left\{ 1 + \left( \frac{PET_t^*}{W_t} \right)^{\frac{1}{1-\alpha_{2n}}} \right\}^{1-\alpha_{2n}} \right] \quad (3.37)$$

$$R_t = W_t - Y_t \quad (3.38)$$

$$S_t = Y_t - ET_t \quad (3.39)$$

$$G_t = (1 - d_n) G_{t-1} + R_t, \text{ where } n = 1 : 12 \text{ (months)}$$

$$Q_t^b = d(G_{t-1}) \quad (3.40)$$

$$Q_t = Q_t^d + Q_t^b \quad (3.41)$$

For parameter estimation, an optimization function is solved for each station

by minimizing the average of four error functions:

$$\text{Min}(Z) \text{ while } Z = \frac{\sum_{i=1}^4 Z_i}{4}$$

$$Z_1 = \frac{\sum_{t=1}^N [\ln(Q_t^{sim}) - \ln(Q_t^{obs})]^2}{\sum_{t=1}^N [\ln(Q_t^{obs}) - \ln(\bar{Q}^{obs})]^2} \quad (3.42)$$

$$Z_2 = \frac{\sum_{t=1}^N (Q_t^{sim} - Q_t^{obs})^2}{\sum_{t=1}^N (Q_t^{obs} - \bar{Q}^{obs})^2} \quad (3.43)$$

$$Z_3 = \frac{\sum_{t=1}^N (Q_t^{sim} - \bar{Q}^{sim})(Q_t^{obs} - \bar{Q}^{obs})}{\sqrt{\sum_{t=1}^N (Q_t^{sim} - \bar{Q}^{sim})^2 \sum_{t=1}^N (Q_t^{obs} - \bar{Q}^{obs})^2}} \quad (3.44)$$

$$Z_4 = \left| \ln \left( \frac{\sum_{t=1}^N Q_t^{sim}}{\sum_{t=1}^N Q_t^{obs}} \right) \right| \quad (3.45)$$

while,

$$0 \leq \beta_n \leq 1 \quad 0 \leq \alpha_{1n} \leq 1 \quad 0 \leq \alpha_{2n} \leq 1 \quad 0 \leq d_n \leq 1 \quad 0 \leq S_{maxn}$$

where  $Q_t^{sim}$  is the simulated streamflow at time  $t$ ,  $\bar{Q}^{sim}$  is the mean simulated streamflow,  $Q_t^{obs}$  is the observed streamflow at time  $t$ ,  $\bar{Q}^{obs}$  is the mean observed streamflow,  $N$  is the number of timesteps in the calibration period. A set of parameter values that minimizes the mean of those four objective functions is obtained by using the constrained nonlinear multivariate function (TheMathworksInc, 2016). For each station, the model runs one cycle of spin-up over the entire given period with the storage components (soil-moisture, snow, groundwater) at their initial

conditions for a stable initialization before calibration. The estimated storage components from the last timestep of the spin-up are employed as the initial condition for the storages during the calibration process.

## 3.5 Results and Discussion

This section presents the model's incremental improvements after employing the proposed snow module and monthly parameterization. The first subsection shows how the original ZDWBM performed across the continental United States. The second subsection illustrates how the model improves as its process representation also includes a snow factor. The third subsection presents the model improvements through improved parameterization at the monthly scale. Further validation and verification for model over-fitting are presented in the fourth subsection. Finally, the results of the monthly parameters are presented and discussed in the fifth subsection.

For the evaluation of the model, the classic Nash-Sutcliffe efficiency (NSE) coefficient (Nash and Sutcliffe, 1970) between the simulated and observed monthly streamflow were examined ( $NSE = 1 - MSE/\sigma_O^2$  where  $MSE$  is the mean squared error between the simulated and observed monthly flows and  $\sigma_O^2$  is the variance of observed monthly flows). NSE theoretically ranges between  $-\infty$  to 1. Values close to 1 imply that the model can resemble the observed system, whereas values close to 0 mean that the model performance is no better than the mean of the observed. Thus, NSE values less than zero are undesirable. Despite its inherent limitations (Schaeefli and Gupta, 2007; Gupta and Kling, 2011; Ehret and Zehe, 2011), the NSE statistic is one of the evaluation metrics most commonly used for evaluating hydrological model performances. Threshold values of NSE representing a reasonable

model performance often depend on the purpose of the model, but a hydrological model at a monthly timestep could be judged *good* when its NSE is greater than 0.65, *satisfactory* when it is greater than 0.5, and *unsatisfactory* if it is less than 0.5 (Moriasi et al., 2007). We used these threshold values for evaluating our models. The results of the stepwise improvements in model performance are summarized in Table 3.1.

### 3.5.1 Performance of the Original ZDWBM across the Continental United States

Here we apply the original ZDWBM across the continental United States (CONUS) and evaluate its performance. Figure 3.4 shows the spatial variability and cumulative distribution function (CDF) of ZDWBM's NSE values across the CONUS and how they relate to snow-runoff ratio R, elevation, and HUC2 location. Figure 3.4a shows how NSE is associated with the geographic characteristics of the CONUS. The model performance is *good* for 38% of the 1,210 HCDN catchments (Figure 3.4b). As expected, the model confronts evident limitations in areas affected by snow, including high elevation catchments located in the Rocky Mountains area (HUC2 region 13, 14, 16, and 17) and catchments in the northern U.S. (HUC2 region 1, 4, 7, and 9), likely due to its lack of a snow process representation (Figure 3.4c). The absence of snow components in the model is also understood through Figure 3.4d, which shows the association between model performance (NSE) and snow-runoff ratio R. The model performs better in basins where snow is not a dominant factor. This result is consistent with a previous study that explored the monthly hydroclimatology of the CONUS with ZDWBM (Petersen, Devineni, and Sankarasubramanian, 2018). The median NSE value of the model across all the 1,210 catchments is estimated as ~0.6, while it is ~0.3 in snow-affected regions

Total HCDN Catchments			
	Original ZDWBM	Model with Snow Module	Model with Snow Module and Monthly Parameters
Median NSE Evaluation (%)	0.57	0.66	0.78
- <i>Good</i>	38	51	83
- <i>Satisfactory</i>	19	27	10
- <i>Unsatisfactory</i>	43	21	7
Overall Bias (%)	0	5	-1
Seasonal Bias (%)			
- <i>Winter</i>	-7	4	-1
- <i>Spring</i>	25	17	3
- <i>Summer</i>	-11	1	0
- <i>Fall</i>	-38	-22	3
Snow-Affected HCDN Catchments ( $R > 0.4$ )			
	Original ZDWBM	Model with Snow Module	Model with Snow Module and Monthly Parameters
Median NSE Evaluation (%)	0.28	0.59	0.76
- <i>Good</i>	5	33	77
- <i>Satisfactory</i>	13	32	14
- <i>Unsatisfactory</i>	82	36	9
Overall Bias (%)	2	6	-1
Seasonal Bias (%)			
- <i>Winter</i>	-39	16	3
- <i>Spring</i>	35	15	-3
- <i>Summer</i>	-3	-3	-1
- <i>Fall</i>	48	-22	1

**Table 3.1:** Summary of the incremental improvements of the model for all and snow-affected HCDN catchments across the CONUS.

$(R > 0.4)$ .

The combined results from Figure 3.4 indicate that the original ZDWBM is noticeably inadequate for the CONUS. According to a previous study, the model verified well against observed monthly streamflow data when tested for catchments in Australia, showing NSE values ranging between 0.6 and 0.9 for the majority

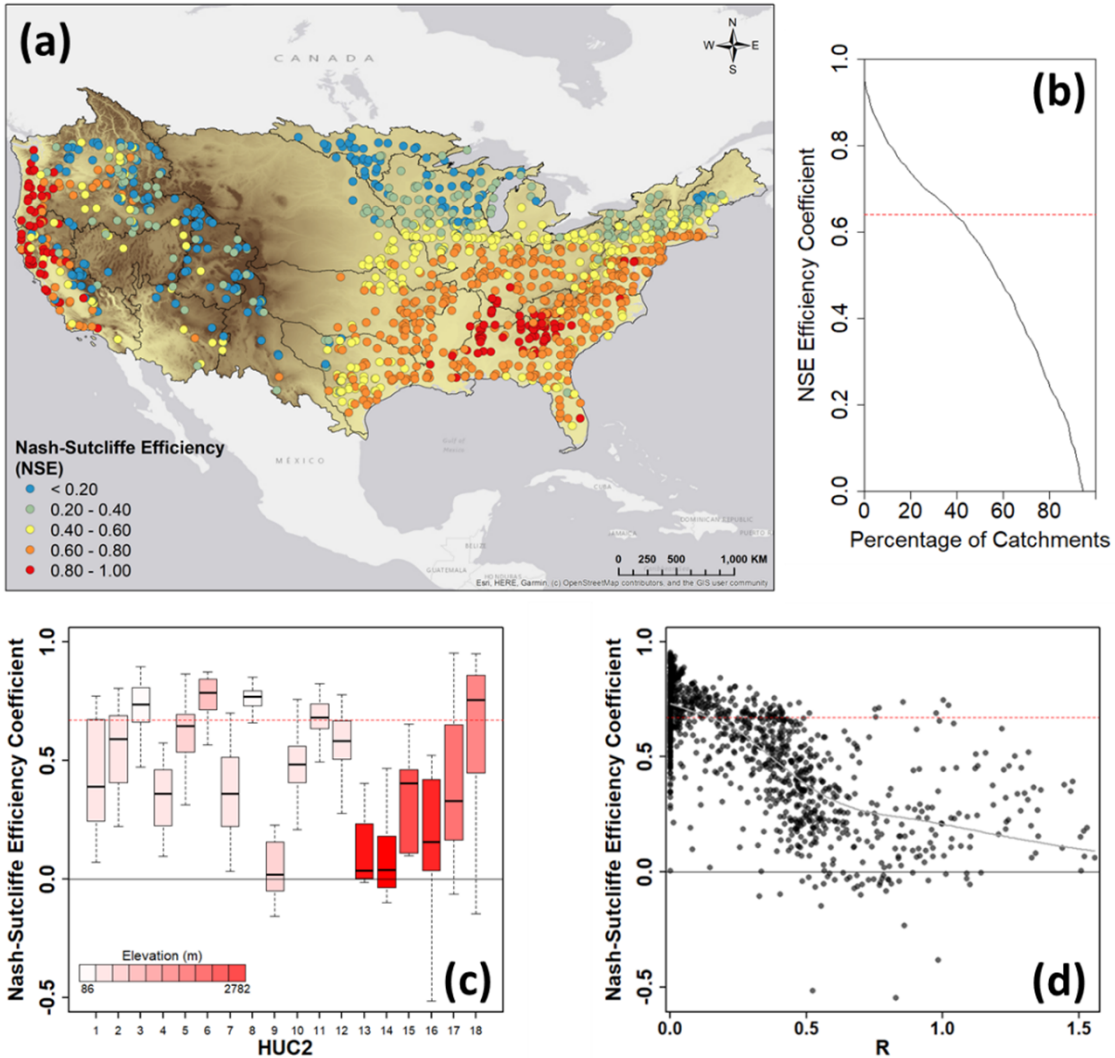


**Figure 3.4:** Performance of the original ZDWB across the CONUS: (a) spatial distribution of NSE across the CONUS (b) cumulative distribution function of NSE (c) distribution of NSE for each HUC2 region (d) dependence between NSE and the snow- factor R. The red horizontal dashed line in each subfigure indicates the threshold for a good model ( $\text{NSE} > 0.65$ )

(Zhang et al., 2008). The study used unimpaired streamflow data that was modeled without considering snowmelt water (Peel et al., 2000), which is reasonable since snow does not play a significant role in the hydrology of those tested catchments, except for a few high elevation areas in the southeast Australia and Tasmania region (Wang et al., 2011). However, the hydrology of a large area in the

CONUS is under the influence of snowmelt water to such an extent that more than 40% of the total HCDN catchments are snow-affected ( $R > 0.4$ ). Evidently, the lack of snow process representation leads to the underperformance of the model for the CONUS.

### 3.5.2 Model performance with the implanted snow module

After implanting the proposed snow module in ZDWBM (ZDWBM-snow), the model shows a significant improvement in estimating monthly streamflow, especially for snow-affected regions. Figure 3.5a displays the ZDWBM-snows NSE values across the CONUS. The median NSE value of ZDWBM-snow for the CONUS shows a slight improvement ( $< 0.1$ ), whereas it improves considerably from  $\sim 0.3$  to  $\sim 0.6$  for snow-affected regions. It can be seen from Figures 3.5a and 3.5c that NSE improves the most in the Northeastern region (HUC2 region 1 and 2) and Rocky Mountains region (HUC2 region 14, 16, and 17). Compared to the original model results, the median values of NSE in those areas increase to 0.33 on average, and the variance reduces remarkably. Stations where ZDWBM-snow shows *good* performance accounted for 51% of the total (Figure 3.5b), as opposed to 38% of the total for the original ZDWBM. As presented in Figure 3.5d, the association between the NSE values and snow-runoff ratio index R mostly diminishes after applying the snow module. Nevertheless, ZDWBM-snow still underperforms overall, showing NSE values less than 0.5 for 21% of the total catchments, especially in the northern part of the Midwest region (HUC2 region 4 and 9), where the catchments are heavily influenced by snow. This indicates that the model is not yet adequately capturing the hydrological process, including the complicated melting mechanism, for some areas where snow is dominantly affecting the local water

balance. There could be several aspects to consider in explaining these remaining errors. However, the most attributable factor is the single-value parameterization for describing the catchment's hydrological characteristics that can often vary from season to season.

Figure 3.6 demonstrates how the simulated flow differs from the observed flow (using pair-wise scatter plots, histograms of relative error, and percent bias) during different seasons across the CONUS, especially focusing on the snow-affected catchments ( $R > 0.4$ ). Percent bias is one of the evaluation statistics that measure simulated flow's average tendency to be larger or smaller than their corresponding observed data (Gupta, Sorooshian, and Yapo, 1999). Low magnitudes indicate accurate model estimation. Positive bias indicates that the model is underestimating the flow, whereas negative values indicate overestimation. The seasonal bias values of the snow implanted ZDWBM across all the 1,210 basins are 4%, 17%, 1%, and -22% for winter, spring, summer, and fall, respectively. The snow-affected regions show 16%, 15%, -3%, and -22% bias for each season from winter to fall, respectively. The inset in each subfigure displays the distribution of relative errors for all the catchments (light grey background) and the snow-affected catchments (transparent dark grey).

The histograms exhibit right-skewed distributions every season for both groups, as is expected of data which is bounded on the left tail. The lower limit of relative error is mathematically -1, while the upper bound is unlimited. From these results, we argue that, on average, the ZDWBM-snow tends to underestimate the streamflow during spring and overestimate during fall for the catchments across CONUS. The model underestimates monthly streamflow during winter and spring for snow-affected regions and overestimates the flow during fall. The model shows

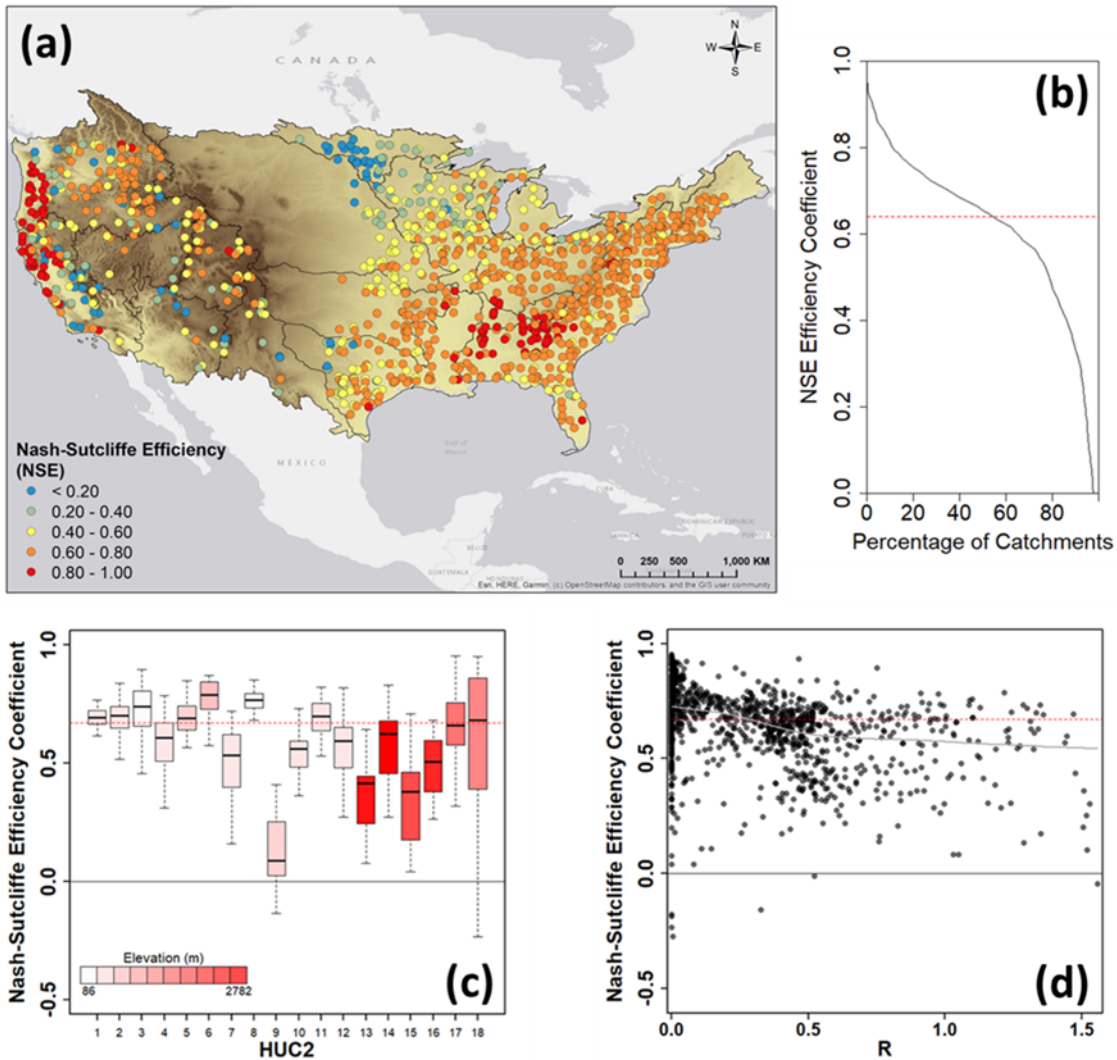


**Figure 3.5:** Performance of ZDWBM-snow across the CONUS: (a) spatial distribution of NSE across the CONUS (b) cumulative distribution function of NSE (c) distribution of NSE for each HUC2 region (d) dependence between NSE and the snow-factor R. The red horizontal dashed line in each subfigure indicates the threshold for a good model ( $\text{NSE} > 0.65$ )

a low bias during the summer season for both groups of basins. This seasonal bias is assumed as an error-offsetting result since the model's calibration process is designed to minimize the overall error with time-invariant parameters expected to represent the catchment's hydrological characteristics.

In practice, for example, the melting efficiency ( $\beta$ ) of a watershed should be

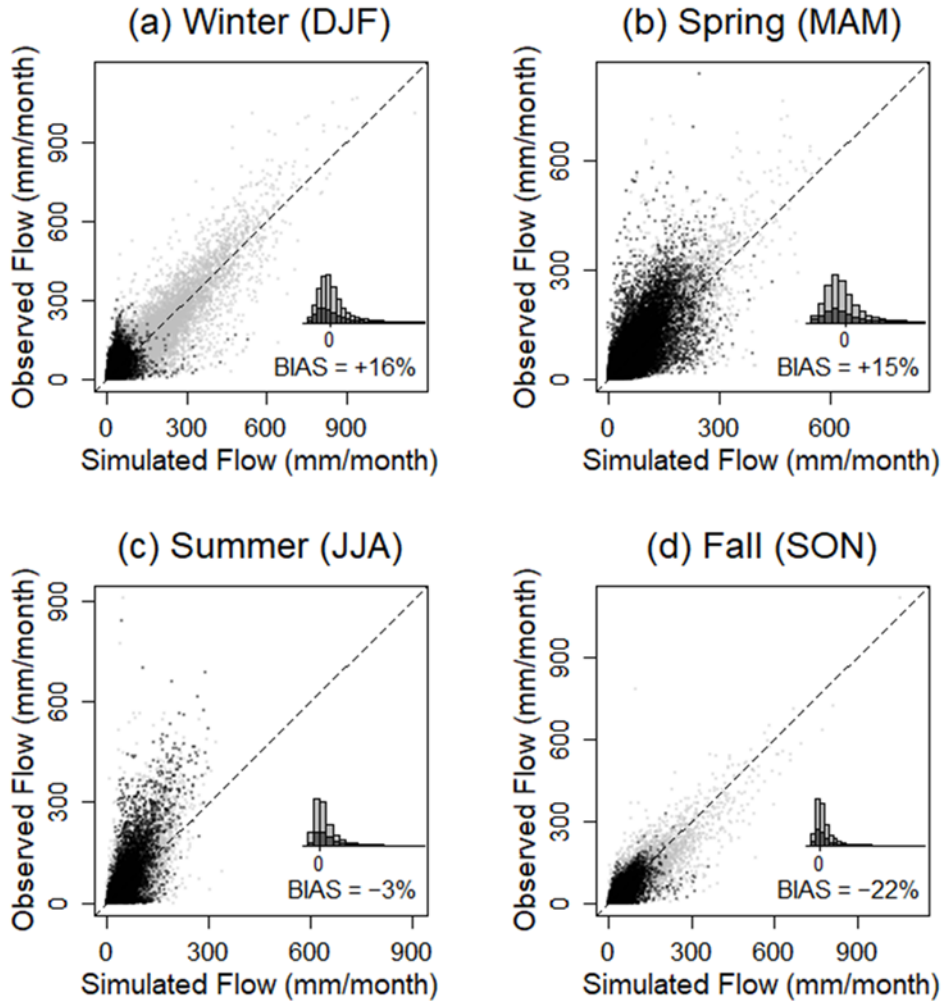


**Figure 3.6:** Bias of ZDWBM-snow for each season. The data points shown in gray indicate catchments that are not affected by snow ( $R < 0.4$ ), whereas the data points shown in black are snow-affected basins ( $R > 0.4$ ). The inset of each subfigure represents the histogram of relative errors between the observed and simulated for all catchments (gray) and snow-affected catchments (black).

relatively low for snow accumulation seasons but high for snow melting seasons. However, during the calibration process, the model determines a single-valued optimal  $\beta$  to minimize the overall error between the simulated and observed flows. This "time-invariant calibration" causes  $\beta$  to be overestimated for snow accumulation seasons and underestimated for snow melting seasons. This type of seasonal

bias can also occur to the other model parameters ( $\alpha_1$ ,  $\alpha_2$ ,  $d$ ,  $S_{max}$ ) as long as they are introduced as time-invariant values. Even if the true values of parameters are nearly constant, changing very little over time, streamflow can be highly sensitive to those small changes. Therefore, we reckon single-value parameters are insufficient to fully account for the temporal variability of the catchment's hydrological characteristics.

### 3.5.3 Model performance with the implanted snow module and monthly parameterization

ZDWBM-snow is calibrated against observed streamflow data with five parameters ( $\alpha_{1n}$ ,  $\alpha_{2n}$ ,  $d_n$ ,  $S_{maxn}$ , and  $\beta_n$ ) that vary over the twelve months ( $n = 1 : 12$ ). The model performance significantly improves when a combination of the snow module and monthly parameterization is applied. Figure 3.7a maps the spatial distribution of the new NSE values across the CONUS. Except for a few, most catchments across the CONUS show a good agreement between the simulated flow and observed flow according to the computed NSE coefficients. The median NSE values for CONUS and snow-affected regions are both  $\sim 0.8$ . The accuracy of the monthly calibrated ZDWBM-snow (ZDWBM-msnow) is evaluated to be *good* for 83% of the total HCDN catchments (Figure 3.7b). According to Figure 3.7c, catchments in HUC2 regions 9 and 15 tend to show relatively poor model performances than others. The elevation and snow-runoff ratio do not show any correspondence with the model performance (Figure 3.7c and 3.7d).

Figure 3.8 shows the percent bias between the simulated flow and observed flow of ZDWBM-msnow. Compared to the model without monthly parameterization, ZDWBM-msnow shows significantly lower bias for catchments across the CONUS, including the areas affected by snow, regardless of the season. Across

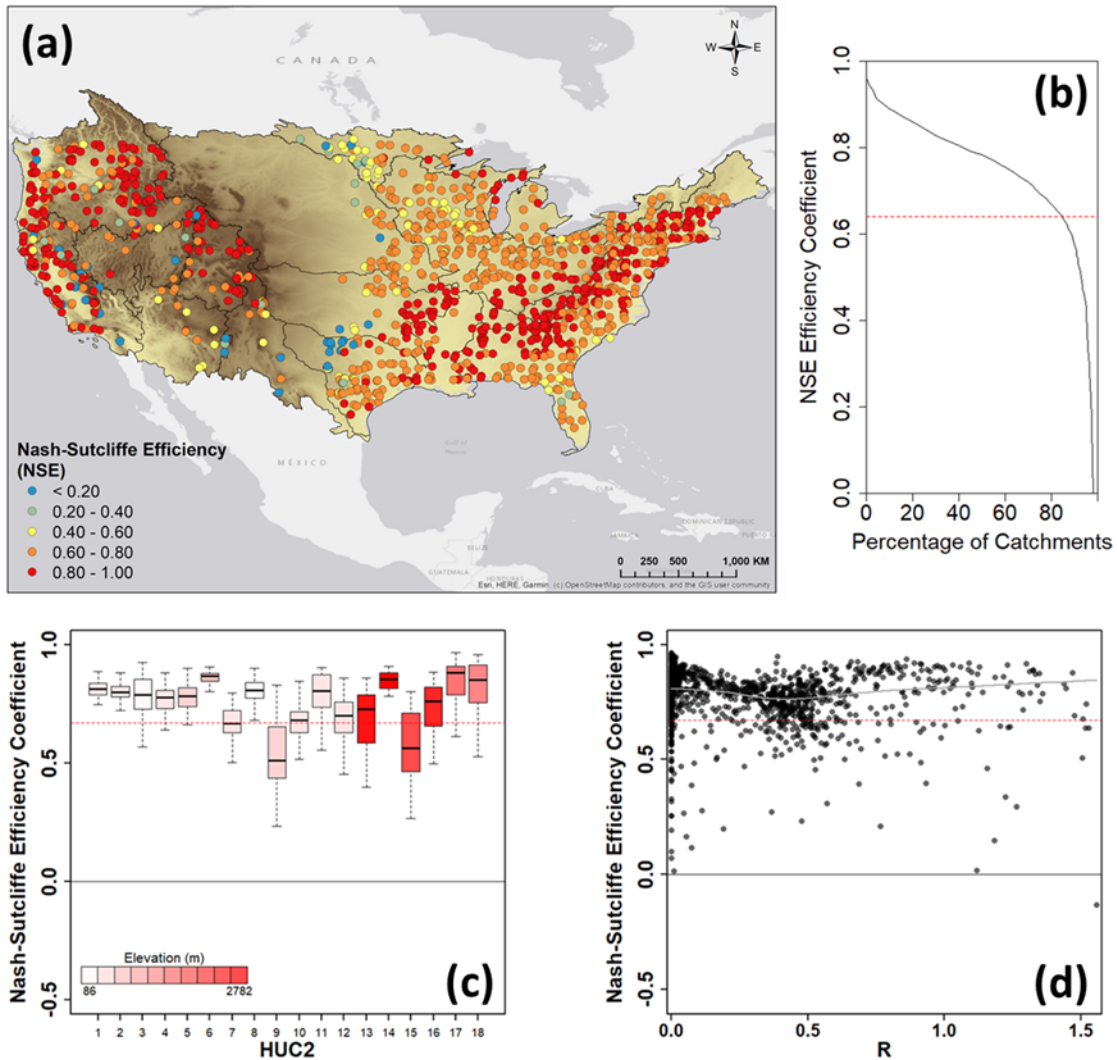


**Figure 3.7:** Performance of ZDWBM-msnow across the CONUS: (a) spatial distribution of NSE across the CONUS (b) cumulative distribution function of NSE (c) distribution of NSE for each HUC2 region (d) dependence between NSE and snow-factor R. The red horizontal dashed line in each subfigure indicates the threshold for a good model ( $\text{NSE} > 0.65$ )

the 1,210 catchments, the model bias is estimated as -1%, 3%, -0.1%, and 3% for each season, respectively, from winter to fall. Compared to the previous biases (4%, 17%, 1%, and -22%), both the magnitude and seasonal variance of the bias have decreased. The bias for snow-affected catchments also shows small values

through winter to fall, estimated as 3%, -3%, -1%, and 1%, respectively. This is considered a promising improvement, given the previous biases for the corresponding catchments are 16%, 15%, -3%, and -22%, respectively.

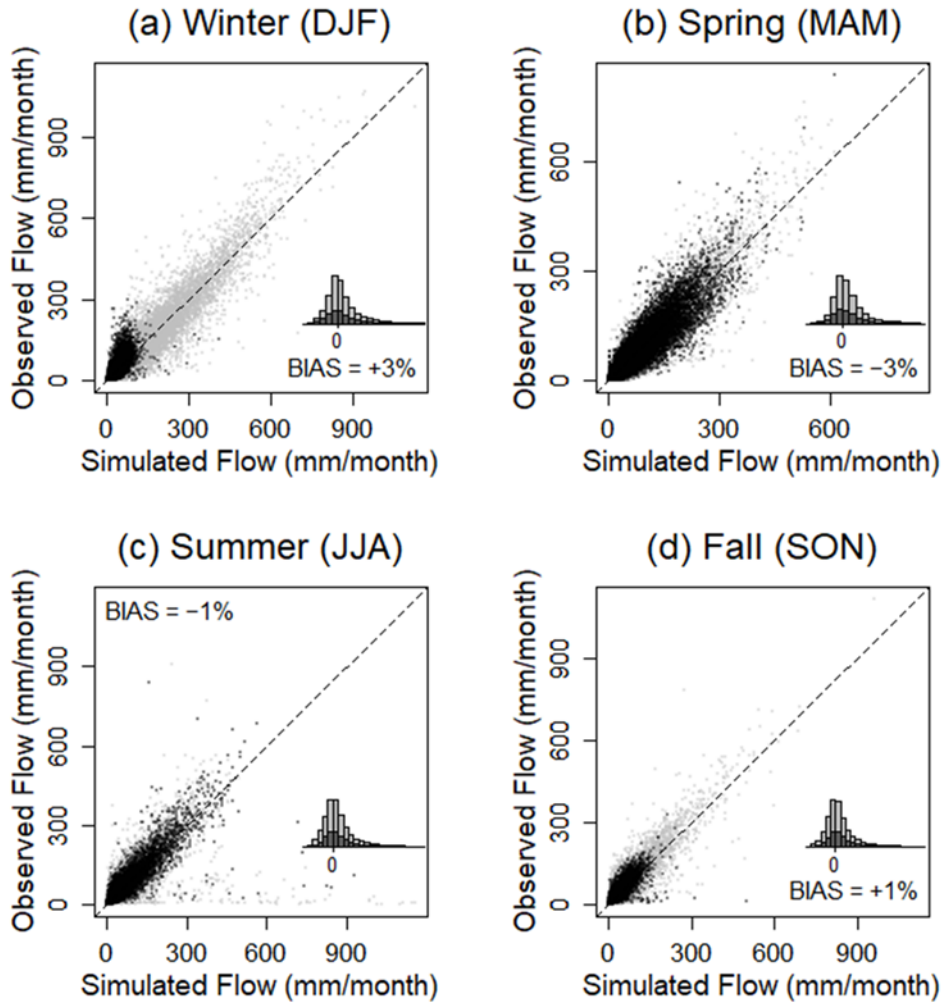


**Figure 3.8:** Bias of ZDWBM-msnow for each season. The data points shown in gray indicate catchments that are not affected by snow ( $R < 0.4$ ), whereas the data points shown in black are snow-affected basins ( $R > 0.4$ ). The inset of each subfigure represents the histogram of relative errors between the observed and simulated for all catchments (gray) and snow-affected catchments (black).

### 3.5.4 Assessment and validation of the model improvements

Comparing the model performance after applying both the snow module and monthly parameterization (ZDWBM-msnow) is summarized in Figure 3.9. NSE of ZDWBM is compared to the NSE of ZDWBM-msnow. For clarity, NSE values less than -0.75 are chosen as lower outliers and omitted from the figure. These are less than 2% of all the 1,210 stations. The figure clearly shows that the model performs better after applying the proposed methods. The median NSE increases to  $\sim 0.8$  from  $\sim 0.6$  for all the catchments, and only 7% of them show NSE less than 0.5. Catchments with the most significant improvements in model performance are hydrologically snow-dominated ( $R > 0.5$ ), while catchments moderately affected by snow ( $0.4 < R \leq 0.5$ ) show marginal improvements. The median NSE of the original model for snow-dominated catchments was  $\sim 0.2$ , and this dramatically increases to  $\sim 0.8$  with ZDWBM-msnow. Whereas the original model was evaluated as *unsatisfactory* ( $NSE < 0.5$ ) for 88% of these catchments, ZDWBM-msnow underperforms in only 13% of them. For most of the basins where snow is not considered an important local water source ( $R < 0.4$ ), the final model shows a slightly better, or at least similar, performance compared to the original model, with few exceptions. Most of these exceptions happen in the catchments less affected ( $R < 0.4$ ) or dominated ( $R > 0.5$ ) by snow. The degradation of the model performance in these catchments could be due to the misallocation of available energy for melting.

An additional comparison shows that ZDWBM-msnow performs better without the snow module, but this may be attributable to the calibration flexibility of the model due to its large number of parameters, misrepresenting basin characteristics and partitioning process, especially in snow-affected basins. The two-layer storage components of the model could control the effect of the snowmelt process

without snow representation, and thus we argue its partitioning process inaccurate. This could be tested by cross-validating the model.

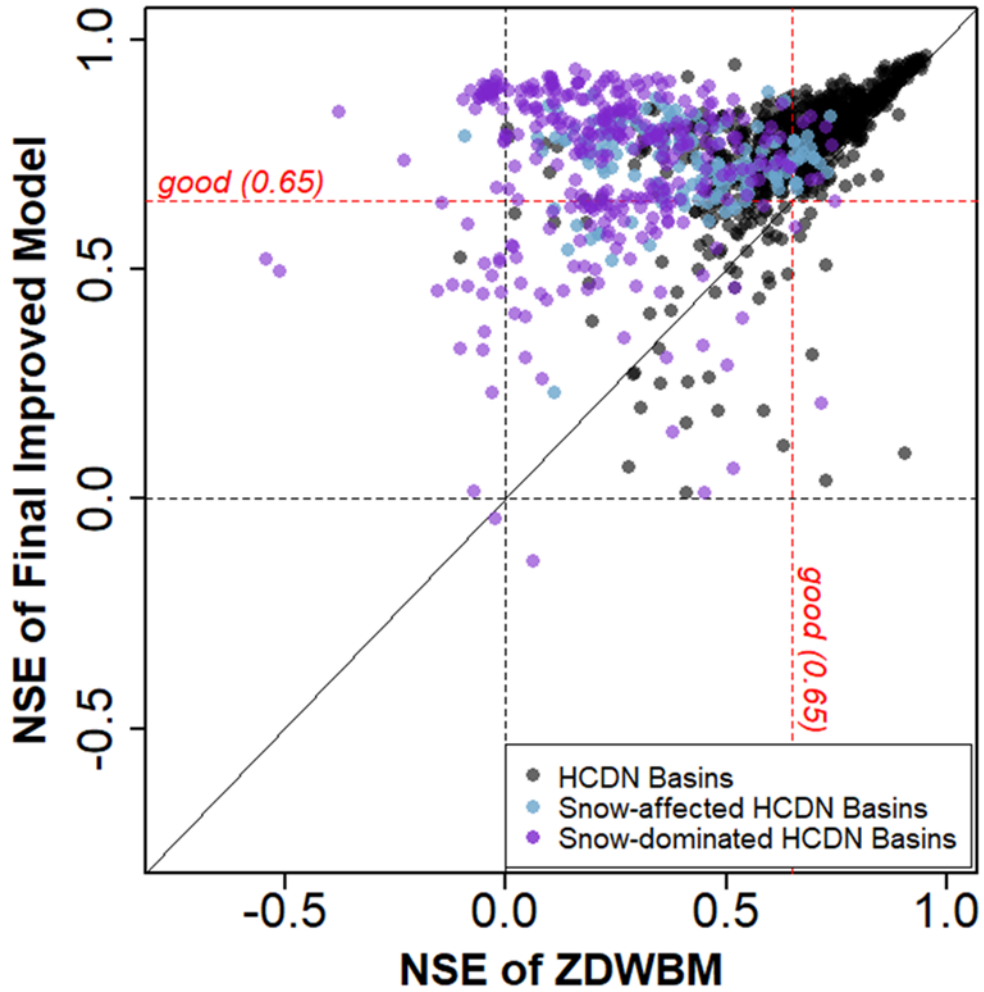


**Figure 3.9:** Comparison of NSE for ZDWBM-msnow and original ZDWBM.

As ZDWBM-msnow includes a snow module with an increased number of parameters due to the monthly parameterization, the model's complexity increases, and thus we cross-validate the model to test overfitting. Overfitting tends to occur when the model is unnecessarily complex, incorporating unnecessary processes (Vanlier et al., 2014), and when it contains an excessive number of parameters

(Orth et al., 2015). The problem of overfitted models lies in the fact that they try to fit the random noise rather than only the signal. It typically shows a remarkable performance during the calibration stage and seems to capture the underlying hydrological process accurately, but it exhibits significant performance degradation during the validation period.

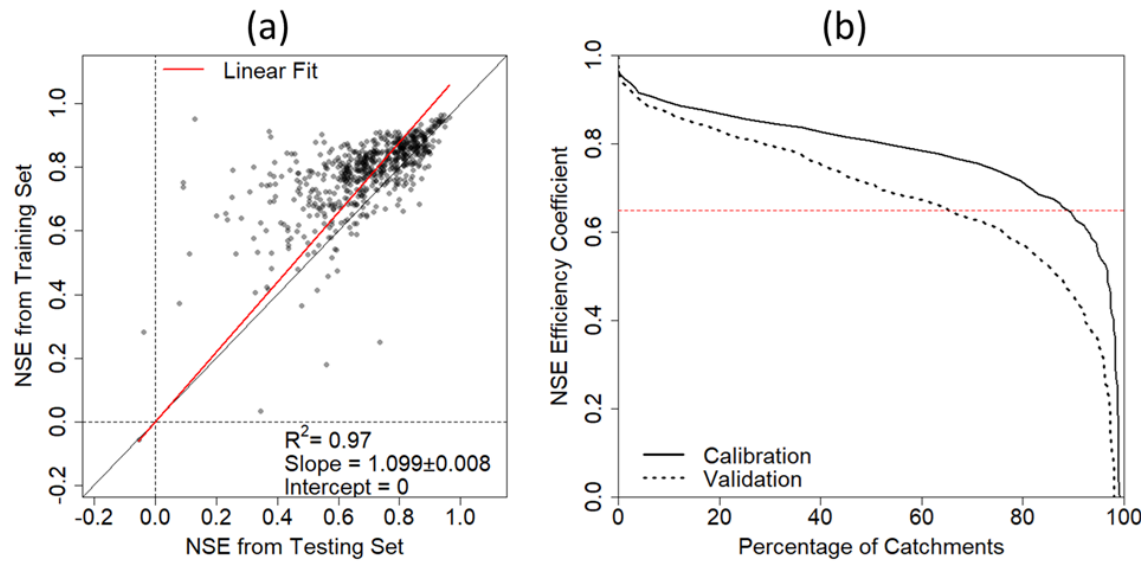


**Figure 3.10:** Cross-validation results verifying for overfitting. (a) Comparison between NSE from calibration and validation periods (b) Comparison between the cumulative distribution function of NSE from calibration (solid) and validation periods (dotted).

We only focus on 636 catchments for the cross-validation test, where 37 years of continuous observed streamflow data are provided. After calibrating the model against the first 25 years (~66% of 37 years) of data (training set), the model is validated with the last 12 years (testing set). Figure 3.10a compares the NSE values of ZDWBM-msnow from the calibration and validation procedures. When the intercept is set to zero, the overall  $R^2$  of the regression of calibrated NSE on simulated NSE is calculated as 0.97, indicating a good correspondence between calibrated NSE and simulated NSE. Besides, the slope of the fitted line is 1.099 with a 0.008 standard error. For a cross-validation test, it is ideal to have the points settled on

the fitted line with a slope of 1 and an intercept of 0. Most of the tested results here are adjacent to the 1:1 line, except for a few cases. These outliers could be due to the climatic or catchment characteristics differences between the calibration and validation periods. The percentage of catchments where the model showed a *good* performance was greater during the calibration period than the validation period, but their distributions of NSE values did not show a big difference (Figure 3.10b). This trend is expected as the model training involves observed streamflow while testing is blind to the observed. Overall, the differences between the calibration and validation results lie within the range that could be expected, and thus we conclude the proposed model does not show a concerning level of overfitting.

### 3.5.5 Assessment of Model Parameters

Here we explore the spatial and seasonal variability of the calibrated parameters of the final model, ZDWBM-msnow. To ensure that the interpretations are reasonable, we only consider catchments where the model performance is evaluated as *good*. This selection provided us 1,008 HCDN basins across CONUS for further investigation. Monthly parameters are explored based on the four seasons by averaging the monthly values corresponding to each season: winter (December February), spring (March May), summer (June August), and fall (September November). The spatial distribution of the parameters for each season is shown in Figure 3.11.

The melting efficiency ( $\beta_n$ ) displays a significant seasonality for most of the catchments, as anticipated. During the winter season, groups of catchments with the highest values of  $\beta_n$  are located in the Pacific Coast and southern part of the CONUS. As spring comes,  $\beta_n$  starts to increase in catchments located northbound

of the South and Southeast region, and this increase of  $\beta_n$  continues northward as summer approaches. When summer arrives, most of the catchments in the CONUS have high melting efficiency ( $\beta_n > 0.8$ ), and this state is maintained until fall.

The catchment retention efficiency ( $\alpha_{1n}$ ) shows a seasonal variability for some catchments across the CONUS. During winter and spring, the eastern U.S. generally shows lower  $\alpha_{1n}$  values than the western U.S., but this relation overturns in summer and fall. Especially during the spring season, the Northeast and Ohio Valley (HUC2 region 5) regions display particularly low  $\alpha_{1n}$  values. Since  $\alpha_{1n}$  describes catchment retention, this cluster of low  $\alpha_{1n}$  in spring may imply a low infiltration rate and intense water supply, indicating more direct runoff in the area. We assume this is strongly related to snowmelt in spring.

The evapotranspiration efficiency ( $\alpha_{2n}$ ) shows varying peak timings for different regions across the CONUS. The South and Ohio Valley regions show quasi-constant  $\alpha_{2n}$  values  $\sim 0.6 - 0.8$  regardless of the seasons. Meanwhile, the Pacific Coast near California shows highest  $\alpha_{2n}$  during the spring season and lowest during summer and fall. The rest of the catchments mostly show highest  $\alpha_{2n}$  during the summer season, especially those located in the Northeast, Pacific Northwest, and Upper Midwest regions. A previous study argues that  $\alpha_{2n}$  is heavily related to various climate factors, such as precipitation, aridity index, peak-lags between precipitation and evapotranspiration, and coefficient of variation of precipitation ([hamel2017a](#)). In fact, the spatial distribution of  $\alpha_{2n}$  displays a similar pattern to the aridity index gradient of the CONUS (Petersen, Devineni, and Sankarasubramanian, [2012](#)).

The groundwater transition rate ( $d_n$ ) displays a strong spatial and seasonal variability for the catchments across the CONUS. Most of the catchments have a low

to moderate value of  $d_n$  during winter. The  $d_n$  values generally increase as spring arrives and reaches the peak for most catchments, except for those located in the Upper Midwest region. During the summer season,  $d_n$  decreases at some catchments, including the Tennessee Valley (HUC2 region 6) and Pacific Coast, but remains at a similar level from spring for most catchments. Then the majority of the catchments show a decrease in  $d_n$ , having their lowest  $d_n$  values in fall.

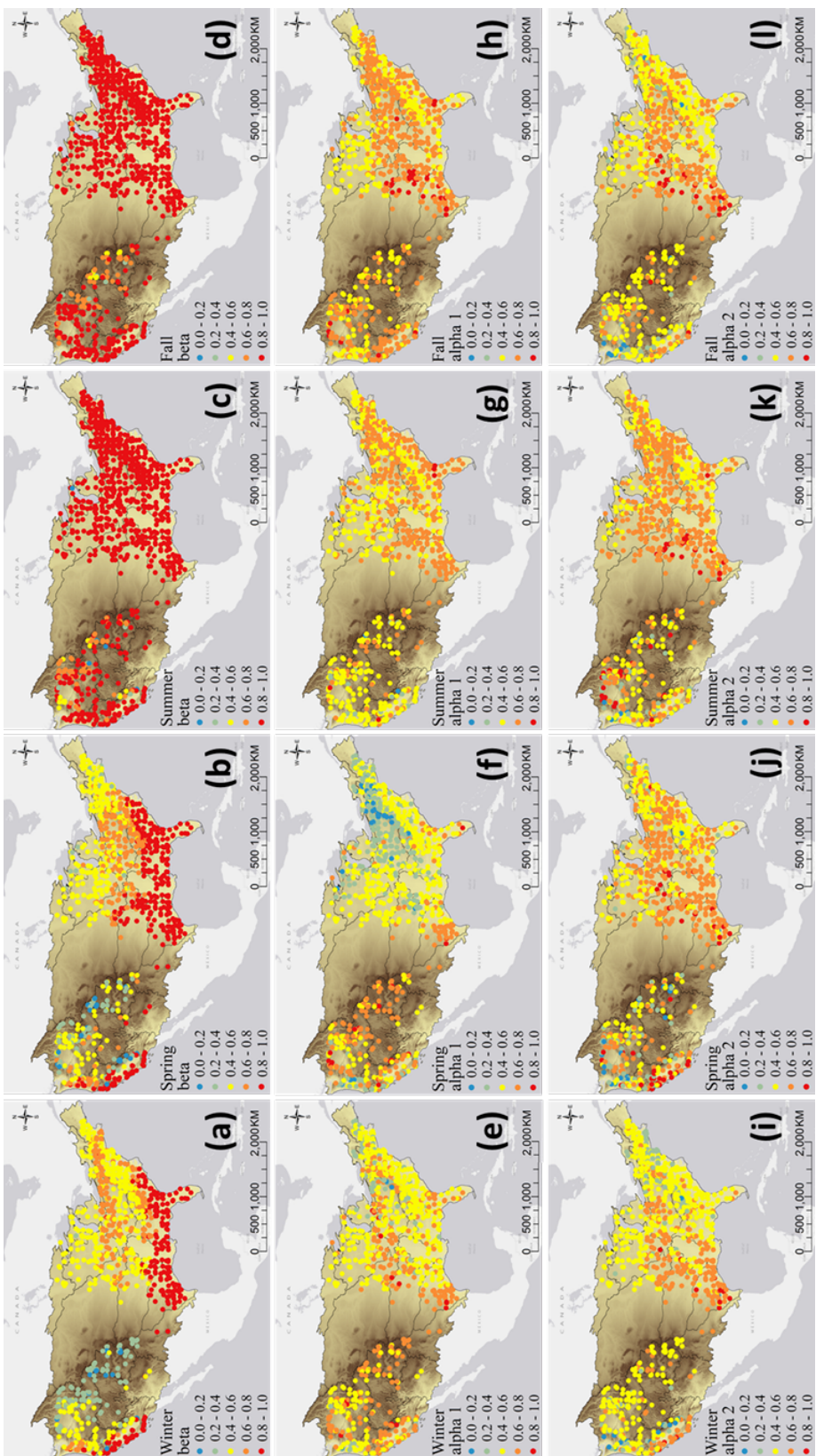
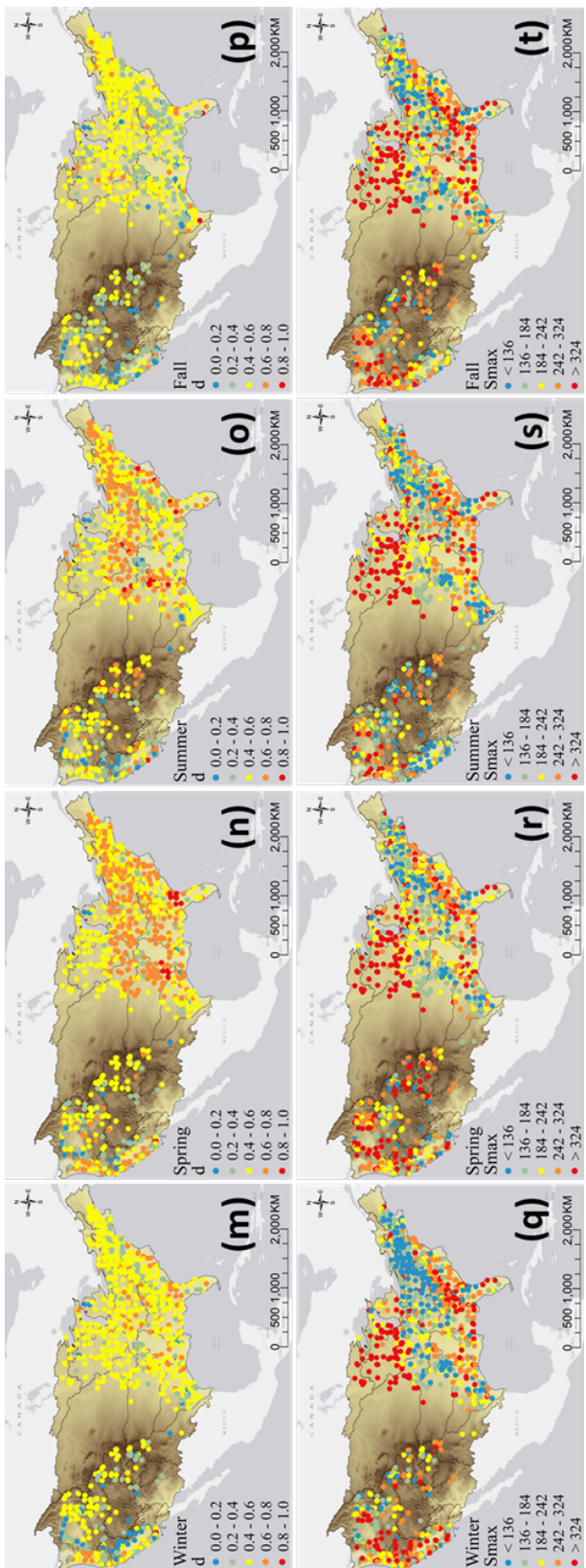


**Figure 3.11:** Seasonal spatial distribution of average melting efficiency (*a - d*), catchment retention efficiency (*e - h*), evapotranspiration efficiency (*i - l*), groundwater transition rate (*m - p*), and maximum soil-moisture capacity (*q - t*) for the HCDN catchments where ZDWBM-msnow performance was classified as good during the calibration. Figure continued on next page.



The maximum soil-moisture storage capacity ( $S_{max,n}$ ) is consistently high in the Midwest region and northbound of the Southeast region, while being relatively low in the Ohio Valley and Northeast regions throughout the four seasons. Catchments in close proximity to the Rocky Mountains Range, including those in California, have lowest  $S_{max,n}$  in summer.

### 3.6 Summary and Conclusion

This study explores the limitations of an existing dynamic water balance model (ZDWBM) proposed by Zhang et al. (2008). It provides measures to overcome those limits based on more than 1,200 unmodified basins across the continental United States with observation data of 31 years on average. Zhang's dynamic water balance model (ZDWBM) describes the monthly water balance of a catchment by partitioning the hydrological process based on Budyko's framework. While this model showed a quality performance for catchments in Australia (Zhang et al., 2008), it fails to perform well for the catchments in the continental United States. The model mainly shows lower performance in snow-affected basins as it does not contain snow components. This limitation of the model is critical when applied to the United States since a significant portion of its catchments is affected by snow. The model suits only 57% of the given catchments and 18% of the snow-affected regions.

A snow module that can be implanted to ZDWBM is developed in this study to improve the model applicability to the continental United States. The snow module is designed based on the concept of Budyko's framework to preserve the spirit and parameter parsimony that ZDWBM has achieved. The augmented model with snow module shows a significant improvement in simulating monthly streamflow,

especially for snow-affected regions. However, we find the augmented model produces a seasonal bias in the simulated streamflow, requiring an additional improvement strategy. We assume the model's seasonal bias is attributable to the time-invariant model parameters inaccurately representing the time-varying catchment characteristics. In order to minimize the seasonal bias, the snow augmented model is calibrated with monthly parameters. After applying monthly parameterization to the snow augmented model, it becomes suitable for more than 90% of the total catchment. Moreover, the seasonal bias diminishes. Based on a cross-validation test, it is confirmed that the model is not overfitting against observed streamflow.

Based on the ZDWBM-msnow, we also discussed the catchments hydrological characteristics across the CONUS by assessing the spatial variability of the model parameters for each season. For each model parameter, catchments with similar values are regionally grouped as various clusters in general. While catchment melting efficiency ( $\beta_n$ ), retention efficiency ( $\alpha_{1n}$ ), evapotranspiration efficiency ( $\alpha_{2n}$ ), and groundwater transition rate ( $d_n$ ) display seasonal variations in most catchments, the maximum soil-moisture storage capacity ( $S_{maxn}$ ) shows only small changes over the four seasons. Further investigations are required to better understand the factors that control this spatiotemporal variability of the parameters.

Overall, ZWBM-msnow displays superior performance in simulating monthly streamflow for the catchments across the United States. However, some catchments remain to be poor. In reality, negative radiation balance can be observed during snow accumulating seasons or in regions of permanent snow and ice cover. However, our estimated net radiation heat flux is assumed to be always positive

since the calculations are based on positive only potential evapotranspiration values. This leaves latent heat from condensation and freezing neglected, inducing the model to have potential errors for certain catchments under the influence of snow. Additionally, the rough estimate of allocating the total energy for potential evapotranspiration and potential melting is expected to introduce a certain level of errors. For further studies, in addition to improving the epistemic uncertainties of the hydro-climatological basis of the model, one may consider redesigning the model using a Bayesian hierarchical structure to enhance the parameter estimation procedure. By pooling the parameters over similar geospatial catchments, a Bayesian hierarchical approach can provide improved model parameters with reduced uncertainty. Since the model parameters are related to the hydrological characteristics of a catchment, a further investigation on the model parameters and catchment characteristics could be conducted to predict the streamflow response to changes in land-use/land cover for catchments, including those ungauged. A successful analysis of the relationship between catchment characteristics and the model parameters will provide further physical interpretation and allow easy applicability for decision-making for various purposes, such as water resources management, restoration of ecological flow, and water-relevant policymaking.

# References

- Anderson, M.G. and T.P. Burt (1985). *Modelling strategies. Hydrological Forecasting.* en. New York, New York.
- Bai, J., J. Li, H. Shi, T. Liu, and R. Zhong (2018). "Snowmelt Water Alters the Regime of Runoff in the Arid Region of Northwest China". en. In: *Water* 10.7, p. 902.
- Bai, P., X. Liu, K. Liang, and C. Liu (2015). "Comparison of performance of twelve monthly water balance models in different climatic catchments of China". en. In: *Journal of Hydrology* 529, pp. 10301040.
- Barnett, T.P., J.C. Adam, and D.P. Lettenmaier (2005). "Potential impacts of a warming climate on water availability in snow-dominated regions". en. In: *Nature* 438.7066, pp. 303309.
- Beven, K., R. Lamb, P. Quinn, R. Romanowicz, and J. Freer (1995). "Topmodel". en. In: *Computer models of watershed hydrology*, pp. 627668.
- Boudhar, Abdelghani, Gilles Boulet, Lahoucine Hanich, Jean Emmanuel Sicart, and Abdelghani Chehbouni (2016). "Energy fluxes and melt rate of a seasonal snow cover in the Moroccan High Atlas". In: *Hydrological Sciences Journal* 61.5, pp. 931–943.
- Budyko, M.I. (1961). "The heat balance of the earth's surface". en. In: *Soviet Geography* 2.4, pp. 313.
- Budyko, M.I., D.H. Miller, and D.H. Miller (1974). *Climate and life*. en. Vol. 508. New York: Academic press.
- Chen, X., N. Alimohammadi, and D. Wang (2013). "Modeling interannual variability of seasonal evaporation and storage change based on the extended Budyko framework". en. In: *Water Resources Research* 49.9, pp. 60676078.
- Daly, C., R.P. Neilson, and D.L. Phillips (1994). "A statistical-topographic model for mapping climatological precipitation over mountainous terrain". en. In: *Journal of Applied Meteorology and Climatology* 33.2, pp. 140158.
- Deng, C., P. Liu, D. Wang, and W. Wang (2018). "Temporal variation and scaling of parameters for a monthly hydrologic model". en. In: *Journal of Hydrology* 558, pp. 290300.
- Eagleson, P.S. (1978). "Climate, soil, and vegetation: 1. Introduction to water balance dynamics". en. In: *Water Resources Research* 14.5, pp. 705712.

- Ehret, U. and E. Zehe (2011). "Series distancean intuitive metric to quantify hydrograph similarity in terms of occurrence, amplitude and timing of hydrological events". en. In: *Hydrology and Earth System Sciences* 15.3, pp. 877896.
- Farmer, D., M. Sivapalan, and C. Jothityangkoon (2003). "Climate, soil, and vegetation controls upon the variability of water balance in temperate and semiarid landscapes: Downward approach to water balance analysis". en. In: *Water Resources Research* 39.2.
- Fayad, A., S. Gascoin, G. Faour, J.I. López-Moreno, L. Drapeau, M. Le Page, and R. Escadafal (2017). "Snow hydrology in Mediterranean mountain regions: A review". en. In: *Journal of Hydrology* 551, pp. 374396.
- Fekete, B.M., D. Wisser, C. Kroeze, E. Mayorga, L. Bouwman, W.M. Wollheim, and C. Vörösmarty (2010). "Millennium ecosystem assessment scenario drivers (19702050): climate and hydrological alterations". fr. In: *Global Biogeochemical Cycles* 24.4.
- Franks, S.W., M. Sivapalan, K. Takeuchi, and Y. Tachikawa (2005). "Predictions in ungauged basins: international perspectives on the state of the art and pathways forward". en. In: *Food and Agriculture Organization*.
- Fu, BP (1981). "On the calculation of the evaporation from land surface". In: *Sci. Atmos. Sin* 5.1, pp. 23–31.
- Gupta, H.V. and H. Kling (2011). "On typical range, sensitivity, and normalization of Mean Squared Error and NashSutcliffe Efficiency type metrics". en. In: *Water Resources Research* 47.10.
- Gupta, H.V., S. Sorooshian, and P.O. Yapo (1999). "Status of automatic calibration for hydrologic models: Comparison with multilevel expert calibration". en. In: *Journal of hydrologic engineering* 4.2, pp. 135143.
- Hargreaves, G.H. and Z.A. Samani (1982). "Estimating potential evapotranspiration". en. In: *Journal of the irrigation and Drainage Division* 108.3, pp. 225230.
- Harman, C. and P.A. Troch (2014). "What makes Darwinian hydrology" Darwinian"? Asking a different kind of question about landscapes". en. In: *Hydrology and Earth System Sciences* 18.2, pp. 417433.
- Koster, R.D. and M.J. Suarez (1999). "A simple framework for examining the interannual variability of land surface moisture fluxes". en. In: *Journal of Climate* 12.7, pp. 19111917.
- Li, D., M. Pan, Z. Cong, L. Zhang, and E. Wood (2013). "Vegetation control on water and energy balance within the Budyko framework". en. In: *Water Resources Research* 49.2, pp. 969976.
- Liang, X., D.P. Lettenmaier, E.F. Wood, and S.J. Burges (1994). "A simple hydrologically based model of land surface water and energy fluxes for general circulation models". en. In: *Journal of Geophysical Research: Atmospheres* 99.D7, pp. 1441514428.

- Martinez, Guillermo F and Hoshin V Gupta (2010). "Toward improved identification of hydrological models: A diagnostic evaluation of the abcd monthly water balance model for the conterminous United States". In: *Water Resources Research* 46.8.
- Mazurkiewicz, Adam B, David G Callery, and Jeffrey J McDonnell (2008). "Assessing the controls of the snow energy balance and water available for runoff in a rain-on-snow environment". In: *Journal of Hydrology* 354.1-4, pp. 1–14.
- Miller, D.M. (1982). *Water at the Surface of Earth: An Introduction to Ecosystem Hydrodynamics*. en. Vol. 21. Academic Press.
- Milly, P.C.D. (1994). "Climate, soil water storage, and the average annual water balance". en. In: *Water Resources Research* 30.7, pp. 21432156.
- Moriasi, D.N., J.G. Arnold, M.W. Van Liew, R.L. Bingner, R.D. Harmel, and T.L. Veith (2007). "Model evaluation guidelines for systematic quantification of accuracy in watershed simulations". en. In: *Transactions of the ASABE* 50.3, pp. 885900.
- Mouelhi, Safouane, Claude Michel, Charles Perrin, and Vazken Andréassian (2006). "Stepwise development of a two-parameter monthly water balance model". In: *Journal of Hydrology* 318.1-4, pp. 200–214.
- Nash, J.E. and J.V. Sutcliffe (1970). "River flow forecasting through conceptual models part IA discussion of principles". en. In: *Journal of hydrology* 10.3, pp. 282290.
- Orth, R., M. Staudinger, S.I. Seneviratne, J. Seibert, and M. Zappa (2015). "Does model performance improve with complexity? A case study with three hydrological models". en. In: *Journal of Hydrology* 523, pp. 147159.
- Padrón, R.S., L. Gudmundsson, P. Greve, and S.I. Seneviratne (2017). "Largescale controls of the surface water balance over land: Insights from a systematic review and metaanalysis". en. In: *Water Resources Research* 53.11, pp. 96599678.
- Peel, M.C., F.H. Chiew, A.W. Western, and T.A. McMahon (2000). "Extension of unimpaired monthly streamflow data and regionalisation of parameter values to estimate streamflow in ungauged catchments". en. In: *Report to the National Land and Water Resources Audit*.
- Petersen, T., N. Devineni, and A. Sankarasubramanian (2018). "Monthly hydroclimatology of the continental United States". en. In: *Advances in Water Resources* 114, pp. 180195.
- Petersen, T., N. Devineni, and A. Sankarasubramanian (2012). "Seasonality of monthly runoff over the continental United States: Causality and relations to mean annual and mean monthly distributions of moisture and energy". en. In: *Journal of hydrology* 468, pp. 139150.
- Pike, J.G. (1964). "The estimation of annual run-off from meteorological data in a tropical climate". en. In: *Journal of Hydrology* 2.2, pp. 116123.

- Reggiani, P., M. Sivapalan, and S.M. Hassanzadeh (2000). "Conservation equations governing hillslope responses: Exploring the physical basis of water balance". en. In: *Water Resources Research* 36.7, pp. 18451863.
- Sankarasubramanian, A and Richard M Vogel (2002b). "Comment on the paper: Basin hydrologic response relations to distributed physiographic descriptors and climate by Karen Plaut Berger, Dara Entekhabi, 2001. Journal of Hydrology 247, 169–182". In: *Journal of Hydrology* 263.1-4, pp. 257–261.
- Sankarasubramanian, A. and R.M. Vogel (2002a). "Annual hydroclimatology of the United States". en. In: *Water Resources Research* 38.6, pp. 191.
- Sankarasubramanian, A., D. Wang, S. Archfield, M. Reitz, R.M. Vogel, A. Mazrooei, and S. Mukhopadhyay (2020). "HESS Opinions: Beyond the long-term water balance: evolving Budyko's supplydemand framework for the Anthropocene towards a global synthesis of land-surface fluxes under natural and human-altered watersheds". en. In: *Hydrology and Earth System Sciences* 24.4, pp. 19751984.
- Schaefli, B. and H.V. Gupta (2007). "Do Nash values have value?" en. In: *Hydrological Processes: An International Journal* 21.15, pp. 20752080.
- Schreiber, P. (1904). "Über die Beziehungen zwischen dem Niederschlag und der Wasserführung der Flüsse in Mitteleuropa". de. In: *Z. Meteorol* 21.10, pp. 441452.
- Shook, K. and D.M. Gray (1997). "Snowmelt resulting from advection". en. In: *Hydrological Processes* 11.13, pp. 17251736.
- Sivapalan, M., K. Takeuchi, S.W. Franks, V.K. Gupta, H. Karambiri, V. Lakshmi, and E. Zehe (2003). "IAHS Decade on Predictions in Ungauged Basins (PUB), 20032012: Shaping an exciting future for the hydrological sciences". en. In: *Hydrological sciences journal* 48.6, pp. 857880.
- Sivapalan, M. and P.C. Young (2006). "Downward approach to hydrological model development". en. In: *Encyclopedia of hydrological sciences*.
- Slack, J.R., A. Lumb, and J.M. Landwehr (1993). *Hydro-Climatic Data Network (HCDN) Streamflow Data Set, 1874-1998*. en. Reston, Virginia. URL: <http://www.daac.ornl.gov>.
- Sposito, Garrison (2017). "Understanding the Budyko equation". In: *Water* 9.4, p. 236.
- Stewart, Iris T, Daniel R Cayan, and Michael D Dettinger (2005). "Changes toward earlier streamflow timing across western North America". In: *Journal of climate* 18.8, pp. 1136–1155.
- Tekleab, S., S. Uhlenbrook, Y. Mohamed, H.H.G. Savenije, M. Temesgen, and J. Wenninger (2011). "Water balance modeling of Upper Blue Nile catchments using a top-down approach". en. In: *Hydrology and Earth System Sciences* 15.7, pp. 21792193.
- TheMathworksInc (2016). *Global Optimization Toolbox: Users Guide*. URL: [https://www.mathworks.com/help/pdf\\_doc/gads/gads.pdf](https://www.mathworks.com/help/pdf_doc/gads/gads.pdf).

- Thomas, H.A. (1981). *Improved methods for national water assessment*. en. Report WR15249270, Washington, DC: US Water Resource Council.
- Thornthwaite, C.W. (1948). "An approach toward a rational classification of climate". en. In: *Geographical review* 38.1, pp. 5594.
- Vandewiele, GL, Chong-Yu Xu, et al. (1992). "Methodology and comparative study of monthly water balance models in Belgium, China and Burma". In: *Journal of Hydrology* 134.1-4, pp. 315–347.
- Vanlier, J., C.A. Tiemann, P.A. Hilbers, and N.A. Riel (2014). "Optimal experiment design for model selection in biochemical networks". cs. In: *BMC systems biology* 8.1, pp. 116.
- Vogel, Richard M and A Sankarasubramanian (2000). "Spatial scaling properties of annual streamflow in the United States". In: *Hydrological sciences journal* 45.3, pp. 465–476.
- Vogel, R.M. and A. Sankarasubramanian (2005). *USGS hydro-climatic data network (HCDN): Monthly climate database*. en. Oak Ridge, Tennessee, USA. DOI: [10.3334/ORNLDaac/810](https://doi.org/10.3334/ORNLDaac/810)..
- Vogel, R.M., I. Wilson, and C. Daly (1999). "Regional regression models of annual streamflow for the United States". en. In: *Journal of Irrigation and Drainage Engineering* 125.3, pp. 148157.
- Wang, Cong, Shuai Wang, Bojie Fu, and Lu Zhang (2016). "Advances in hydrological modelling with the Budyko framework: A review". In: *Progress in Physical Geography* 40.3, pp. 409–430.
- Wang, D. and Y. Tang (2014). "A oneparameter Budyko model for water balance captures emergent behavior in Darwinian hydrologic models". en. In: *Geophysical Research Letters* 41.13, pp. 45694577.
- Wang, GQ, JY Zhang, JL Jin, YL Liu, RM He, ZX Bao, CS Liu, and Y Li (2014). "Regional calibration of a water balance model for estimating stream flow in ungauged areas of the Yellow River Basin". In: *Quaternary International* 336, pp. 65–72.
- Wang, Q.J., T.C. Pagano, S.L. Zhou, H.A.P. Hapuarachchi, L. Zhang, and D.E. Robertson (2011). "Monthly versus daily water balance models in simulating monthly runoff". en. In: *Journal of Hydrology* 404.3-4, pp. 166175.
- Xiong, Lihua and Shenglian Guo (1999). "A two-parameter monthly water balance model and its application". In: *Journal of hydrology* 216.1-2, pp. 111–123.
- Yang, D., F. Sun, Z. Liu, Z. Cong, G. Ni, and Z. Lei (2007). "Analyzing spatial and temporal variability of annual waterenergy balance in nonhumid regions of China using the Budyko hypothesis". en. In: *Water Resources Research* 43.4.
- Zhang, D., Z. Cong, G. Ni, D. Yang, and S. Hu (2015). "Effects of snow ratio on annual runoff within the Budyko framework". en. In: *Hydrology and Earth System Sciences* 19.4, pp. 19771992.

- Zhang, L., W.R. Dawes, and G.R. Walker (2001). "Response of mean annual evapotranspiration to vegetation changes at catchment scale". en. In: *Water resources research* 37.3, pp. 701708.
- Zhang, L., K. Hickel, W.R. Dawes, F.H. Chiew, A.W. Western, and P.R. Briggs (2004). "A rational function approach for estimating mean annual evapotranspiration". en. In: *Water resources research* 40.2.
- Zhang, L., N. Potter, K. Hickel, Y. Zhang, and Q. Shao (2008). "Water balance modeling over variable time scales based on the Budyko frameworkModel development and testing". en. In: *Journal of Hydrology* 360.1-4, pp. 117131.
- Zhou, G., X. Wei, X. Chen, P. Zhou, X. Liu, Y. Xiao, and Y. Su (2015). "Global pattern for the effect of climate and land cover on water yield". en. In: *Nature communications* 6.1, pp. 19.

# Chapter 4

## Quantifying the spatial coherence of deficit and excess rainfall across the continental United States<sup>1</sup>

### 4.1 Summary

Hydrometeorological extremes often occur simultaneously across a large area and cause significant economic and societal damages, and thus should be explored considering their spatiotemporal dependence. The purpose of this study, therefore, is to promote our ability to coherently understand and predict the wet/dry precipitation extremes based on their spatiotemporal covariance across the continental United States. The spatiotemporal variability of the identified joint extremes is explored and tested for its link to large-scale climate oscillations. Precipitation data from 1244 Global Historical Climatology Network (GHCN) stations, which are the stations subjected to a certain level of quality assurance, are used for generating an outlier-indicating sparse matrix based on robust principal component analysis. The sparse matrix is investigated for the spatial coherence of the joint extreme

---

<sup>1</sup>Hwang, J. and Devineni, N., 2021, Quantifying the spatial coherence of deficit and excess rainfall across the continental United States, *Geophysical Research Letters*, under review.

events for each year. Finally, the dependence between the manifestation of these outliers and El Niño Southern Oscillation, the prominent large-scale climate teleconnection is tested. This continental scale analysis of simultaneous extremes is expected to advance predictive models of hydrometeorological extremes along with providing a better understanding of the spatiotemporal coherence of extremes.

## 4.2 Introduction

Although around 25% of dams in the United States are primarily constructed for flood controls and drought preparedness (Engineers, 2021), the frequency and intensity of hydrometeorological extremes are showing upward trends in several regions of the United States (Andreadis and Lettenmaier, 2006; Dai, 2013; Kunkel et al., 2013; Armal, Devineni, and Khanbilvardi, 2018). Wright, Bosma, and Lopez-Cantu (2019) also argue thats the exceedance of hydrometeorological extremes over hydrologic design standards are becoming more frequent since 1950, particularly in the eastern half of the nation. Across the contiguous United States (CONUS), these extremes have been occurring simultaneously every year. Considering only the events that caused more than \$1 billion in damages, the United States has experienced 9.8 events of severe storms or floods and 0.8 events of droughts from 2010 to the present on average each year, and multiple counties were affected by each of these events ()�.

Figure 4.1 illustrates examples of such simultaneous extreme wet/dry conditions for four different years. Precipitation anomalies with greater magnitudes may represent simultaneous wet and dry extremes of the corresponding year. As shown in the figure, the CONUS has been under the influence of simultaneous wet/dry extremes every year, and the spatial distributions of those extremes vary

over time. In 1991, for example, the extreme wet conditions co-occurred throughout the Southeastern and Midwestern regions of CONUS, while they co-occurred in the Pacific coast, Northwestern, Midwestern, and Southeastern regions of CONUS in 1998. In these years, simultaneous extreme dry conditions occurred in Pennsylvania, northern California, and central Kansas (1991), and southern states of Texas, Louisiana, and Mississippi (1998). The spatial distributions of simultaneous wet and dry extremes were found to be different as well in 2007 and 2011. Whereas a west-central-southeast tripole-like pattern dominated 2007, a northeast-south dipole-like pattern dominated 2011. At a national scale, identifying such simultaneous extremes and modeling their manifestation, as it relates to large-scale climate teleconnection drivers, could be immensely beneficial for preparing for subsequent disasters and mitigating economic and societal damages.

The spatiotemporal variability of extremes has been actively explored across the CONUS (Bracken et al., 2015; Parker and Abatzoglou, 2016; McCabe, Wolock, and Austin, 2017; Veettil et al., 2018; McCabe and Wolock, 2021), mostly by incorporating local exceedances that are defined based on the return period thresholds for either extreme rainfall or for deficit rainfall, independently. However, this classical approach fails to account for the spatiotemporal dependence (connectedness) of hydrometeorological extremes. Spatial outliers i.e., abnormal spatial patterns of simultaneous extremes could not be captured without considering their spatiotemporal dependence. As hydrometeorological extreme events often affect large regions, their spatial outliers can have major impacts on mitigation plans and water resources management (Metin et al., 2020), especially in the United States, where significant spatial dependence of hydrometeorological extremes is observed across the territory (Brunner et al., 2020). Despite of its importance, however, there has

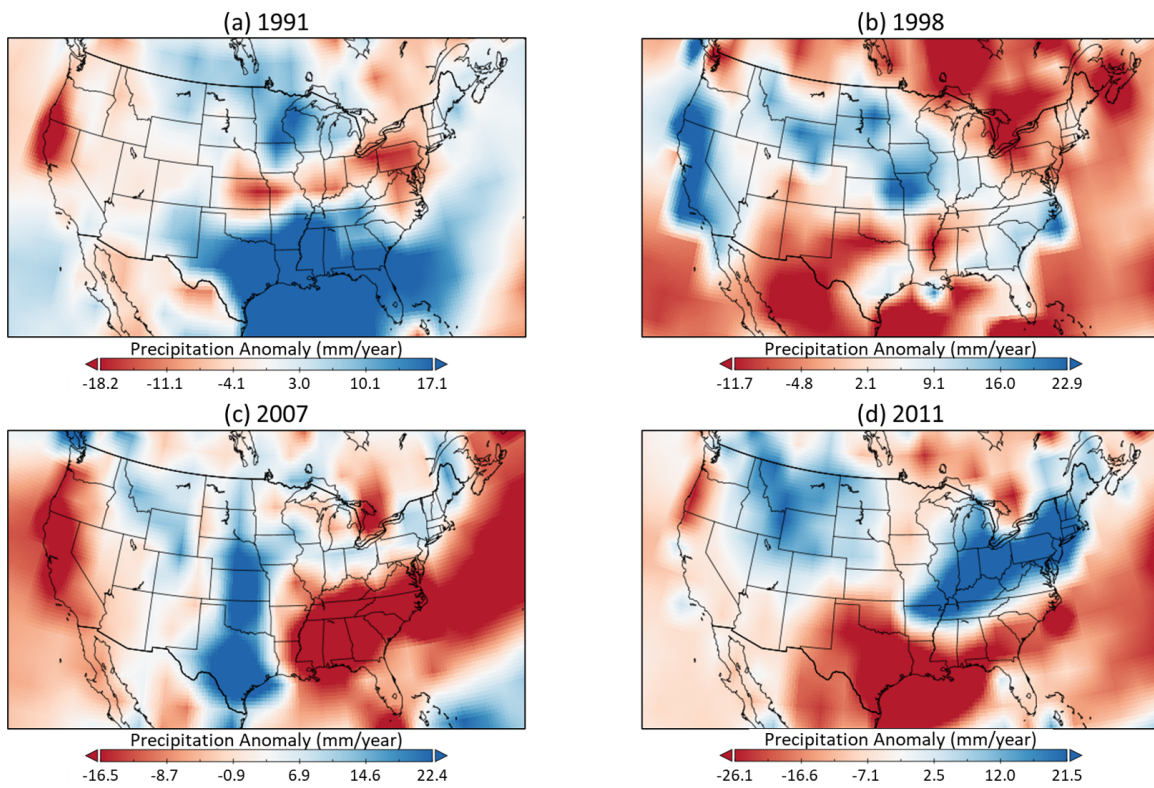


**Figure 4.1:** Annual precipitation anomalies across the CONUS for four samples years: (a) 1991, (b) 1998, (c) 2007, (d) 2011.

been little, if any, efforts on capturing wet and dry precipitation extremes considering the spatial dependence across the CONUS.

To this end, this study introduces a novel approach to explore the simultaneous precipitation extremes (both wet and dry) across the CONUS on an annual basis, considering their spatiotemporal dependence. The proposed approach involves a machine learning technique that does not rely on the classical threshold method to define extremes. The threshold method has been widely used for extreme analysis because it can be easily utilized and provide straightforward information in a form useful for decision making and interpretation. However, it often leads to significant discrepancies in analysis results depending on the selection of thresholds (Kunkel et al., 2013; Pendergrass, 2018). Our proposed approach focuses on the spatiotemporal joint variability of annual max cumulative precipitation excesses (deficits) across the CONUS and determines the spatiotemporal extremes by solving a convex program. More details of the technical approach are presented in section 4.3.

In addition to the fact that spatial dependence of simultaneous hydrometeorological extremes received little attention, its link with large-scale atmospheric teleconnections and circulations has yet been unexplored. As spatial attributes of both wet and dry precipitation extremes are often affected by large-scale climate teleconnections (Piechota and Dracup, 1996; Mo and Schemm, 2008; Archfield et al., 2016; Ward, Kummu, and Lall, 2016; Armal, Devineni, and Khanbilvardi, 2018; Najibi and Devineni, 2018), we also test if the El Niño Southern Oscillation (ENSO) has any significant association with the manifestation of simultaneous spatiotemporal extremes.

## 4.3 Materials and Methods

### 4.3.1 Precipitation Data

For this study, daily time series of precipitation observations from the Global Historical Climatology Network (GHCN) dataset (Menne et al., 2012) are employed. The GHCN dataset provides records of numerous climate variables observed from land surface stations across the globe. To ensure data quality, the following criteria were used for the review: (1) days of missing records in each year less than 20% of the year; (2) record length of daily precipitation at least 80 years; (3) data available in electronic form. As a result, 114 years (1900–2013) of GHCN daily precipitation data from 1,244 stations across the CONUS were selected to be considered for this study.

### 4.3.2 Cumulative Deficit and Excess Index

Considering the cumulative nature of meteorological droughts and excess rainfall and persistent effect of climate oscillations, we adopt and extend the concept of Cumulative Deficit Index (*CDI*) (Ravindranath et al., 2018) to represent the annual maximum wetness and dryness of precipitation. The *CDI* was originally developed to quantify the crop water stress, and thus computes the annual maximum cumulative deficit between the daily water requirement for crop growth and daily effective rainfall. For this study, the *CDI* is modified to compute the annual maximum cumulative deficit between long-term mean daily precipitation and daily precipitation as a quantification measure for the annual maximum dryness of precipitation. Extending on this algorithm, we also develop an index similar to *CDI*, which we refer to as the Cumulative Excess Index (*CEI*), to represent the annual

maximum wetness of precipitation. The *CEI* computes the annual maximum cumulative excess between long-term mean daily precipitation and daily precipitation.

For any given year  $t$  and station  $i$ , the maximum day-by-day accumulation of precipitation deficit ( $CDI_{i,t}$ ) is calculated as

$$\text{def}_{i,t,d} = \max(0, \text{def}_{i,t,d-1} + D_{i,t,d} - S_{i,t,d}), \text{ where } \text{def}_{i,t,0} = 0 \quad (4.1)$$

$$CDI_{i,t} = \max(\text{def}_{i,t,d}) \quad (4.2)$$

where  $\text{def}_{i,t,d}$  represents the accumulated daily deficit,  $D_{i,t,d}$  the long-term mean daily precipitation,  $S_{i,t,d}$  daily precipitation for station  $i$ , at day  $d$  of year  $t$ . For each year, the annual maximum dryness of precipitation is computed as the maximum value of accumulated daily deficit,  $CDI_{i,t}$ . The max function in Equation 4.1 automatically zeroes out the negative cumulative deficit values, indicating the absence of meteorological drought. The negative cumulative deficit values are accounted as excess, or  $exc_{i,t}$ :

$$exc_{i,t,d} = -\min(0, exc_{i,t,d-1} + D_{i,t,d} - S_{i,t,d}), \text{ where } exc_{i,t,0} = 0 \quad (4.3)$$

$$exc_{i,t,d} = exc_{i,t,d} + exc_{i,t,d-1}, \text{ if } \text{def}_{i,t,d} = 0 \\ OR \quad exc_{i,t,d} = 0, \text{ if } \text{def}_{i,t,d} > 0 \quad (4.4)$$

$$CEI_{i,t} = \max(exc_{i,t,d}) \quad (4.5)$$

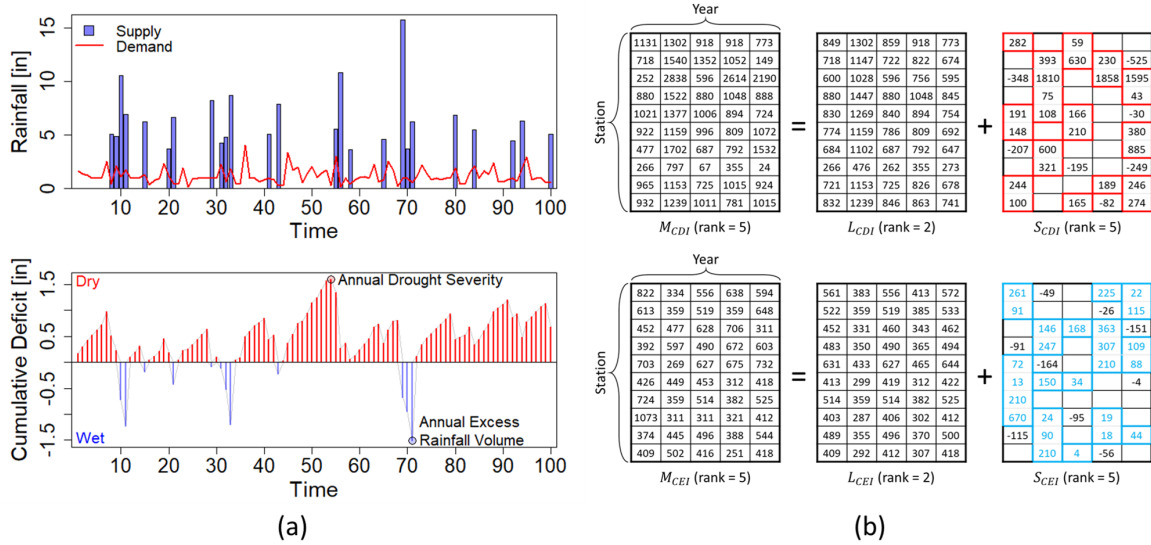


**Figure 4.2:** Diagrams of (a) how the cumulative deficit index (CDI) and cumulative excess index (CEI) are computed as rainfall distribution and long-term mean daily rainfall vary over a synthetic year and (b) how the simultaneous dry and wet extremes are defined from rPCA. In the top figure of (a), the vertical bars (supply) are the daily rainfall magnitudes, and the red line (demand) is the long-term mean daily rainfall. In the bottom figure of (a), the vertical red bars are the cumulative deficits, and the blue bars are the cumulative excesses. The top figure of (b) demonstrates the rPCA decomposition of the CDI matrix ( $M_{CDI}$ ), and the red-colored values in the sparse matrix ( $S_{CDI}$ ) are defined as the simultaneous dry extremes. The bottom figure of (b) shows the decomposition of the CEI matrix ( $M_{CEI}$ ), and the blue-colored values in the sparse matrix ( $S_{CEI}$ ) are defined as the simultaneous wet extremes.

where  $exc_{i,t,d}$  refers to the daily excess of precipitation. The variable  $exc_{i,t,d}$  in Equation 4.4 accumulates the daily excess  $exc_{i,t,d}$  over time, but only for the days where excess occurs, i.e., when  $def_{i,t,d}$  is zero. The maximum value of accumulated daily excess, or  $CEI_{i,t}$ , is considered to represent the annual maximum wetness of precipitation. Figure 4.2a illustrates how CDI and CEI are determined based on the accumulative precipitation deficit and excess. The CDI and CEI are computed for all the stations each year, and thus we eventually obtain two 1244-by-114 CDI and CEI matrices.

### 4.3.3 Robust Principal Component Analysis (rPCA)

After obtaining the *CDI* and *CEI* matrices, each matrix is examined with the robust Principal Component Analysis (rPCA), which was originally developed for the purpose of recovering the principal components of a partially corrupted data matrix (Candès et al., 2011). The rPCA procedure decomposes the input matrix ( $M$ ) into a low-rank matrix ( $L$ ) and sparse matrix ( $S$ ) by solving a convenient convex program called Principal Component Pursuit (PCP):

$$\text{minimize } \|L\|_* + \lambda \|S\|_1 \quad (4.6)$$

$$\text{subject to } L + S = M \quad (4.7)$$

where  $\|L\|_*$  denotes the nuclear norm of the  $L$  (i.e., the sum of singular values of  $L$ ),  $\|S\|_1$  the 1-norm of  $S$  (i.e., the sum of the absolute values of the entries), and  $\lambda$  is the tuning parameter that depends on the dimension size of  $M$ . In our case,  $M$  is the *CDI* (or *CEI*) matrix, and its column and row represent the time and spatial domain, respectively. The low-rank matrix  $L$  consists of *CDI* (or *CEI*) values with its spatiotemporal outliers replaced with estimations from PCP. Since the low-rank matrix  $L$  can be well explained with its principal components, here, we describe it as the spatiotemporal variability of the *expected CDI* (or *CEI*).

Meanwhile, the sparse matrix  $S$  contains the joint anomalies of the given matrix  $M$ . In our case, the sparse matrix  $S$  is composed of outliers that are far off from the spatiotemporal joint distribution of the *CDI* (or *CEI*). The entries of the sparse matrix indicate the partial amount of *CDI* (or *CEI*) that could not be explained by the principal components of low-rank matrix  $L$ , and thus we describe the sparse

matrix  $S$  as the spatiotemporal variability of the *unexpected amount* of CDI (or CEI).

Figure 4.2b demonstrates a procedure of capturing the annual spatiotemporal extremes using rPCA. The sparse matrix can have positive, negative, and non-value entries, as shown in the figure. A negative entry value of a sparse matrix indicates that the corresponding event is extraordinarily weak based on the spatiotemporal joint covariance of the total events. Since this study intends to focus on extremes that might have significant impact, therefore, we define only the events where the entry value of their sparse matrix is positive as spatiotemporal extremes, as shown in Figure 4.2b. This selection allows us to focus on spatiotemporal extremes that have greater intensities. It should be noted that events with extremely strong intensity may not always be identified as spatiotemporal extremes when using rPCA. For example,  $M_{CDI}(1, 2)$  from Figure 4.2b shows the highest CDI value for that station but is not classified as a spatiotemporal extreme event. This is because such intensive events could comply with the spatiotemporal joint covariance of the total. Those events can be still identified in the low-rank matrix. In addition, the spatiotemporal extremes may contain events that would not be classified as extremes from the local return period threshold classification. For example,  $M_{CDI}(1, 3)$  from Figure 4.2b shows a relatively low CDI value for that station but is still classified as an extreme event. In this case, such low CDI value might be outlying from the spatiotemporal joint covariance of the total.

#### 4.3.4 Climate modeling with ENSO

Large-scale periodic fluctuation in sea surface temperature and air pressure, such as ENSO, affects the variability of the global atmospheric circulation and local climate anomalies across the United States (Gershunov and Barnett, 1998;

Rajagopalan et al., 2000; Mo and Schemm, 2008; Najibi, Deveneni, and Lu, 2017; Armal, Deveneni, and Khanbilvardi, 2018), and force simultaneous influences on the manifestation of spatiotemporal extremes. In this section, therefore, we tested the large-scale climate impact on the simultaneous manifestation of spatiotemporal extremes by running a logistic regression on ENSO3.4 index. First, we create a binary matrix that indicates the occurrence of spatiotemporal extremes based on the sparse matrix. The binary matrix denotes 1 for the events with positive sparse entry and 0 for non-positive sparse entries. Then the logistic model for station  $i$  at year  $t$  is developed as:

$$Y_{i,t} \sim \text{Binomial}(P_{i,t}) \quad (4.8)$$

$$\text{logit}(P_{i,t}) = \alpha_i + \beta_i \cdot \text{ENSO}_t \quad (4.9)$$

where  $Y_{i,t}$  refers to the binomial matrix representing the simultaneous manifestation of spatiotemporal extremes,  $P_{i,t}$  to the probability of occurrence, and  $\text{ENSO}_t$  to the annual mean ENSO.  $\alpha_i$  and  $\beta_i$  are the station-wise coefficients for the regression model. This process is carried out for both *CDI* and *CEI*.

## 4.4 Results

Here, we present the maps of spatiotemporal extremes for the four example years (1991, 1998, 2007, and 2011) of which the annual precipitation anomalies were displayed in Figure 4.1. Then a qualitative analysis is conducted on the results by focusing on the clusters of extremes with relatively greater measures.

#### 4.4.1 Simultaneous Dry Extremes

Based on the  $CDI$  sparse matrix obtained from rPCA, we identify the spatiotemporal dry extremes for each year from 1900 to 2013. The left column of Figure 4.3a exhibits the spatial variability of the dry extremes across the CONUS for the four example years. The spatial variability of the dry extremes shows a strong agreement to the annual precipitation anomalies each year, except for 1998 spatiotemporal dry extremes occurred throughout the South and Southeast regions, but dry annual precipitation anomalies were not significant in those areas. This implies that the amount of rainfall the South and Southeast regions received in 1998 is close to the average of the local historical records, while the  $CDI$  in those areas significantly deviates from the spatiotemporal joint covariance.

The right column of Figure 4.3a displays the *unexpected amount* of the spatiotemporal dry extremes in a fractional form by computing the ratio of the sparse element to extreme  $CDI$ . In 1991, clusters of spatiotemporal dry extremes are found in the Pacific coast, Midwest, and Northeast regions, and a large proportion of their measures are shown to be *unexpected*. In 1998, spatiotemporal dry extremes occur across the eastern half of the nation, and they show especially stronger intensity in the South and Southeast regions. However, they are mostly *expected*, except for some areas in the Northeast and Midwest regions. In 2007, spatiotemporal dry extremes are observed in the Pacific coast, Ohio Valley (Central), Southeast, Upper Midwest regions. In particular, the Southeast region experiences spatiotemporal dry extremes with large magnitudes. The spatiotemporal dry extremes at the Pacific coast, Upper Midwest region, and the northbound of the Southeast region are mostly *unexpected* events. Lastly in 2011, clusters of intensive spatiotemporal dry extremes are found in the Pacific coast and South regions, and a large portion of

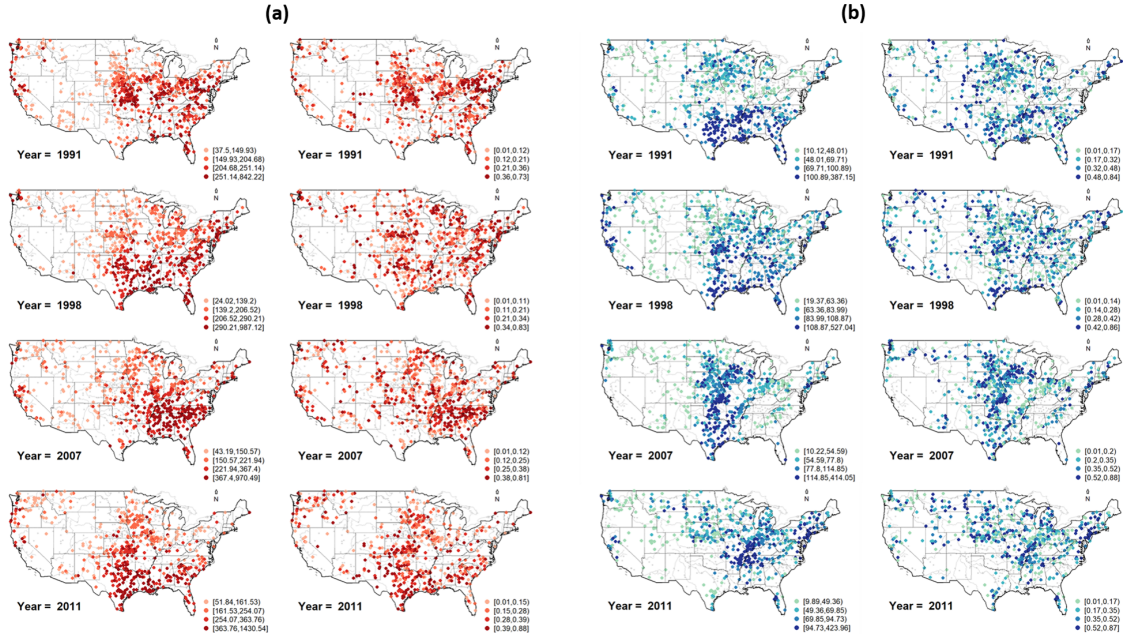


**Figure 4.3:** Spatial variability of (a) spatial distributions of spatiotemporal dry extremes (left) and proportion of CDI that is unexpected (right) and (b) of spatial distributions of spatiotemporal wet extremes (left) and proportion of CEI that is unexpected (right) for four sample years 1991, 1998, 2007, 2011.

those extremes are *unexpected*.

#### 4.4.2 Simultaneous Wet Extremes

The simultaneous manifestation of spatiotemporal wet extremes is annually identified based on the *CEI* sparse matrix from 1900 to 2013. The left column of Figure 4.3b exhibits the spatial variability of the spatiotemporal wet extremes across the CONUS for the four sample years (1991, 1998, 2007, and 2011). The spatial variability of the wet extremes shows reasonable conformity to the annual precipitation anomalies for each year.

The right column of Figure 4.3b displays the proportion of *unexpected* spatiotemporal wet extremes by computing the ratio of the sparse element to extreme *CEI*. In 1991, the spatiotemporal wet extremes occur in the South, Southeast, and Upper

Midwest regions, and significant portion of these events are *unexpected* in those areas. In 1998, Pacific coast, westbound of Ohio Valley region, and southbound of the Southern region experience spatiotemporal wet extremes. Such spatiotemporal wet extremes are mostly *unexpected* to these locations. In 2007, the spatiotemporal wet extremes manifest across the South and Upper Midwest regions. These events are more *expected* in the South region than in the Midwest region. Finally in 2011, the spatiotemporal wet extremes occur across Ohio Valley region, but a large portion of the events are *expected*.

#### 4.4.3 Association of Spatiotemporal Extremes with El Niño Southern Oscillation

Figure 4.4 shows where the annual ENSO has a statistically significant ( $p - value < 0.05$ ) association with the manifestation of spatiotemporal extremes across the CONUS. In the figure, the CONUS is divided into 18 Hydrologic Unit Code (HUC02) basins to represent the hydrometeorological impact of the ENSO-significant locations. As shown in the figure, the majority of the stations where the spatiotemporal dry extremes show a negative association with ENSO are located vertically across the middle of the CONUS (HUC02 regions 7, 10, 11, and 12). On the other hand, stations where the spatiotemporal dry extremes show positive association with ENSO are located in the Northwest, Ohio Valley, Southeast, and Northeast regions (HUC02 regions 2, 3, 5, 7, and 17).

As shown in Figure 4.4b, the ENSO-significant stations for spatiotemporal wet extremes show a spatial distribution similar to Figure 4.4a but with the directions reversed. The stations where the spatiotemporal wet extremes show a negative association with ENSO are mostly located in the Ohio Valley, Southeast, and Northeast regions (HUC02 regions 2, 3, 5, and 7). Clusters of stations show a positive

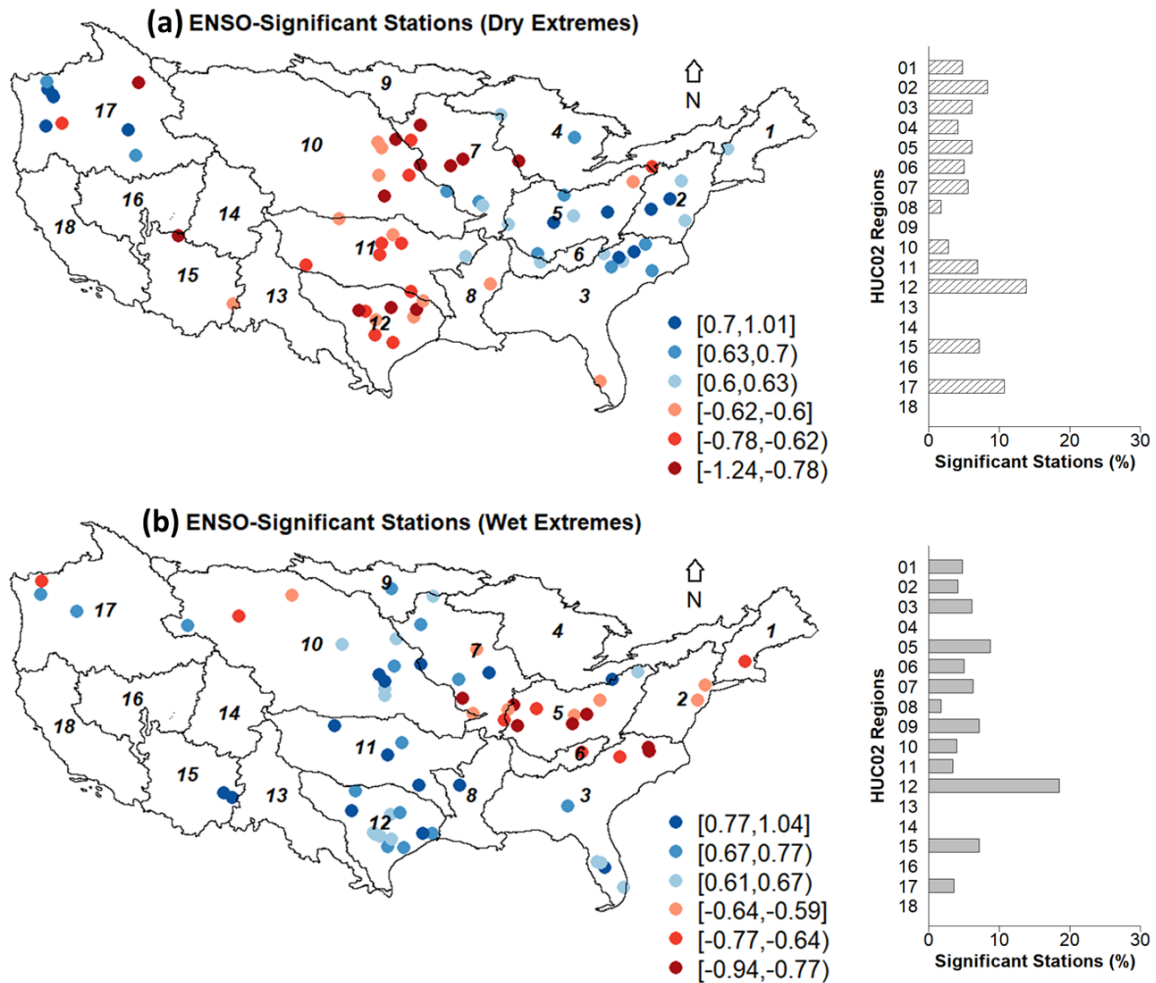


**Figure 4.4:** (a) Spatial distribution of stations where the simultaneous manifestation of spatiotemporal dry extremes has statistically significant association with ENSO and (b) stations where the simultaneous manifestation of spatiotemporal wet extremes has statistically significant association with ENSO. The color of the dots indicates the  $\beta$  coefficient for ENSO. The CONUS is divided into HUC02 basins and the percentage of ENSO-significant stations in each basin is presented alongside both maps.

association between the spatiotemporal wet extremes with ENSO in the South, Northern Rockies and Plains, Upper Midwest, and Southeast regions (HUC02 regions 3, 7, 10, 11, and 12).

## 4.5 Summary

Many classification methods of hydrometeorological extremes only consider the at-site frequency distribution and their return levels, and do not consider the spatial dependence of the extremes. Here, we introduce a novel framework that systematically identifies simultaneous hydrometeorological extremes considering their spatiotemporal joint variability. The proposed framework adopts the concept of *CDI* to reflect the cumulative nature of hydrometeorological extremes and develops two matrices that represent the spatiotemporal variability of the annual maximum dryness and wetness, respectively. Then rPCA is applied to each annual-max matrix to identify its spatiotemporal joint outliers, which we define as the spatiotemporal dry extremes and spatiotemporal wet extremes, respectively. We also demonstrate how the outlying magnitude of spatiotemporal extremes can be quantified from their sparse matrix. As part of the study, the manifestation of spatiotemporal extremes is modeled with ENSO to explore their association across the CONUS.

As Stephenson, Diaz, and Murnane (2008) notes, extreme events are generally easy to recognize but difficult to define. Abundant studies of extremes have been focusing on very rare or intensive extreme events, but the surprising events that drive significant changes in the national policies are argued to be both unexpectedly large and occurring simultaneously in multiple locations (Kjeldsen and Prodocimi, 2018). Correspondingly, this study has the potential to provide invaluable

source of information for decision-makers and policy initiatives regarding future flood and drought preparedness plans at a national-scale.

# References

- Andreadis, K.M. and D.P. Lettenmaier (2006). "Trends in 20th century drought over the continental United States". en. In: *Geophysical Research Letters* 33.10.
- Archfield, S.A., R.M. Hirsch, A. Viglione, and G. Blöschl (2016). "Fragmented patterns of flood change across the United States". en. In: *Geophysical research letters* 43.19, pp. 10232.
- Armal, S., N. Devineni, and R. Khanbilvardi (2018). "Trends in extreme rainfall frequency in the contiguous United States: Attribution to climate change and climate variability modes". en. In: *Journal of Climate* 31.1, pp. 369385.
- Bracken, C., B. Rajagopalan, M. Alexander, and S. Gangopadhyay (2015). "Spatial variability of seasonal extreme precipitation in the western United States". en. In: *Journal of Geophysical Research: Atmospheres* 120.10, pp. 45224533.
- Brunner, M.I., E. Gilleland, A. Wood, D.L. Swain, and M. Clark (2020). "Spatial dependence of floods shaped by spatiotemporal variations in meteorological and landsurface processes". en. In: *Geophysical Research Letters* 47.13, p. 2020 088000.
- Candès, E.J., X. Li, Y. Ma, and J. Wright (2011). "Robust principal component analysis?" es. In: *Journal of the ACM (JACM)* 58.3, pp. 137.
- Dai, A. (2013). "Increasing drought under global warming in observations and models". en. In: *Nature climate change* 3.1, pp. 5258.
- Engineers, U.S. Army Corps (2021). *National Inventory of Dams*. it. Washington D. C. URL: <https://nid.sec.usace.army.mil/ords/f?p=105:19:12463373659661::NO:::>
- Environmental Information, NOAA National Centers for.
- Gershunov, A. and T.P. Barnett (1998). "ENSO influence on intraseasonal extreme rainfall and temperature frequencies in the contiguous United States: Observations and model results". en. In: *Journal of Climate* 11.7, pp. 15751586.
- Kjeldsen, T.R. and I. Prosdocimi (2018). "Assessing the element of surprise of record-breaking flood events". fr. In: *Journal of Flood Risk Management* 11, pp. 541 553.
- Kunkel, K.E., T.R. Karl, H. Brooks, J. Kossin, J.H. Lawrimore, D. Arndt, and K. Emanuel (2013). "Monitoring and understanding trends in extreme storms: State of knowledge". en. In: *Bulletin of the American Meteorological Society* 94.4, pp. 499514.

- McCabe, G.J. and D.M. Wolock (2021). "Multiyear hydroclimatic droughts and pluvials across the conterminous United States". en. In: *International Journal of Climatology* 41.3, pp. 17311746.
- McCabe, G.J., D.M. Wolock, and S.H. Austin (2017). "Variability of runoffbased drought conditions in the conterminous United States". en. In: *International Journal of Climatology* 37.2, pp. 10141021.
- Menne, M.J., I. Durre, R.S. Vose, B.E. Gleason, and T.G. Houston (2012). "An overview of the global historical climatology network-daily database". en. In: *Journal of atmospheric and oceanic technology* 29.7, pp. 897910.
- Metin, A.D., N.V. Dung, K. Schröter, S. Vorogushyn, B. Guse, H. Kreibich, and B. Merz (2020). "The role of spatial dependence for large-scale flood risk estimation". en. In: *Natural Hazards and Earth System Sciences* 20.4, pp. 967979.
- Mo, K.C. and J.E. Schemm (2008). "Relationships between ENSO and drought over the southeastern United States". en. In: *Geophysical Research Letters* 35.15.
- Najibi, N. and N. Devineni (2018). "Recent trends in the frequency and duration of global floods". en. In: *Earth System Dynamics* 9.2, pp. 757783.
- Najibi, N., N. Devineni, and M. Lu (2017). "Hydroclimate drivers and atmospheric teleconnections of long duration floods: An application to large reservoirs in the Missouri River Basin". en. In: *Advances in water resources* 100, pp. 153167.
- Parker, L.E. and J.T. Abatzoglou (2016). "Spatial coherence of extreme precipitation events in the northwestern United States". en. In: *International Journal of Climatology* 36.6, pp. 24512460.
- Pendergrass, A.G. (2018). "What precipitation is extreme?" fr. In: *Science* 360.6393, pp. 10721073.
- Piechota, T.C. and J.A. Dracup (1996). "Drought and regional hydrologic variation in the United States: Associations with the El NiñoSouthern Oscillation". en. In: *Water Resources Research* 32.5, pp. 13591373.
- Rajagopalan, B., E. Cook, U. Lall, and B.K. Ray (2000). "Spatiotemporal variability of ENSO and SST teleconnections to summer drought over the United States during the twentieth century". en. In: *Journal of Climate* 13.24, pp. 42444255.
- Ravindranath, A., N. Devineni, U. Lall, and P. Concha Larrauri (2018). "Season-ahead forecasting of water storage and irrigation requirementsan application to the southwest monsoon in India". en. In: *Hydrology and Earth System Sciences* 22.10, pp. 51255141.
- Stephenson, D.B., H.F. Diaz, and R.J. Murnane (2008). "Definition, diagnosis, and origin of extreme weather and climate events". en. In: *Climate Extremes and Society* 340, pp. 1123.
- Veettil, A.V., G. Konapala, A.K. Mishra, and H.Y. Li (2018). "Sensitivity of drought resilience-vulnerability-exposure to hydrologic ratios in contiguous United States". en. In: *Journal of hydrology* 564, pp. 294306.

- Ward, P.J., M. Kummu, and U. Lall (2016). "Flood frequencies and durations and their response to El Niño Southern Oscillation: Global analysis". en. In: *Journal of Hydrology* 539, pp. 358378.
- Wright, Daniel B, Christopher D Bosma, and Tania Lopez-Cantu (2019). "US hydrologic design standards insufficient due to large increases in frequency of rainfall extremes". In: *Geophysical Research Letters* 46.14, pp. 8144–8153.

# **Chapter 5**

## **Conclusion and Forward**

### **5.1 Concluding Remarks**

This dissertation presented a comprehensive study on the hydrosystems of the United States through multifaceted analysis of its modified and unmodified basins. This was followed by understanding the complex mechanism of the spatiotemporal variability of streamflow and the manifestation of hydrometeorological extremes. The Colorado River Basin was selected as the testbed to understand the spatiotemporal variability of the streamflow and its frequency in modified basins. To understand the spatiotemporal variability of the streamflow in natural basins, basins that are minimally affected by human influences were tested throughout the contiguous United States. To understand the manifestation of simultaneous hydrometeorological extremes, investigations were conducted for the contiguous United States. Important remarks that were established throughout the above chapters are recited below.

1. In Chapter 2, the scale-averaged wavelet coherence between monthly observed and natural flows was explored across the highly regulated Colorado

River Basin to capture and understand the spatiotemporal changes in the annual (10 to 14 months) and multi-annual (24 to 60 months) frequencies over the river network. The study found clear alterations in annual and multi-annual frequencies, which varied spatially across the basin. As part of the study, the local alterations in the streamflow frequency due to dam operations were separated with an intent to distinguish the main sources of the cumulative alterations.

It was revealed that, 1) the alteration in the frequency signal of the San Juan River is dominantly derived by the Navajo Dam; 2) the wavelet coherence loss of the streamflow between the Hoover Dam and Glen Canyon Dam shows a homogeneous fluctuation across the segment, and the majority of this pattern is presumed to be caused by the local impact from Glen Canyon Dam; 3) the pattern of wavelet coherence loss in the rest of the Colorado River after the Hoover Dam shows a uniform pattern across the segment, and we conclude that this is inherited from the management of the Glen Canyon Dam operation; 4) Overall, the annual frequency in the streamflow recovers as it passes the Hoover Dam, and alteration of the multi-annual frequency intensifies as the flow proceeds downstream.

The approach using the coherence loss between the natural flow and altered flow is novel in the estimation of river alterations. The proposed approach is transferable to other highly regulated basins, and thus can significantly contribute to the field of sustainable water management. The proposed approach could be also utilized when allocating new dams or re-operating existing dams. This study also emphasized the significance of reconstructing the naturalized flow for a long period over large regions.

2. In Chapter 3, the complex hydrological process was unfolded using Zhang's Dynamic Water Balance Model (ZDWBM) for the natural basins across the contiguous United States. To handle the effect of snowmelt water, the study proposed a Budyko-type snow module based on surface energy balance, preserving the spirit of Budyko-basis and parameter parsimony that is achieved from ZDWBM, and it was introduced into ZDWBM. In addition, the study applied monthly parameterization to the model to capture the time-variant catchment properties while minimizing the increase in model complexity. The proposed model showed significant improvement predicting the water balance for natural basins, including those in regions where snowmelt water plays significant role.

It was shown in the study that, 1) the snow melting process can be represented by extending the supply-demand concept of Budyko's framework; 2) time-invariant model parameters could produce seasonal bias, and monthly parameterization can reduce such bias without causing overfitting to the model.

Overall, the proposed model has the potential to be used for analyzing and predicting the streamflow responses to changes in regional climate and land-use/land-cover for natural catchments, including snow-affected and ungauged basins. This could be a significant aspect since predicting water availability for ungauged basins has been one of the prolonged interest in the field of water resources and hydrology.

3. In Chapter 4, a novel threshold-free machine-learning-based approach for identification of spatiotemporal wet and dry extremes was presented. The proposed approach adopt and extended the concept of CDI to quantify the

annual maximum cumulative precipitation deficit and excess across the contiguous United States. A robust principal component analysis was applied to each set of those annual quantities to identify their spatiotemporal joint outliers. The identified spatiotemporal joint outliers were defined as the spatiotemporal dry extremes and spatiotemporal wet extremes. Based on the sparse matrix from rPCA, it was able to quantify the amount of outlying magnitude of the spatiotemporal precipitation extremes. As part of the study, the manifestation of spatiotemporal precipitation extremes were modeled with the El Niño Southern Oscillation to explore their association across the contiguous United States.

The study showed 1) a novel approach for capturing the simultaneous spatiotemporal precipitation extremes at the national scale; 2) the manifestation of spatiotemporal precipitation extremes have significant association with the El Niño Southern Oscillation in some areas in the Northeast, Ohio Valley, Southeast, Northeast, South, Upper Midwest, Northern Rockies and Plains, and Upper Midwest regions.

The approach using robust principal component analysis is novel in extremes identification. It identifies spatiotemporal extremes accounting for the spatial dependence of simultaneous extremes without relying on artificial thresholds. By providing enhanced understanding of the spatial dimension of simultaneous extremes, this study can contribute to the national flood and drought preparedness.

## 5.2 Future Works

The present dissertation largely divided the hydrosystems of the United States into three parts and explored them independently. As hydrosystems are becoming more complex under the changing climate and human influences, however, an integrated understanding of the hydroclimatology is required. Future works, therefore, may focus on expanding the concepts and findings of the present dissertation. The novel approaches that were developed during the present dissertation may serve as useful tools for complementing our current knowledge and even exploring the unknown hydrological domain in the future. Each chapter of the current dissertation presents its own direction for further studies, and future works of this dissertation will focus on following and integrating the suggested directions. A summary of the future works is outlined below:

1. Based on the findings from the investigation of dam-induced streamflow alterations, future works may include developing the time series of streamflow alterations at finer frequency scales. Once the time series is obtained, the efficiency of dam operations could be tested against local climate variability and water demand. Such examination could be used to develop a systematic approach for basin-wide optimal rule curves for each reservoir, leveraging the regional factors and the organic structure of the dendritic river network. As the impacts of dam operations are shown to propagate throughout the riverine system, these basin-wide optimal rule curves will contribute relaxing the cumulative water stress induced by upstream dam operations and reconciling the divergent needs of water.
2. The Budyko-based dynamic water balance model that was developed in this

dissertation shows a significant improvement in accuracy and applicability compared to the original model. One of the limitations of the developed model is that it does not provide the uncertainty levels of the parameters. One may consider redesigning the proposed model in a Bayesian hierarchical structure to quantify the uncertainties. The Bayesian structure will also improve the calibration process by pooling the geospatial information across the sites. The multilevel structure, then, can be used as for predictions in ungauged basins. Based on the proposed model, further investigation on the model parameters could be conducted to explore streamflow sensitivity to changes in local climate and land-use/land-cover.

3. As this dissertation demonstrated an approach for identifying simultaneous spatiotemporal precipitation extremes using rPCA, one would be interested in applying rPCA to the streamflow data as well. Then the spatial dependence between the detected simultaneous hydrological extremes and simultaneous precipitation extremes can be directly measured. As the antecedence conditions of the basin is known to be one of the important factors that determines the transition level of precipitation extreme to hydrological extreme, it would be also meaningful to explore the autocorrelation between the simultaneous hydrological and climate conditions.
4. One possible integrative future work could be exploring the spatiotemporal variability in land-surface water fluxes for human-altered watersheds by extending Budyko's framework. The quantification of hydrological impacts of regional climate forcings, catchment characteristics, and anthropogenic factors will allow us to explore the vulnerability of modified basins to simultaneous extremes.

This dissertation emphasizes the importance of understanding the hydrology at both modified and natural basins and their possible extreme events as a whole to properly control and assess the current and future hydrosystem. For example, naturalized flow series could be reconstructed for basins across the United States by modeling the parameters of ZDWBM-msnow based on observable attributes of the basin – *e.g.*, aridity index, vegetation coverage, curve number, elevation, etc. – and running the ZDWBM-msnow. The level of alteration in streamflow can be assessed across the United States by comparing the reconstructed naturalized flow and controlled flow. Based on such comparison, moreover, the capability of current hydrological infrastructures in mitigating hydrometeorological disasters can also be evaluated, and this evaluation can provide information on how vulnerable the basin is to meteorological extremes of which would likely occur. Thus all the chapters of this dissertation are inherently connected by this motivation to improve the management of hydrosystems.

The potential future works of the present dissertation include but are not limited to the outlined ideas above. The overall objective of future works of this dissertation is to contribute to the reliability of contemporary and future water resources management by comprehensively understanding the complex interactions between hydroclimate drivers and catchment water balance.

ProQuest Number: 28543140

INFORMATION TO ALL USERS

The quality and completeness of this reproduction is dependent on the quality  
and completeness of the copy made available to ProQuest.



Distributed by ProQuest LLC (2021).

Copyright of the Dissertation is held by the Author unless otherwise noted.

This work may be used in accordance with the terms of the Creative Commons license  
or other rights statement, as indicated in the copyright statement or in the metadata  
associated with this work. Unless otherwise specified in the copyright statement  
or the metadata, all rights are reserved by the copyright holder.

This work is protected against unauthorized copying under Title 17,  
United States Code and other applicable copyright laws.

Microform Edition where available © ProQuest LLC. No reproduction or digitization  
of the Microform Edition is authorized without permission of ProQuest LLC.

ProQuest LLC  
789 East Eisenhower Parkway  
P.O. Box 1346  
Ann Arbor, MI 48106 - 1346 USA